

Electronic Theses and Dissertations, 2004-2019

2013

Analytical And Experimental Study Of Monitoring For Chain-like Nonlinear Dynamic Systems

Bryan Paul
University of Central Florida

 Part of the [Civil Engineering Commons](#), and the [Structural Engineering Commons](#)
Find similar works at: <https://stars.library.ucf.edu/etd>
University of Central Florida Libraries <http://library.ucf.edu>

This Masters Thesis (Open Access) is brought to you for free and open access by STARS. It has been accepted for inclusion in Electronic Theses and Dissertations, 2004-2019 by an authorized administrator of STARS. For more information, please contact STARS@ucf.edu.

STARS Citation

Paul, Bryan, "Analytical And Experimental Study Of Monitoring For Chain-like Nonlinear Dynamic Systems" (2013). *Electronic Theses and Dissertations, 2004-2019*. 2908.
<https://stars.library.ucf.edu/etd/2908>

ANALYTICAL AND EXPERIMENTAL STUDY OF MONITORING FOR CHAIN-LIKE
NONLINEAR DYNAMIC SYSTEMS

by

BRYAN PAUL

B.S.C.E University Of Central Florida, 2010

B.S.Env.E University Of Central Florida, 2010

A thesis submitted in partial fulfillment of the requirements
for the degree of Master of Science
in the Department of Civil, Environmental, and Construction Engineering
in the College of Engineering and Computer Science
at the University of Central Florida
Orlando, Florida

Spring Term
2013

Major Professor: Hae-Bum Yun

© 2013 BRYAN PAUL

ABSTRACT

Inverse analysis of nonlinear dynamic systems is an important area of research in the field of structural health monitoring for civil engineering structures. Structural damage usually involves localized nonlinear behaviors of dynamic systems that evolve into different classes of nonlinearity as well as change system parameter values. Numerous parametric modal analysis techniques (e.g., eigensystem realization algorithm and subspace identification method) have been developed for system identification of multi-degree-of-freedom dynamic systems. However, those methods are usually limited to linear systems and known for poor sensitivity to localized damage. On the other hand, non-parametric identification methods (e.g., artificial neural networks) are advantageous to identify time-varying nonlinear systems due to unpredictable damage. However, physical interpretation of non-parametric identification results is not as straightforward as those of the parametric methods. In this study, the Multidegree-of-Freedom Restoring Force Method (MRFM) is employed as a semi-parametric nonlinear identification method to take the advantages of both the parametric and non-parametric identification methods.

The MRFM is validated using two realistic experimental nonlinear dynamic tests: (i) large-scale shake table tests using building models with different foundation types, and (ii) impact test using wind blades. The large-scale shake table test was conducted at Tongji University using 1:10 scale 12-story reinforced concrete building models tested on three different foundations, including pile, box and fixed foundation. The nonlinear dynamic signatures of the building models collected from the shake table tests were processed using MRFM (i) to investigate the effects of foundation types on nonlinear behavior of the superstructure and (ii) to detect localized damage during the shake table tests. Secondly, the MRFM was applied to investigate the applicability of this method to wind turbine blades. Results are promising, showing a high level of nonlinearity of the system and how the MRFM can be applied to wind-turbine blades. Fu-

ture studies were planned for the comparison of physical characteristic of this blade with blades created made of other material.

This work is dedicated to those who have left a positive impact on my life and made me a better person.

ACKNOWLEDGMENTS

I would like to thank the following people. My advisor and committee chair Dr. Yun. My committee members Dr. Catbas and Dr. Chopra. All of the people who have contributed to my education from my elementary school teachers to my professors at UCF. The people at Omega Engineering who were always helpful answering my questions. The wonderful staff in the UCF CECE department Juan Cruz, Margarida Trim, Pauline Strauss and Carol Ann Pohl. The wonderful UCF CECS staff Pedro Cordero, Donald Scrip and Peter Alfieris. All of the other UCF staff that has helped me. My friends: Aaron Rank, Yoonhwak “Danny” Kim, Toni-Gaye McCulloch, Ayad “Bubba” Ali, Ganesh Sundaresan, Mohamed Rowimi, Nader Mehdawi, Ahmad Naili and Liuliu Wu. My brothers and parents: Spencer, Nik, Mike and Donna. My fiancée Kristen Ridenhour. Celine Kavalec-Miller who did her best to make me a better writer.

TABLE OF CONTENTS

LIST OF FIGURES	ix
LIST OF TABLES	xii
1 INTRODUCTION	1
1.1 Problem Statement	1
1.2 Motivation	1
1.3 Objectives	2
1.4 Scope And Approach	2
2 RESTORING FORCE METHOD	4
2.1 Single Degree Of Freedom Restoring Force Method	5
2.2 Multi-Degree-Of-Freedom Restoring Force Method	9
2.3 Previous Studies Using RFM And MRFM	15
3 ANALYTICAL STUDY: SYSTEM IDENTIFICATION FOR MULTI-DEGREE-OF-FREEDOM OSCILLATORS	18
3.1 Examples Of Oscillators	18
3.2 Analytical Simulation	21
3.3 System Identification	24
3.3.1 Linear System	24
3.3.2 Duffing System	27
3.3.3 Dead-Space Nonlinear System	30
3.4 Conclusions From The Analytical Study	34
4 EXPERIMENTAL NONLINEAR IDENTIFICATION FOR BUILDING STRUCTURES WITH DIFFERENT FOUNDATION TYPES	35
4.1 Experimental Setup	35
4.1.1 Background	35
4.1.2 Equipment	35
4.1.3 Sample Preparation	39
4.1.4 Instrumentation	40
4.1.5 Excitation	41
4.1.6 Experimental Protocol	43
4.1.7 Damage Observation After Shake Table Tests	44
4.2 Preprocessing Of Sensor Measurements	47
4.2.1 Restoring Force Estimation	50
4.3 Multidegree Of Freedom Restoring Force Method Results	54

4.3.1	Error In Estimation	55
4.3.2	MRFM For Fixed Foundation	63
4.3.3	Term Wise Identification	69
4.3.4	Effects Of Foundation	80
4.3.5	Effects Of Damage	83
5	EXPERIMENTAL NONLINEAR IDENTIFICATION FOR SMALL SCALE WIND	
	TURBINE BLADE	88
5.1	Background	88
5.2	Literature Review: Wind Turbines	89
5.2.1	Introduction	89
5.2.2	Floating Wind Turbine Structural Design	90
5.2.3	Floating Wind Turbine Subtypes	90
5.2.4	Wind Potential	92
5.2.5	Hywind	93
5.3	Experimental Study	94
5.3.1	Sample Preparation	94
5.3.2	Instrumentation	95
5.3.3	Test Protocol	97
5.4	Preprocessing	97
5.4.1	Restoring Force Estimation	99
5.5	Multidegree Of Freedom Restoring Force Method Results	102
5.5.1	Error In Estimation	103
5.6	MRFM For Wind Turbine Blade	106
5.7	Discussion	108
6	SUMMARY AND CONCLUSIONS	109
6.1	Summary And Conclusions	109
6.2	Challenges Presented In The Application Of The Restoring Force	109
6.3	Suggestions For Future Studies	110
	LIST OF REFERENCES	112

LIST OF FIGURES

2.1	A nonlinear, single-degree-of-freedom system.	6
2.2	A nonlinear, multidegree of freedom system, with unknown restoring forces. .	10
3.1	Seven-degree-of-freedom system	19
3.2	Linear phase diagrams of the restoring force vs displacement with reconstructed restoring force	25
3.3	Duffing phase diagrams of the restoring force vs displacement with reconstructed restoring force	29
3.4	Phase diagrams of the restoring force vs displacement with reconstructed restoring force using up to the 4th order Chebyshev coefficients	31
3.5	Phase diagrams of the restoring force vs displacement with reconstructed restoring force using up to the 8th order Chebyshev coefficients	32
3.6	Phase diagrams of the restoring force vs displacement with reconstructed restoring force using up to the 12th order Chebyshev coefficients	32
4.1	Pictures of the container fully assembled (Chen, 2001).	37
4.2	Pictures of the container fully assembled (Chen, 2001).	38
4.3	Distribution of the accelerometers on the structures.	40
4.4	Time history and frequency spectrum for the scaled Shanghai artificial wave .	41
4.5	Time history and frequency spectrum for the scaled Kobe earthquake record .	42
4.6	Time history and frequency spectrum for the scaled El Centro earthquake record	42
4.7	Cracking of the pile foundation	46
4.8	Flowchart representing how preprocessing was performed	48
4.9	Time history for the absolute acceleration (\ddot{x}), absolute velocity (\dot{x}) and absolute displacement(x)	49
4.10	Time history of the measured restoring force for Shanghai excitation level 6 for the fixed foundation model	51
4.11	Phase Diagrams of the measured restoring force vs displacement for Shanghai excitation level 6 for the fixed foundation model	52
4.12	Phase Diagrams of the measured restoring force vs velocity for Shanghai excitation level 6 for the fixed foundation model	53
4.13	Model order vs the NMSE	55
4.14	Time history of the measured restoring force with the approximated restoring force overlapped for Shanghai excitation level 6 for the fixed foundation model	60
4.15	Phase Diagrams of the measured restoring force vs displacement for Shanghai excitation level 6 for the fixed foundation model	61

4.16	Phase Diagrams of the measured restoring force vs velocity for Shanghai excitation level 6 for the fixed foundation model	62
4.17	3D phase Diagrams of the measured restoring force vs displacement vs velocity for Shanghai excitation level 6 for the fixed foundation model	64
4.18	Identified Chebyshev coefficients for the Shanghai excitation level 6 for the fixed foundation model	65
4.19	Identified power series coefficients for the Shanghai excitation level 6 for the fixed foundation model	67
4.20	Term wise phase Diagrams of the measured restoring force vs displacement for Shanghai excitation level 6 for the fixed foundation model	69
4.21	Term wise phase Diagrams of the measured restoring force vs displacement for Shanghai excitation level 6 for the fixed foundation model	70
4.22	Term wise phase Diagrams of the measured restoring force vs displacement for Shanghai excitation level 6 for the fixed foundation model	71
4.23	Term wise phase Diagrams of the measured restoring force vs displacement for Shanghai excitation level 6 for the fixed foundation model	72
4.24	Term wise phase Diagrams of the measured restoring force vs displacement for Shanghai excitation level 6 for the fixed foundation model	73
4.25	Term wise phase Diagrams of the measured restoring force vs displacement for Shanghai excitation level 6 for the fixed foundation model	74
4.26	Reconstructed mass normalized restoring forces plotted against other reconstructed mass normalized restoring forces for Shanghai excitation level 6 for the fixed foundation model	75
4.27	Term wise phase diagrams of the measured restoring force vs displacement for Shanghai excitation level 6 for the fixed foundation model	77
4.28	Plot of dissipated energy vs peak acceleration for the Shanghai artificial wave record	79
4.29	Plot of dissipated energy vs peak acceleration for the Kobe wave record	79
4.30	Plot of dissipated energy vs peak acceleration for the El Centro wave record	79
4.31	Mode shapes for Shanghai excitation level 1 for the fixed foundation model	80
4.32	Mode shapes for Shanghai excitation level 3 for the box foundation model	81
4.33	Mode shapes for Shanghai excitation level 6 for the pile foundation model	81
4.34	Plot of mass normalized power series coefficients vs peak acceleration for the Shanghai artificial wave record	85
4.35	Plot of mass normalized power series coefficients vs peak acceleration for the Kobe wave record	86
4.36	Plot of mass normalized power series coefficients vs peak acceleration for the El Centro wave record	87
5.1	(a)An offshore wind turbine Source: (Hollman, 2006) (b) a land-based wind turbine Source: (Sherman, 2008)	89

5.2	Three of the subtypes of floating wind turbines Source: (U.S. National Renewable Energy Laboratory, 2011)	92
5.3	Map of Potential Wind Energy In The United States Source: U.S. National Renewable Energy Laboratory (2007)	93
5.4	Photograph of the wind turbine blade	94
5.5	Distribution of the accelerometers on the turbine blade.	96
5.6	Time history of force applied to turbine blade and the associated frequency spectrum.	97
5.7	Time history of acceleration of the turbine blade.	98
5.8	Time history of relative velocity of the turbine blade.	99
5.9	Time history of relative displacement of the turbine blade.	99
5.10	Time history of the measured restoring force for the wind turbine blade	101
5.11	Phase Diagrams of the measured restoring force vs displacement for wind turbine blade	101
5.12	Phase Diagrams of the measured restoring force vs velocity for the wind turbine blade	102
5.13	Model order vs the NMSE for the wind turbine blade	103
5.14	Time history of the measured restoring force with the approximated restoring force overlapped for the wind turbine blade	104
5.15	Phase Diagrams of the measured restoring force vs displacement for wind turbine blade	105
5.16	Phase Diagrams of the measured restoring force and approximated restoring force vs displacement for wind turbine blade	105
5.17	3D phase Diagrams of the measured restoring force vs displacement vs velocity for wind turbine blade	106
5.18	Identified Chebyshev coefficients for the wind turbine blade	107
5.19	Identified power series coefficients for the wind turbine blade	108

LIST OF TABLES

3.1	Properties for linear system analytical simulation	25
3.2	Identified linear system results for known mass	26
3.3	Identified linear system results for unknown mass	26
3.4	Properties for duffing system analytical simulation	28
3.5	Identified duffing system results for known mass	28
3.6	Identified duffing system results for unknown mass	28
3.7	Properties for dead-space nonlinear oscillator analytical simulation	31
3.8	Dead-space nonlinear oscillator NMSE for model order	33
4.1	Key Properties of the Shaking Table Used in the Experiment	37
4.2	Excitation level and its correspond peak acceleration	43
4.3	NMSE of the reconstructed restoring force for the Shanghai excitation	57
4.4	NMSE of the reconstructed restoring force for the Kobe excitation	58
4.5	NMSE of the reconstructed restoring force for the El Centro excitation	59
5.1	Comparison of Advantages and Disadvantages of Offshore and Land-based Wind Turbines.	90
5.2	NMSE for the wind turbine blade elements	103

1 INTRODUCTION

1.1 Problem Statement

As the age of the US infrastructure increases so does damage and fatigues to some critical infrastructure components. These infrastructure components are in need of reliable methods that are able to both, evaluate their health and locate damage. With location and quantification of damage repairs can be made for the continual safe use of these infrastructure components.

As recently as 2013 ASCE has graded the US infrastructure as D+ (ASCE, 2009). The infrastructure is poor shape and some aspects are at risk of collapse. If this problem is ignored; it could result in the loss of life, along with economic losses. A Structural Health Monitoring technique is needed to analyze detect and locate damage on structures.

This study will use the multidegree of freedom Restoring Force Method to accurately locate and detect damages in structures.

1.2 Motivation

The field of Structural Health Monitoring (SHM) is a growing field and has numerous applications in many areas in the discipline of civil engineering and in other disciplines such as aerospace and mechanical engineering. The techniques of SHM can be used in the analysis and damage detection of a number of structures including, but not limited to, wind turbines, bridges, offshore oil rigs, airplanes, and buildings. An extensive literature review was done by Doebling et al. (1996) which covered up to 1996, followed by Sohn et al. (2004), which covered from 1996 to 2001. In the field of SHM evaluation of nonlinear systems is important. This is because most linear systems only behave linearly in their undamaged state; In complex systems the behavior in damaged or undamaged state is often nonlinear. Bornn et al. (2010) found that the

majority of SHM techniques focus on initially linear systems and highlights the inadequacy of linear based methodologies for systems that are initially nonlinear. One example of a nonlinear multidegree of freedom identification technique is the multidegree of freedom Restoring Force Method (MRFM).

1.3 Objectives

This study will focus on testing the validity of the multidegree of freedom Restoring Force Method MRFM on two real world studies. There are several objectives of this study. First, is, testing to see if the MRFM is able to accurately detect damage in a structure. Second, is to see if the method can indicate the location of where the damage has occurred in the structure. Finally, the last objective of this study is to investigate the versatility of the MRFM to non-building structures.

1.4 Scope And Approach

This study will be broken into the analysis of three different data sets. The first data set will be an analytical data set to understand the results of the RFM and how well it works with given data. In the second data set, this study evaluates the performance of this chain-like, nonlinear identification technique on Soil Foundation Structure Interaction (SFSI) under nonstationary random excitation. The data provided by experiments performed at Tongji University, on a relatively large scale, i.e., 1/10 scale, superstructure with multiple foundation types. This provided a very unique and challenging opportunity to evaluate the complex nonlinear response of the superstructure due to SFSI from seismic loads. Various levels of excitations are used which eccentricities the nonlinearities of the superstructures response. This data also presents a good opportunity to use a local identification technique to identify system parameters of the superstructure for change detection. Finally, the last data set which will be analyzed is a preliminary experimental data set collected from a small scale wind turbine blade. This data provides the

opportunity to investigate the application of the RFM to wind turbine blades.

2 RESTORING FORCE METHOD

Yun and Masri (2008) pointed that developing effective Structural Health Monitoring (SHM) methodologies for complex nonlinear systems is challenging. This complexity is increased when the system characteristics are uncertain. These uncertainties pertaining to system characteristics can often arise from uncertainty in system parameters or environmental effects on the system characteristics. Yun and Masri (2008) pointed out several technical challenges to overcome in both parametric and nonparametric SHM methodologies. One of the major problems is over-simplification of system models which occurs through model-order reduction and disregard of environmental effects that may contribute significantly to the system. Another problem is parametric modeling approaches that are incapable of identifying time-varying or deteriorating structures.

The nonlinear identification methodology developed by Yun and Masri (2008) laid out a few select features that must be included in a reliable SHM method. This guide pointed out that first, the method should be able to detect system changes for various types of structural changes. This includes changes to the system parameters and when the system shifts into a different type of nonlinearity. Next, the method must be able to give some physical interpretations to the identified system parameters. A goal of SHM is to assess structural conditions and use this information to help establish operation and maintenance strategies. Because of this goal results should be interpreted with some physical meaning of identification results. This physical meaning should involve the effects of the change on the health of the structure in both a global and local approach. The location of the detected changes should also be included in this physical meaning. Lastly, the method must be able to quantify the uncertainty of the detected changes. This includes measurement uncertainty due to noisy data and uncertainty of the

system parameters. The method should be able to detect true changes to the structure instead of changes based on system uncertainty.

Using these parameters Yun and Masri (2008) proposed a reliable SHM methodology for change detection in nonlinear dynamic systems. This methodology is based on using the Restoring Force Method as the system identification technique.

2.1 Single Degree Of Freedom Restoring Force Method

The Restoring Force Method (RFM) is a nonparametric, nonlinear system identification technique, originally developed by Masri and Caughey (1979). This method was developed to overcome the limitations of other nonlinear identification techniques, such as the Volterra-series or Weiner-kernal. Both suffer from complications: difficulties obtaining convergence rate, long computational times, high storage requirements, only capable of identifying nonhysteretic stationary with white noise as the input. RFM has low sensitivity to noise in the data being processed, low storage requirements, quick computation times and most nonlinear system can be identified.

A nonlinear single-degree-of-freedom (SDOF) system can be expressed as Equation 2.1

$$kx + c\dot{x} = F(t) - m\ddot{x} \quad (2.1)$$

$$m\ddot{x} + G(x, \dot{x}) = F(t) \quad (2.2)$$

where $G(x, \dot{x})$ represents a nonlinear restoring force function that is a function of velocity and displacement.

$$G(x, \dot{x}) = F(t) - m\ddot{x} \quad (2.3)$$

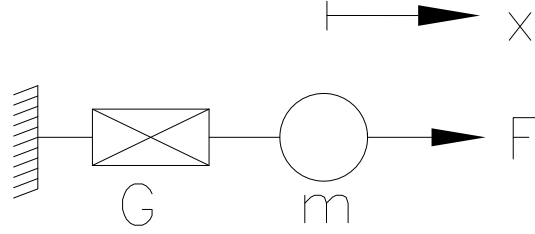


Figure 2.1: A nonlinear, single-degree-of-freedom system.

The basic premise is that the RFM identifies a series of two dimensional orthogonal polynomial coefficients; from a fitted surface of velocity, displacement and the restoring force of a system. Because of the orthogonality of the polynomials, an identified coefficient of order ij is not affected by other coefficients of a different order. This is particularly useful because often times the correct system order is unknown. The polynomial coefficients identified are able to generate an approximate restoring force, which estimates the real restoring force. In this study a series of Chebyshev polynomials are used. The formulation for this approximated restoring force using the Chebyshev polynomials can be seen in Equation 2.4, where T_i is the Chebyshev polynomial of the degree i given by

$$G(x, \dot{x}) \approx \hat{G}(\bar{x}, \bar{\dot{x}}) = \sum_{i=0}^{m2} \sum_{j=0}^{n2} C_{ij} T_i(\bar{x}) T_j(\bar{\dot{x}}) \quad (2.4)$$

$$T_i = \cos(i \arccos(\xi)), -1 < \xi < 1 \quad (2.5)$$

Chebyshev polynomials are only orthogonal over the range of -1 to 1 ; the displacement (x) and velocity (\dot{x}) has to be normalized over this range. This normalization can be accomplished

by the Equation 2.6 for the displacement and Equation 2.7.

$$\bar{x} = [x - (x_{max} + x_{min})/2]/[(x_{max} - x_{min})/2] \quad (2.6)$$

$$\bar{\dot{x}} = [\dot{x} - (\dot{x}_{max} + \dot{x}_{min})/2]/[(\dot{x}_{max} - \dot{x}_{min})/2] \quad (2.7)$$

In equation 2.4, C_{ij} is the Chebyshev coefficient given by equation 2.8.

$$C_{ij} = \begin{bmatrix} (2/\pi)^2 v & i \text{ and } j \neq 0 \\ (2/\pi^2) v & i \text{ or } j = 0 \\ (1/\pi^2) v & i = j = 0 \end{bmatrix}, \quad (2.8)$$

Here in 2.8, the value of v can be found from equation 2.9.

$$v = \int_{x=-1}^1 \int_{y=-1}^1 G(x, y) T_i(x) T_j(y) w(x) w(y) dx dy \quad (2.9)$$

By using the transformations $x = \cos(\theta)$ and $y = \cos(\phi)$, equation 2.9 can be rewritten as
2.10.

$$v = \int_{x=0}^{\pi} \int_{y=0}^{\pi} G(\arccos(x), \arccos(y)) T_i(\theta) T_j(\phi) d\theta d\phi \quad (2.10)$$

To make equation 2.10 solvable by numerical integration, it is made discrete as in equation
2.11

$$v = \sum_{k=1}^{MX2} \sum_{l=1}^{MY2} G_{kl} \cos [i(\Delta\theta)(k-1)] \cos [j(\Delta\phi)(l-1)] \Delta\theta \Delta\phi \quad (2.11)$$

$$\begin{aligned}\Delta\theta &= \pi/MX2 \\ \Delta\phi &= \pi/NX2\end{aligned}\tag{2.12}$$

$$G_{kl} = G(\cos \theta_k, \cos \phi_l)$$

$$\theta_k = (k - 1)\Delta\theta \quad 0 \leq \theta \leq \pi$$

$$\phi_l = (l - 1)\Delta\phi \quad 0 \leq \phi \leq \pi$$

In Equations 2.11 and 2.12, the values for MX and NX are selected by the user. These are the values for the discretization of the the numerical integration. Here G_{kl} is a 3d surface of the restoring force the normalized, transformed velocity and the normalized, transformed displacement. To get points on this surface requires interpolation, in this study Gaussian Radial Basis Functions seen in Equation 2.13 were used in the interpolation.

$$\phi(r) = \exp(-\epsilon r)^2\tag{2.13}$$

where $r = \|x - x_i\|$ and ϵ is the weight of the radial basis function.

The Radial Basis Functions (RBFs) interpolation works by using a series of sum of RBFs, in this study Gaussian, to fit the surface (Fasshauer, 2007).

$$s(x, y) = \sum_{j=1}^N \lambda_j \phi^j(x, y)\tag{2.14}$$

where $s(x, y) = F(x, y)$ where $F(x, y)$ is the surface to be interpolated. Enforcing the interpolation conditions results in $B\lambda = F$ where A is a matrix with entries $B_{ij} = \phi^j(x_i, y_j)$

Interpolation with RBFs offer several distinctive advantages (Carr et al., 1997). First, it is a

mesh-free interpolation which means that there is no restriction for the geometry of the known points. The end product from the interpolation is a smooth single-valued function. Last, RBFs are suited to interpolate scattered data, even when that data contains large dataless areas, because of their variational characterizations.

Since the restoring force method is a nonparametric identification technique, the identified coefficients do not directly reflect any of the stiffness or damping values of the system; however, they can help to indicate certain parameters about the system, such as the linear and nonlinear contribution as indicated by Yun et al. (2008). Those coefficients can also be converted from a Chebyshev series into a power series.

Yun and Masri (2008) took advantage of the fact that while the restoring force method is non-parametric, parametric relation is possible. This can be seen in equation 2.15

$$\hat{G}(x, \dot{x}) = \sum_{i=0}^{m2} \sum_{j=0}^{n2} C_{ij} T_i(\bar{x}) T_j(\bar{\dot{x}}) = \sum_{i=0}^{m2} \sum_{j=0}^{n2} \bar{a}_{ij} \bar{x}^i \bar{\dot{x}}^j = \sum_{i=0}^{m2} \sum_{j=0}^{n2} a_{ij} x^i \dot{x}^j \quad (2.15)$$

where \bar{a}_{ij} represents the normalized power series coefficient and a_{ij} represents the de-normalized power series coefficients, both of which are parametric. By performing a conversion from the identified Chebyshev coefficients into power series coefficients, the results will most likely be different than if an identification was originally accomplished by using a power series. This is a useful approach because the power series can be related to stiffness like and damping like coefficients (Hernandez-Garcia et al., 2010).

2.2 Multi-Degree-Of-Freedom Restoring Force Method

Although the RFM was originally developed for a SDOF system, Masri et al. (1982) developed it into a multidegree of freedom system identification method. The idea behind this development was that each degree could be separated into its own relative single degree of free-

dom system, once the severation is established the single degree of freedom method applies.

Figure 2.2 illustrates a multi-degree-of-freedom (MDOF) chain-like dynamic system, where s is a base excitation, F_k is the force applied to the mass m_k , and the absolute displacement at this mass is measured by x_k . To calculate the interstory relative displacement and velocity of the system, Equations 2.16 and 2.17 can be used respectively.

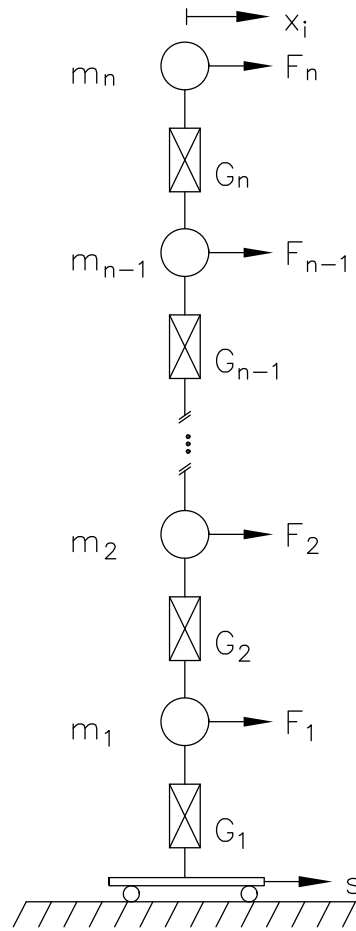


Figure 2.2: A nonlinear, multidegree of freedom system, with unknown restoring forces.

$$z_n = x_n - x_{n-1} \quad (2.16)$$

$$\dot{z}_n = \dot{x}_n - \dot{x}_{n-1} \quad (2.17)$$

$$z_1 = x_1 - s \quad (2.18)$$

$$\dot{z}_1 = \dot{x}_1 - \dot{s} \quad (2.19)$$

where s is the movement of the base of the structure.

A nonlinear element is interposed between the masses m_k and m_{k-1} . This element is represented by G_k , and generates a restoring force $G_k(z_k, \dot{z}_k)$ which is a function of the interstory relative displacement and velocity. For figure 2.2 the equation of motion is described in equation 2.20. It should be noted that all nodes will have the restoring force of the node directly above them contributing to the the force acting upon their structure. Since n would be the top of the structure, it will have no other restoring force other than its own acting upon it.

$$\begin{aligned} m_n \ddot{x}_n &+ G_n(z_n, \dot{z}_n) &= &+ F_n(t) \\ m_{n-1} \ddot{x}_{n-1} &+ G_{n-1}(z_{n-1}, \dot{z}_{n-1}) &= &G_n(z_n, \dot{z}_n) + F_{n-1}(t) \\ &\vdots & & \\ m_2 \ddot{x}_2 &+ G_2(z_2, \dot{z}_2) &= &G_3(z_3, \dot{z}_3) + F_2(t) \\ m_1 \ddot{x}_1 &+ G_1(z_1, \dot{z}_1) &= &G_2(z_2, \dot{z}_2) + F_1(t) \end{aligned} \quad (2.20)$$

The equation 2.20 can be rewritten so that the restoring force appears on the left hand side as seen in equation 2.21.

$$\begin{aligned}
G_n(z_n, \dot{z}_n) &= -m_n \ddot{x}_n + F_n(t) \\
G_{n-1}(z_{n-1}, \dot{z}_{n-1}) &= -m_{n-1} \ddot{x}_{n-1} + G_n(z_n, \dot{z}_n) + F_{n-1}(t) \\
&\vdots \\
G_2(z_2, \dot{z}_2) &= -m_2 \ddot{x}_2 + G_3(z_3, \dot{z}_3) + F_2(t) \\
G_1(z_1, \dot{z}_1) &= -m_1 \ddot{x}_1 + G_2(z_2, \dot{z}_2) + F_1(t)
\end{aligned} \tag{2.21}$$

The restoring force for the nodes can now be calculated the same way as in equation 2.4. This can be represented by equation 2.22.

$$G_{(k)}(z_k, \dot{z}_k) \approx \hat{G}_{(k)}(z_k, \dot{z}_k) = \sum_{i=0}^{m2} \sum_{j=0}^{n2} C_{ij} T_i(\bar{z}_k) T_j(\bar{\dot{z}}_k) \tag{2.22}$$

Now each of the real restoring forces for the i th degree of freedom can be approximated by two dimensional orthogonal polynomials. Again T_i is the Chebyshev polynomial of the i th degree represented by

$$T_i = \cos(i \arccos(\xi)), -1 < \xi < 1 \tag{2.23}$$

Since the Chebyshev polynomials are only orthogonal over the range of -1 to 1, the interstory relative displacement (z) and interstory relative velocity (\dot{z}) had to be normalized over this range. This can be accomplished by the equation 2.24 for the displacement and equation 2.25.

$$\bar{z} = [z - (z_{max} + z_{min})/2]/[(z_{max} - z_{min})/2] \tag{2.24}$$

$$\bar{\dot{z}} = [\dot{z} - (\dot{z}_{max} + \dot{z}_{min})/2]/[(\dot{z}_{max} - \dot{z}_{min})/2] \tag{2.25}$$

In equation 2.22, C_{ij} is the Chebyshev coefficient given by equation 2.8.

$$C_{ij} = \begin{bmatrix} (2/\pi)^2 v & i \text{ and } j \neq 0 \\ (2/\pi^2) v & i \text{ or } j = 0 \\ (1/\pi^2) v & i = j = 0 \end{bmatrix}, \quad (2.26)$$

Here in 2.26, the value of v can be found from equation 2.27, which was transformed and made discrete as in equation.

$$v = \sum_{k=-1}^{MX2} \sum_{l=-1}^{MY2} G_{kl} \cos [i(\Delta\theta)(k-1)] \cos [j(\Delta\phi)(l-1)] \Delta\theta \Delta\phi \quad (2.27)$$

$$\begin{aligned} \Delta\theta &= \pi/MX2 \\ \Delta\phi &= \pi/NX2 \end{aligned} \quad (2.28)$$

$$G_{kl} = G(\cos \theta_k, \cos \phi_l)$$

$$\theta_k = (k-1)\Delta\theta \quad 0 \leq \theta \leq \pi$$

$$\phi_l = (l-1)\Delta\phi \quad 0 \leq \phi \leq \pi$$

Like the SDOF RFM, the Multi-degree-of-freedom Restoring Force Method (MRFM) requires inputs of restoring force, velocity and displacement for all the elements of interest. Velocity and displacement can be measured, but to find the restoring force, mass, acceleration and the input force must be measured.

When the mass is not known, Nayeri et al. (2008) showed that it is possible to still effectively use this method by assuming that the mass is equal for all degrees of freedom of interest i.e. $m_i = m_{i-1} = \dots = m_2 = m_1$. The equation for the restoring force can be normalized by mass

which is done in equation 2.29.

$$\begin{aligned}
\frac{G_n(z_n, \dot{z}_n)}{m_n} &= -\ddot{x}_n + \frac{F_n(t)}{m_n} \\
\frac{G_{n-1}(z_{n-1}, \dot{z}_{n-1})}{m_{n-1}} &= -\ddot{x}_{n-1} + \frac{G_n(z_n, \dot{z}_n)}{m_{n-1}} + \frac{F_{n-1}(t)}{m_{n-1}} \\
&\vdots \\
\frac{G_2(z_2, \dot{z}_2)}{m_2} &= -\ddot{x}_2 + \frac{G_3(z_3, \dot{z}_3)}{m_2} + \frac{F_2(t)}{m_2} \\
\frac{G_1(z_1, \dot{z}_1)}{m_1} &= -\ddot{x}_1 + \frac{G_2(z_2, \dot{z}_2)}{m_1} + \frac{F_1(t)}{m_1}
\end{aligned} \tag{2.29}$$

The mass normalized restoring force can be written as

$$\frac{G_k(z_k, \dot{z}_k)}{m_k} = G_k^m(z_n, \dot{z}_n)$$

This turns equation into 2.30

$$G_k^m(z_k, \dot{z}_k) \approx \hat{G}_k^m(z_k, \dot{z}_k) = \sum_{i=0}^{m2} \sum_{j=0}^{n2} C_{ij}^m T_i(\bar{z}_k) T_j(\bar{\dot{z}}_k) = \sum_{i=0}^{m2} \sum_{j=0}^{n2} a_{ij}^m x^i \dot{x}^j \tag{2.30}$$

It should be noted though, that this results in the Chebyshev coefficients to also be normalized by the unknown mass. This does not usually affect damage detection because damage usually changes the stiffness or damping of the structure of interest and not the mass. If measuring the force acting on the structure is not feasible due to cost or other reasons Nayeri et al. (2008) showed that that if the assumption that the unknown force acting on the structure is a stationary white noise process then the NExT technique can be used and it is not necessary to measure the force. Combing both of these methods increases the number of applications on which RFM can be used, however there are certain constraints; the restoring force had to be assumed linear, the excitation has to be considered low level gaussian white noise and the masses at different elements have to be considered equal to one another.

2.3 Previous Studies Using RFM And MRFM

The RFM is a local identification method as apposed to a global identification methods such as Eigensystem Realization Algorithm (ERA). For the most part, instead of viewing these two different methods as competitive they, should be view as complementary (Nayeri et al., 2008). The local methodology can provide information about a relatively small region of interest through the use of measurements specific to that area, while the global methodology can provide information about the global systems' condition through use of a network of sensors dispersed on the entire structure. However, the local approach may have applications where the global approach can not be used; for very large sensor networks where the processing power and storage requirements are too great, the local approach can still be used because each node is processed individually. However, Nayeri et al. (2008) showed that there was a high degree of error using the local technique based on the RFM. This was attributed to the fact that interstory relative displacement was so small, usually in the order of micrometers, which could be considered within the measurement range of error for the sensors. Nayeri et al. (2008) recommended using a shaker to generate a significant excitation to increase the interstory relative motion since the excitation generated by ambient vibrations are too low.

Hernandez-Garcia et al. (2010) used a three story structure at Los Alamos National Laboratory excited by an electro-dynamic shaker. The goal behind the study was to test the effectiveness of both MRFM and ERA, very similar to what Nayeri et al. (2008) did but without the use of NExT. During the course of their study Hernandez-Garcia et al. (2010) showed that ERA indicated changes, but did so with a high rate of false positives. While the MRFM was demonstrated to effectively, robustly and confidently detect changes in the system and the location of the changes, despite measurement and data processing uncertainties. Because the Chebyshev coefficients that are output from the RFM are normalized, which makes it more difficult to quantify changes, Hernandez-Garcia et al. (2010) decided to use de-normalized power se-

ries coefficients a_{ij} as the dominant restoring force coefficients. The reliable change-sensitive features were shown to be the dominant restoring force coefficients. These can be used for detecting and assessing the degree of the change. The experimental study was also tested against a finite element model to validate the results obtained by the MRFM. Overall the MRFM was shown to be capable of estimating the magnitude of the structural change with more reliability, higher detection rate and good accuracy compared to ERA, (Hernandez-Garcia et al., 2010).

Another significant RFM study was conducted by Yun et al. (2008). This study was on a 1112 kN orifice viscous damper, utilizing several different identification techniques. The study used three different methods: a parametric method based on Maxwell models referred to as the Simplified Design Model (SDM); two nonparametric, one of which was the Single Degree of Freedom (SDOF) RFM; and an Artificial Neural Networks (ANN) identification technique. It was found that all the methods could successfully identify the peak force by using any of the studied methods. The RFM was able to model the damper though with less error than the SDM, while the ANN had the least amount of error of all of the methods studied. The computational time for the RFM was shown to be less than both the SDM and the ANN (Yun et al., 2008)

Yun and Masri (2009) used the RFM in their proposed SHM method for complex nonlinear uncertain systems. The RFM would identify the coefficients and changes were detected with use of statistical pattern recognition techniques. Support vector classification and k-means clustering were used in the study. The detected changes were shown with different levels of system uncertainty. The results from classification were shown to be more robust and have more accurate results when the orthogonal Chebyshev coefficients were used compared to the non-orthogonal power series coefficients. The results from their study further showed that this method can be used for detecting small effective changes, a physical meaning can be interpreted from the detected changes and the uncertainty bounds of the detected changes can be quantified.

Wolfe et al. (2002) did a study on SHM methods for nonlinear viscous dampers. Of partic-

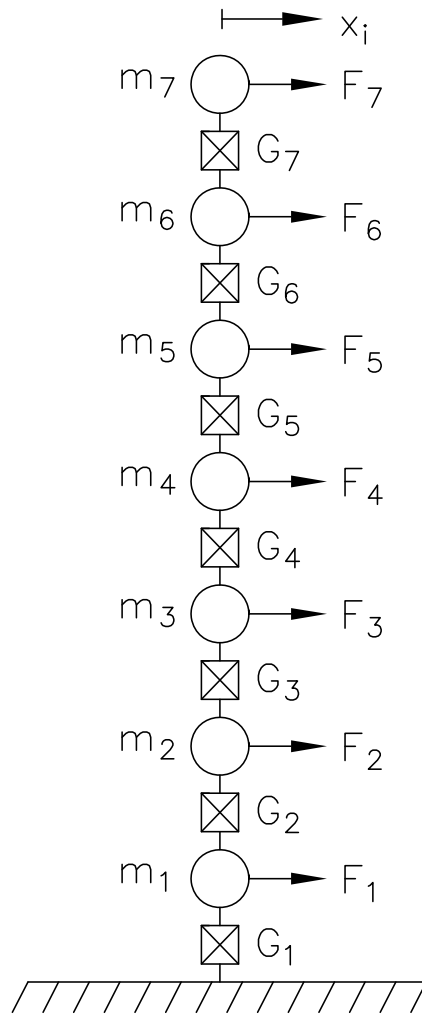
ular interest was the sensitivity of the proposed approach, based on the RFM, to detect small changes in the system characteristics of a nonlinear viscous damper with noise-polluted synthetic data. Both analytical and experimental studies were conducted. Their study successfully demonstrated that even at a 10% noise pollution, that the system coefficients could be identified with a very low error rate, about 7% for the stiffness characteristics; however for the damping characteristics the error was higher at around 55%. To quantify the effects of variations in the system stiffness parameters a Monte Carlo simulation was used.

3 ANALYTICAL STUDY: SYSTEM IDENTIFICATION FOR MULTI-DEGREE-OF-FREEDOM OSCILLATORS

This chapter presents a number of analytical dynamic models for a better understanding of the capabilities and limits of the MRFM. In all of these studies the system parameters were selected and used to create the data sets. A linear multi-degree of freedom system along with various types of nonlinear multi-degree of freedom models were used in order to ensure the quality of the Restoring Force Method system identification technique and its ability to replicate the restoring force with an approximated solution.

3.1 Examples Of Oscillators

MDOF models of three common oscillators are presented: (a) linear, (b) duffing, and (c) dead-space nonlinear oscillators. Figure 3.1 shows a generic 7-DOF which can represent any of these oscillators, where m_n is the mass, G_n is the nonlinear element interposed between the masses, and F_n is the force applied at the mass.



(a) G_7

Figure 3.1: Seven-degree-of-freedom system which can be representative of any nonlinear oscillators.

The linear MDOF model can be described by Equation 3.1. This shows the general equation for a linear multidegree of freedom system with only interstory connections.

$$\begin{aligned}
m_n \ddot{z}_n + c_n \dot{z}_n + k_n z_n &= f_n(t) \\
m_{n-1} \ddot{z}_{n-1} + c_{n-1} \dot{z}_{n-1} + k_{n-1} z_{n-1} &= c_n \dot{z}_n + k_n z_n + f_{n-1}(t) \\
\vdots & \\
m_2 \ddot{z}_2 + c_2 \dot{z}_2 + k_2 z_2 &= c_3 \dot{z}_3 + k_3 z_3 + f_2(t) \\
m_1 \ddot{z}_1 + c_1 \dot{z}_1 + k_1 z_1 &= c_2 \dot{z}_2 + k_2 z_2 + f_1(t)
\end{aligned} \tag{3.1}$$

where c_n and k_n represent the damping and stiffness constants at the n th degree of freedom.

The duffing MDOF model can be described by Equation 3.2. This shows the general equation for a duffing multidegree of freedom system with only interstory connections. Duffing is

$$\begin{aligned}
m_n \ddot{z}_n + c_n \dot{z}_n + k_n^1 z_n + k_n^3 (z_n)^3 &= f_n(t) \\
m_{n-1} \ddot{z}_{n-1} + c_{n-1} \dot{z}_{n-1} + k_{n-1}^1 z_{n-1} + k_{n-1}^3 (z_{n-1})^3 &= \\
c_n \dot{z}_n + k_n^1 z_n + k_n^3 (z_n)^3 + f_{n-1}(t) & \\
\vdots & \\
m_2 \ddot{z}_2 + c_2 \dot{z}_2 + k_2^1 z_2 + k_2^3 (z_2)^3 &= \\
c_3 \dot{z}_3 + k_3^1 z_3 + k_3^3 (z_3)^3 + f_2(t) & \\
m_1 \ddot{z}_1 + c_1 \dot{z}_1 + k_1^1 z_1 + k_1^3 (z_1)^3 &= \\
c_2 \dot{z}_2 + k_2^1 z_2 + k_2^3 (z_2)^3 + f_1(t) &
\end{aligned} \tag{3.2}$$

where k_n^1 and k_n^3 are stiffness coefficients at the n th degree of freedom. At large displacements the k_n^3 is expected to be the dominant restoring force term because it is attached to a cubic

exponentiation of relative displacement.

The dead-space MDOF model can be described by equation 3.3.

$$\begin{aligned}
m_n \ddot{z}_n &+ c_n \dot{z}_n &+ k_n(z_n - g_n)[g_n \leq |z_n|] &= & f_n(t) \\
m_{n-1} \ddot{z}_{n-1} &+ c_{n-1} \dot{z}_{n-1} &+ k_{n-1}(z_{n-1} - g)[g_{n-1} \leq |z_{n-1}|] &= & \\
& c_n \dot{z}_n &+ k_n(z_n - g_n)[g_n \leq |z_n|] + & f_{n-1}(t) \\
& \vdots & & (3.3) \\
m_2 \ddot{z}_2 &+ c_2 \dot{z}_2 &+ k_2(z_2 - g)[g_2 \leq |z_2|] &= & \\
& c_3 \dot{z}_3 &+ k_3(z_3 - g_3)[g_3 \leq |z_3|] + & f_2(t) \\
m_1 \ddot{z}_1 &+ c_1 \dot{z}_1 &+ k_1(z_1 - g)[g_1 \leq |z_1|] &= & \\
& c_3 \dot{z}_2 &+ k_2(z_2 - g_2)[g_2 \leq |z_2|] + & f_1(t)
\end{aligned}$$

where g_n represents the size of the dead-space. Note the use of Iverson brackets $[]$ which are evaluated at 0 if the condition isn't meet and at 1 if the condition is meet.

3.2 Analytical Simulation

For all the dynamic systems in this chapter they were created and analyzed in Simulink, a tool for simulating and modeling dynamics systems. Simulink is well integrated into MATLAB and can either take commands or give commands to MATLAB. The importance of Simulink in this study comes from its ability to numerically solve differential equations. All of the dynamic equations for this study are either linear or nonlinear second order differential equation. To numerically solve these equations, a fourth-order Runge-Kutta method will be used. The fourth-order Runge-Kutta is used because it gives accurate values for many dynamic systems. Zill and Cullen (2006) shows the Runge-Kutta method as follows:

$$\begin{aligned}
y_{n+1} &= y_n + \frac{h}{6}(k_1 + 2k_2 + 3k_3 + k_4) \\
k_1 &= f(x_n, y_n) \\
k_2 &= f(x_n + \frac{1}{2}h, y_n + \frac{1}{2}hk_1) \\
k_3 &= f(x_n + \frac{1}{2}h, y_n + \frac{1}{2}hk_2) \\
k_4 &= f(x_n + h, y_n + hk_3) \\
y' &= f(x, y)
\end{aligned} \tag{3.4}$$

here h is a step-size. The step-size must be chosen by the user, when picking a step-size it is important for it to be small enough to reduce error but if too small will require too much computation time and memory from the computer. The size is important because the Runge-Kutta is a numerical method and with a larger step sizes the error for each step is increased this will give flawed results. The displacement is represented by x_n at step n where if $n = 0$ is the initial condition for the displacement. Similarly y_n is the velocity at step n and again can be described by the initial condition if $n = 0$.

To create a dynamic model in Simulink Equations 3.1, 3.2 and 3.3 will be rewritten as ordinary inhomogeneous second-order differential equations and will be solved for in terms of acceleration \ddot{z} . An example for how this can be done for the for Equation 3.1 can be seen in Equation 3.5

$$\begin{aligned}
\ddot{z}_7 &= -\frac{c_7 \dot{z}_7}{m_7} - \frac{k_7 z_7}{m_7} + \frac{c_7 \dot{z}_7}{m_7} \\
\ddot{z}_6 &= -\frac{c_6 \dot{z}_6}{m_6} - \frac{k_6 z_6}{m_6} + \frac{c_7 \dot{z}_7}{m_6} + \frac{k_7 z_7}{m_6} + \frac{f_6(t)}{m_6} \\
\ddot{z}_5 &= -\frac{c_5 \dot{z}_5}{m_5} - \frac{k_5 z_5}{m_5} + \frac{c_6 \dot{z}_6}{m_5} + \frac{k_6 z_6}{m_5} + \frac{f_5(t)}{m_5} \\
\ddot{z}_4 &= -\frac{c_4 \dot{z}_4}{m_4} - \frac{k_4 z_4}{m_4} + \frac{c_5 \dot{z}_5}{m_4} + \frac{k_5 z_5}{m_4} + \frac{f_4(t)}{m_4} \\
\ddot{z}_3 &= -\frac{c_3 \dot{z}_3}{m_3} - \frac{k_3 z_3}{m_3} + \frac{c_4 \dot{z}_4}{m_3} + \frac{k_4 z_4}{m_3} + \frac{f_3(t)}{m_3} \\
\ddot{z}_2 &= -\frac{c_2 \dot{z}_2}{m_2} - \frac{k_2 z_2}{m_2} + \frac{c_3 \dot{z}_3}{m_2} + \frac{k_3 z_3}{m_2} + \frac{f_2(t)}{m_2} \\
\ddot{z}_1 &= -\frac{c_1 \dot{z}_1}{m_1} - \frac{k_1 z_1}{m_1} + \frac{c_2 \dot{z}_2}{m_1} + \frac{k_2 z_2}{m_1} + \frac{f_1(t)}{m_1}
\end{aligned} \tag{3.5}$$

All of the cases will be a 7 DOF system with excitation at only the first level and analysis will only be conducted on the top 6 degrees of freedom. All cases will be analyzed knowing fully what the restoring force is and analyzed not knowing what the restoring force is and finding the mass normalized restoring force following the formulation from Equation 2.29.

The following simulation factors will be used:

- Time length will be 200 seconds with a time step of 0.01 seconds
- Excitation will be provided by a broadband random root-mean-square force, with a frequency range from 0.1 Hz to 5 Hz and a scale of 1.5 and an offset of 0.0...

Individual model parameters will be discussed in their respective sections. Error will be calculated using the percent error formula in Equation 3.6

$$Error = \frac{|Approximate - Exact|}{Exact} 100\% \tag{3.6}$$

The individual code used in Simulink to model all 3 of the system types can be found in the Appendix.

3.3 System Identification

In this section the samples cases will be analyzed using the MRFM and discussion will follow explaining the significance of these various results.

3.3.1 Linear System

A linear case was created this will be the simplest case of all analyzed. The case will first be analysed as if the mass is known and the restoring force will be calculated and a second case with unknown mass and the mass normalized restoring force will be calculated. The properties of the system can be found in Table 3.1 since the properties are known the results will be compared and the error will be calculated what the difference is. The results can be seen in Tables 3.2 and 3.3.

Table 3.1: Properties for linear system analytical simulation.

<i>Linear System Properties</i>			
<i>Element</i>	<i>Mass (kg)</i>	<i>Stiffness (kg/s²)</i>	<i>Damping (kg/s)</i>
7	2	0.50	0.01
6	2	0.75	0.01
5	2	1.00	0.01
4	2	1.25	0.01
3	2	1.5	0.01
2	2	1.75	0.01

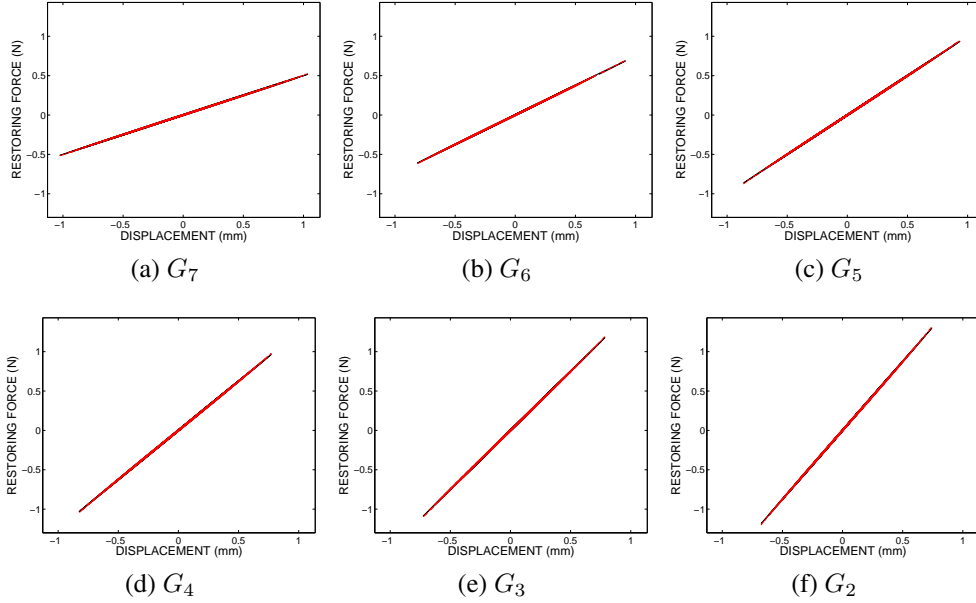


Figure 3.2: Linear phase diagrams of the restoring force vs displacement with reconstructed restoring force at (a) G_7 (b) G_6 (c) G_5 (d) G_4 (e) G_3 (f) G_2 .

Table 3.2: Identified linear system results for known mass.

<i>Known Mass Linear System Identification Results</i>						
<i>Element</i>	<i>Stiffness (kg/s²)</i>	<i>Identified Stiffness (kg/s²)</i>	<i>(Error) (%)</i>	<i>Damping (kg/s)</i>	<i>Identified Damping (kg/s)</i>	<i>(Error) (%)</i>
7	0.50	0.496	0.78	0.01	0.009	0.64
6	0.75	0.745	0.71	0.01	0.009	0.76
5	1.00	0.993	0.74	0.01	0.009	0.74
4	1.25	1.241	0.74	0.01	0.009	0.75
3	1.5	1.489	0.74	0.01	0.009	0.75
2	1.75	1.737	0.73	0.01	0.009	0.75

Table 3.3: Identified linear system results for unknown mass. All properties are the mass normalized coefficients.

<i>Unknown Mass Linear System Identification Results</i>						
<i>Element</i>	<i>Stiffness (1/s²)</i>	<i>Identified Stiffness (1/s²)</i>	<i>(Error) (%)</i>	<i>Damping (1/s)</i>	<i>Identified Damping (1/s)</i>	<i>(Error) (%)</i>
7	0.25	0.248	0.78	0.01	0.005	0.64
6	0.375	0.372	0.71	0.01	0.005	0.76
5	0.50	0.496	0.74	0.01	0.005	0.74
4	0.625	0.620	0.74	0.01	0.005	0.75
3	0.75	0.745	0.74	0.01	0.005	0.75
2	0.875	0.869	0.73	0.01	0.005	0.75

Discussion And Conclusions

The results show that with either a known or unknown mass the restoring force method can accurately describe the linear system characteristics with minimum error. In fact using either method results in the same error as the other case for each element. So whether the mass is known or unknown do not directly affect the results, as long as the assumption used, that the masses are equal to each other is true.

3.3.2 Duffing System

A duffing case was created next. This will be the simplest of all nonlinear system analyzed. The case will first be analysed as if the mass is known and the restoring force will be calculated and a second case with unknown mass and the mass normalized restoring force will be calculated. The properties of the system can be found in Table 3.4 since the properties are known the results will be compared and the error will be calculated what the difference is. The results can be seen in Tables 3.5 and 3.6.

Table 3.4: Properties for duffing system analytical simulation.

<i>Duffing System Properties</i>				
<i>Element</i>	<i>Mass (kg)</i>	k^1 (kg/s ²)	k^3 (kg/mm ² s ²)	<i>Damping (kg/s)</i>
7	2.00	2.00	0.75	0.01
6	2.00	1.75	1.00	0.01
5	2.00	1.50	1.25	0.01
4	2.00	1.25	1.50	0.01
3	2.00	1.00	1.75	0.01
2	2.00	0.75	2.00	0.01

Table 3.5: Identified duffing system results for known mass.

<i>Duffing System Properties</i>						
<i>Element</i>	<i>True</i> k^1 (kg/s ²)	<i>Identified</i> k^1 (kg/s ²)	<i>Error</i> %	<i>True</i> k^3 (kg/mm ² s ²)	<i>Identified</i> k^3 (kg/mm ² s ²)	<i>Error</i> %
7	2.00	1.98	0.79	0.75	0.94	25.39
6	1.75	1.73	0.80	1.00	1.16	16.29
5	1.50	1.49	0.58	1.25	1.40	12.48
4	1.25	1.23	1.00	1.50	1.62	8.33
3	1.00	0.98	1.46	1.75	1.85	5.62
2	0.75	0.74	0.96	2.00	2.08	4.31

Table 3.6: Identified duffing system results for unknown mass. All properties are the mass normalized coefficients.

<i>Duffing System Properties</i>						
<i>Element</i>	<i>True</i> k^1 (1/s ²)	<i>Identified</i> k^1 (1/s ²)	<i>Error</i> %	<i>True</i> k^3 (1/mm ² s ²)	<i>Identified</i> k^3 (1/mm ² s ²)	<i>Error</i> %
7	1.00	0.99	0.79	0.375	0.47	25.39
6	0.875	0.865	0.80	0.50	0.58	16.29
5	0.75	0.745	0.58	0.625	0.70	12.48
4	0.625	0.615	1.00	0.75	0.81	8.33
3	0.50	0.49	1.46	0.875	0.925	5.62
2	0.375	0.37	0.96	1.00	1.04	4.31

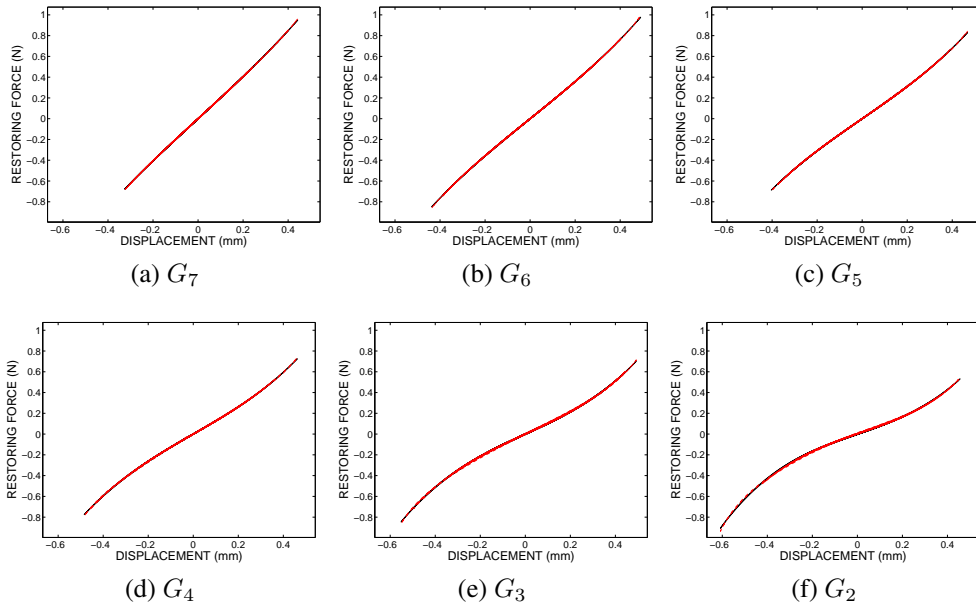


Figure 3.3: Duffing phase diagrams of the restoring force vs displacement with reconstructed restoring force at (a) G_7 (b) G_6 (c) G_5 (d) G_4 (e) G_3 (f) G_2 .

Discussion And Conclusions

The results show that with either a known or unknown mass the restoring force method can accurately describe the duffing system characteristics with some error. All though the values are not that different because of there size the error is greatly exaggerated, in later chapters a different method will be used to calculate the error. Like the linear system though it is shown that using either method unknown or known mass, results in the same error for each element. So weather the mass is known or unknown do not directly affect the results, as long as the assumption used, that the masses are equal to each other is true.

3.3.3 Dead-Space Nonlinear System

The last case to analyze is the Gap space case. This is the most complicated nonlinear system that will be analyzed in this study. Like the previous two systems it has physical damping and stiffness but it also has an additional system property which is a physical dead-space. During this dead-space there is no stiffness to resist movement, the dead-space can be seen in many systems an example is a gear, this dead-space exist until the teeth hit together and can vary in size based on the size of the gears teeth, there are additional examples of dead-spaces beyond just gears though. Since, the only way to measure a dead-space is through plotting of the phase diagram, and the RFM can not measure the dead-space, instead it will be shown how the RFM can approximate the restoring force using higher order coefficients. The properties of the dead-space space model are seen in Table 3.8.

Table 3.7: Properties for dead-space nonlinear oscillator analytical simulation.

<i>Dead-Space Nonlinear Oscillator Properties</i>				
<i>Element</i>	<i>Mass (kg)</i>	<i>Stiffness(kg/s²)</i>	<i>Dead-Space Size (mm)</i>	<i>Damping (kg/s)</i>
7	2.00	0.50	0.50	0.01
6	2.00	0.75	1.00	0.01
5	2.00	1.00	1.50	0.01
4	2.00	1.25	2.00	0.01
3	2.00	1.50	2.50	0.01
2	2.00	1.75	3.00	0.01

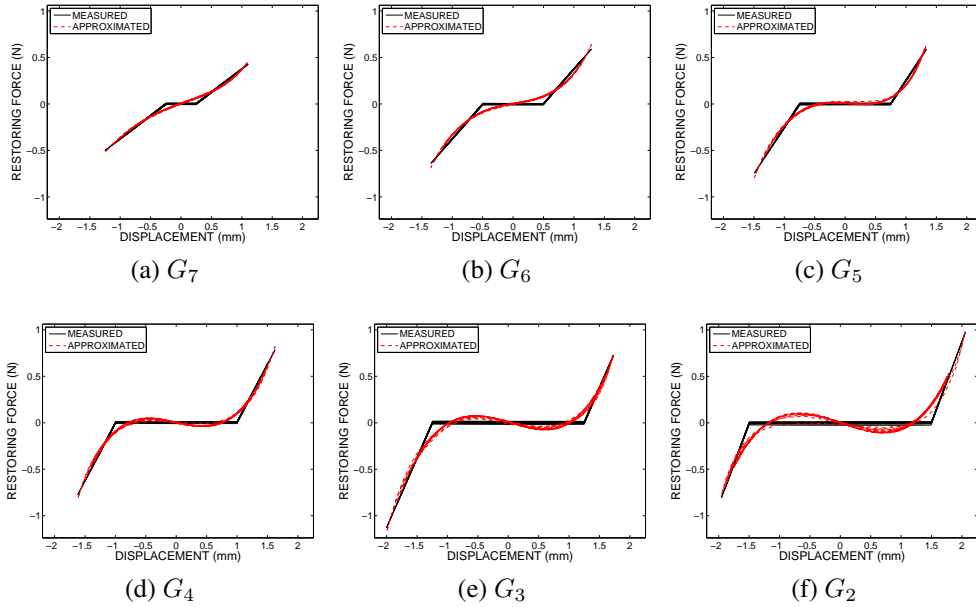


Figure 3.4: Phase diagrams of the restoring force vs displacement with reconstructed restoring force using up to the 4th order Chebyshev coefficients at (a) G_7 (b) G_6 (c) G_5 (d) G_4 (e) G_3 (f) G_2 .

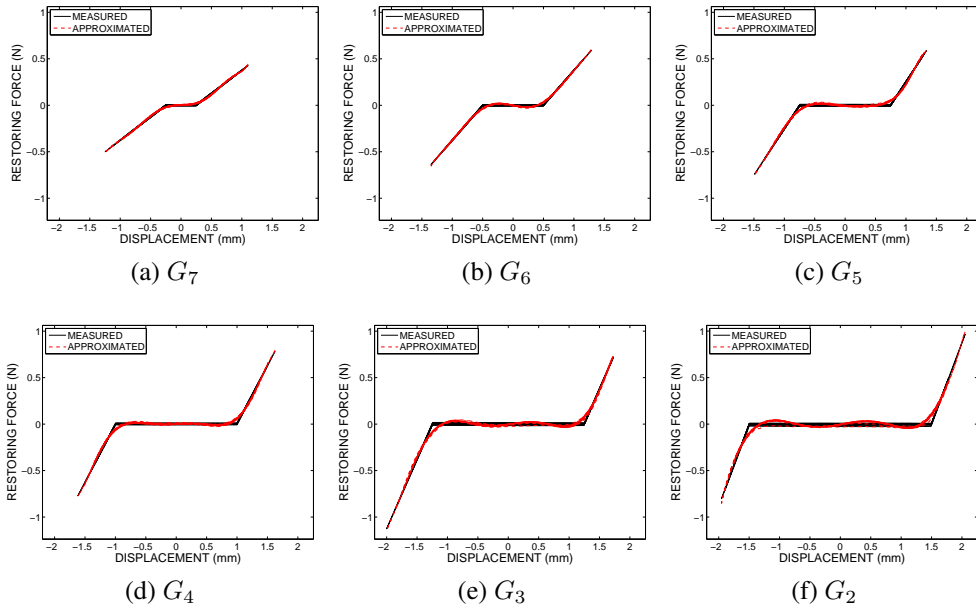


Figure 3.5: Phase diagrams of the restoring force vs displacement with reconstructed restoring force using up to the 8th order Chebyshev coefficients at (a) G_7 (b) G_6 (c) G_5 (d) G_4 (e) G_3 (f) G_2 .

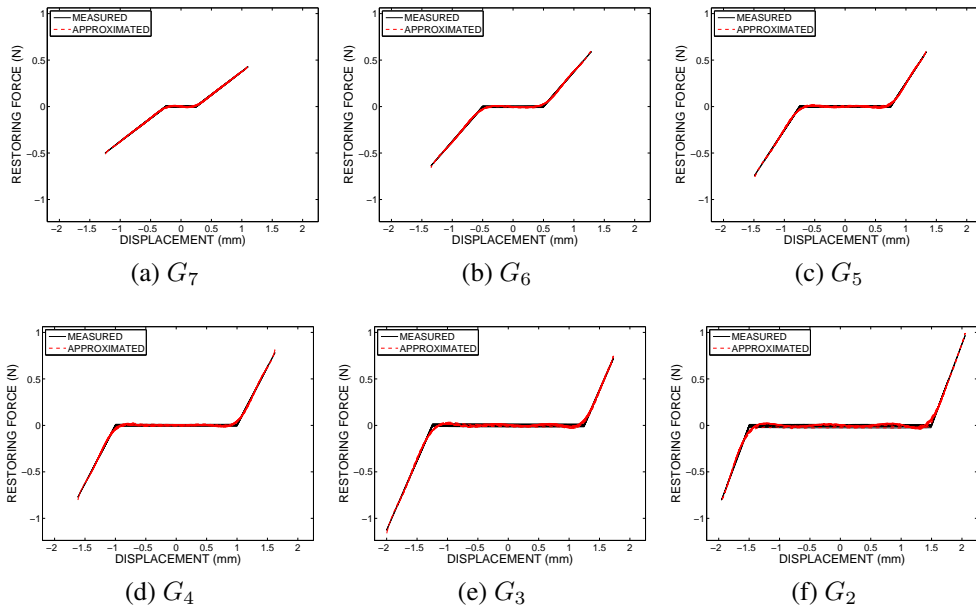


Figure 3.6: Phase diagrams of the restoring force vs displacement with reconstructed restoring force using up to the 12th order Chebyshev coefficients at (a) G_7 (b) G_6 (c) G_5 (d) G_4 (e) G_3 (f) G_2 .

Table 3.8: Dead-space nonlinear oscillator NMSE for model order.

<i>Dead-Space Nonlinear Oscillator Properties</i>						
<i>Element</i>	<i>Dead-Space Size (mm)</i>	<i>5th Order NMSE %</i>	<i>7th Order NMSE %</i>	<i>9th Order NMSE %</i>	<i>11th Order NMSE %</i>	<i>12th Order NMSE %</i>
7	0.50	0.80	0.24	0.10	0.04	0.04
6	1.00	0.63	0.40	0.33	0.21	0.20
5	1.50	1.63	0.92	0.28	0.23	0.19
4	2.00	3.36	0.64	0.68	0.24	0.25
3	2.50	7.54	1.57	1.67	0.58	0.54
2	3.00	6.34	5.14	1.78	1.72	1.65

Discussion And Conclusions

The results of Figures 3.4, 3.5 and 3.6, show how using the higher order coefficients closer fits to the sharp edges of the dead-space can be achieved. Even when the dead-space is very large an excellent fit can found, however finding such a fit requires higher order coefficients to be used.

3.4 Conclusions From The Analytical Study

Several conclusions can be drawn from these analytical studies. It was seen that for the various types of nonlinearities presented either a close match to their system characteristics were found or the restoring force their characteristics generated could be closely matched with high orders of the two dimensional orthogonal Chebyshev polynomials. This gives confidence in using the restoring force.

4 EXPERIMENTAL NONLINEAR IDENTIFICATION FOR BUILDING STRUCTURES WITH DIFFERENT FOUNDATION TYPES

4.1 Experimental Setup

4.1.1 Background

Soil structure interactions can change the dynamic characteristics of the structure (Nayeri et al., 2008). To better understand This experimental setup, designed by researchers at Tongji University, Shanghai, China, was meant to help understand the entire structure system, which includes the superstructure and foundation system.

4.1.2 Equipment

To understand these SFSI, the test made use of a 1:10 scaled 12-story cast-in-place reinforced concrete frame building models and used three different foundations types: fixed, pile and box. Various seismic loading conditions were used. For the fixed foundation type the scale model building was rigidly attached to the tabletop. However, during the box and pile foundation testing, the foundations were set into a soil container.

Soil Container

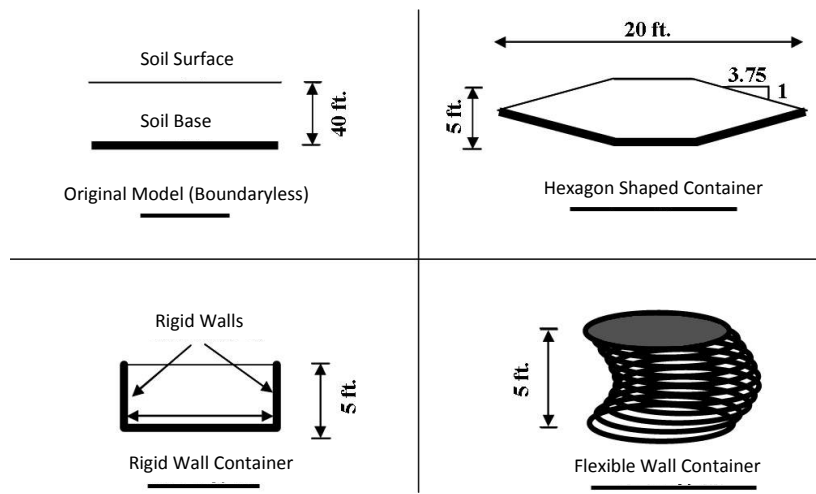
To try and imitate these SFSI seen in a real world example, selection of the soil container was very important as the improper selection would result in significant error in the data. Since real world conditions would have no boundary, the soil container had to be designed to have the same deformation as an infinite dimension container. With boundaries, the waves are reflected off the boundaries and effects the system. This is called the “box-effect”. To determine the best way to reduce this ”box-effect”, several boundary simulation methods were used to select the optimal soil container, the different boundaries used can be seen in Figure 4.1 (a). These

containers and their responses can be seen in Figure 4.1 (b). By looking at the Figure it can be seen how closely the flexible wall container matched to the boundaryless model, while the rigid wall and hexagon containers do not match closely to the boundaryless model. Based on this, it was decided that the container that imitated the natural conditions the best was a flexible cylindrical container. It was also found that the error from the boundary is very small and stable when D , the diameter of the ground plane, divided by d , the base of the structure, is greater than or equal to 5, e.i., $D/d \geq 5$. The container was finally designed to the following specifications of a 5 mm flexible rubber membrane, with a 3000 mm diameter.

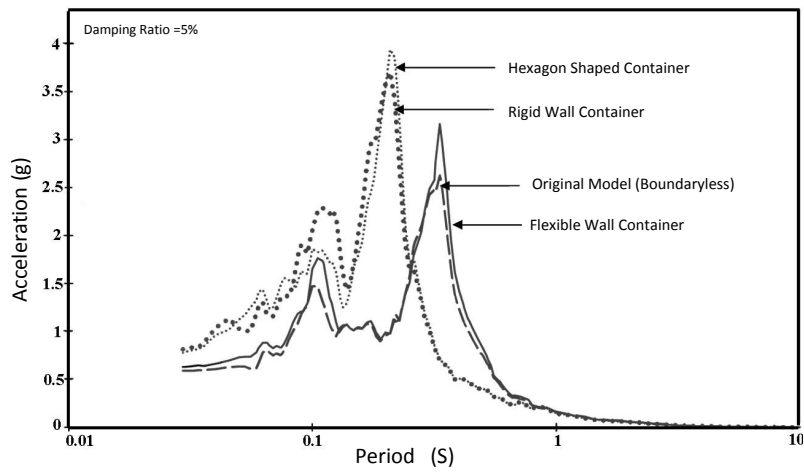
Reinforcement was added to the outside of the container, providing radial rigidity and allows for the soil to have shear deformation in the horizontal direction. These reinforcement loops were made of welded steel bars. A top plate, with a large diameter hole cut out, held the flexible rubber membrane, and the two were secured using bolts. The top plate was supported by four columns fixed to the base plate. The rubber membrane was also secured to the base plate with bolts. The column supporting the top plate had a universal joint between the column and the top plate, allowing the top plate to displace. Final pictures of the soil container can be seen in Figure 4.2. Crushed rock was epoxied to the floor of the container to prevent the soil from slipping.

Shaker Table

All tests were performed on a electro-hydraulic shaking table at the State Key Laboratory of Tongji University and performed by the shaking table division. The shaking table was produced by MTS. Key properties of the shaking table can be found in Table 4.1.



(a) Tongji Models



(b) Tongji Acceleration Response Foundation

Figure 4.1: (a) The container models (b) the responses used in the boundary simulation (Chen, 2001).

Table 4.1: Key Properties of the Shaking Table Used in the Experiment

Table Dimension	4.0m x 4.0m
Maximum Specimen Weight	25 ton
Vibration Direction	X, Y, Z
Degrees of Freedom	6
Maximum Acceleration in X, Y and Z respectively	1.2g, 0.8g, 0.7g
Frequency of Operation	0.1 Hz 50Hz



(a) Vertical view of soil container



(b) Horizontal view of soil container

Figure 4.2: Pictures of the container fully assembled. (a) A vertical view of the soil container (b) a horizontal view of the container with translation of the Chinese characters is ‘Shaking table tests of structural soil system’ (Chen, 2001).

4.1.3 *Sample Preparation*

Because of the dimensional transformation from the real world version down to a scaled model, it was important to take into account the change to the geometric shapes, material properties, boundary conditions and external influence. The new physical properties should be analogues to the real world properties; however, the reliability of the data produced from these experiments depends on whether the scaled model is indeed similar to real world conditions. Since the main purpose of this experiment was to study the structure foundation system dynamic, the following principles of the model design were determined. The principles are as follows: the soil, foundation and superstructure should follow the same similarity relation; allow gravity distortion, even though it is very difficult to do so without additional weight on the system; the dynamic loading parameters should be controlled to satisfy the requirements of the vibration table performance parameters; and the model can not exceed capacity of the lab equipment capacity.

Following these established principles, the tests adopted the material of the real world structure, but had to ignore the gravity deformation. To derive the physical quantities, the Buckingham Pi Theorem was used. Which is a key theorem in dimensional analysis and one of the most popular (Finnemore and Franzini, 2001). Pi theorem allows for n dimensional variables involved in some physical phenomenon to be written in a dimensionally homogenous equation. For the real world building a two-way single span of 12 layer reinforced cast-in-place concrete frame was used, the soil was made of Shanghai soft soil. The soil foundation and superstructure were all designed according to the similitude relation. The concrete used for the model had coarse aggregate that contained larger than standard concrete coarse aggregate diameter and the fine aggregate diameter was smaller than standard concrete fine aggregate diameter. With the construction methods and material properties of the concrete for the model, the similarity relation to standard concrete is close. With the adjustment to the mix design of the concrete, a

lower modulus of elasticity is achieved. The soil water was added and was stirred appropriately to match the characteristics of the soil to that of the real world building. Before the testing, the models' materials were all tested to check the performance parameters of the materials.

4.1.4 Instrumentation

It was important for the system to gather as much information as possible. For this reason it was instrumented with; accelerometers, strain gauges, pore pressure and soil pressure gauges. These were installed to acquire different information about the SFSI system. Because of the choice to use the RFM for the analysis in this study, only the data from the accelerometers will be used. The locations of the accelerometers can be seen in Figure 4.3. These accelerometers only measured the acceleration in the X-direction. A0 is the acceleration of the shaker table, A1 is the start of the superstructure and A7 is the top of the superstructure. Accelerometers were placed on every other floor between A1 and A7. The accelerometers will be used in the calculation of mass normalized restoring force, interstory relative velocity and interstory relative displacement.

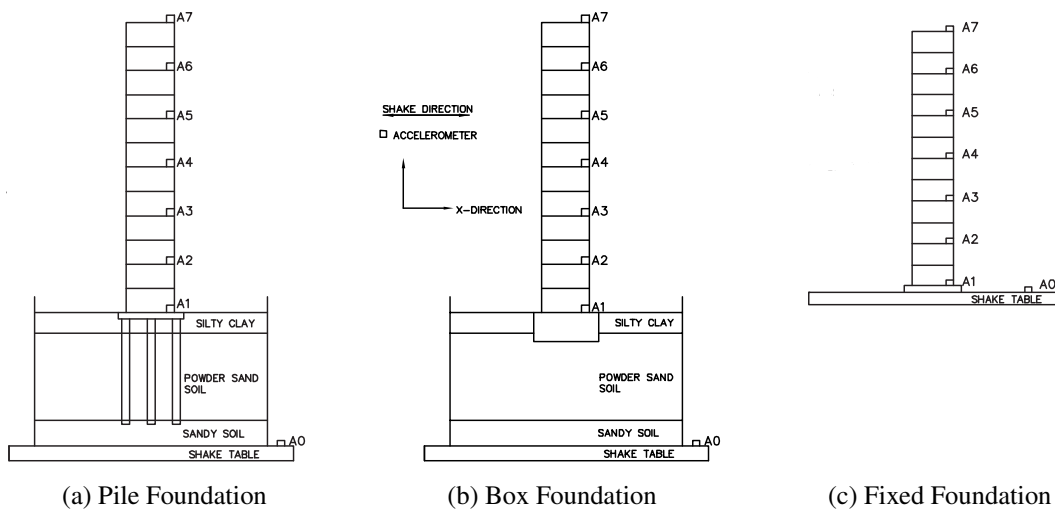


Figure 4.3: Distribution of the accelerometers on the structure for (a) The pile foundation model (b) The box foundation model (c) The fixed foundation model.

4.1.5 Excitation

To properly excite the building it was important for the proper selection of seismic waves. The seismic waves selected for the test consist of the Shanghai artificial wave record (SH), the Kobe earthquake record (KB), and El Centro earthquake record (EL). A description of these waves follows.

The first source was the Shanghai artificial wave. The main excitation lasts for about 50 seconds and the entire length is around 78 seconds. It is a broadband frequency, so it has higher frequencies not seen in historical earthquake records. Also like the other seismic waves, it had to be adjusted by Buckingham Pi theorem. The scaled time history of acceleration and its respected FFT for the Shanghai artificial wave can be seen in figure 4.4 (a) and (b) respectively.

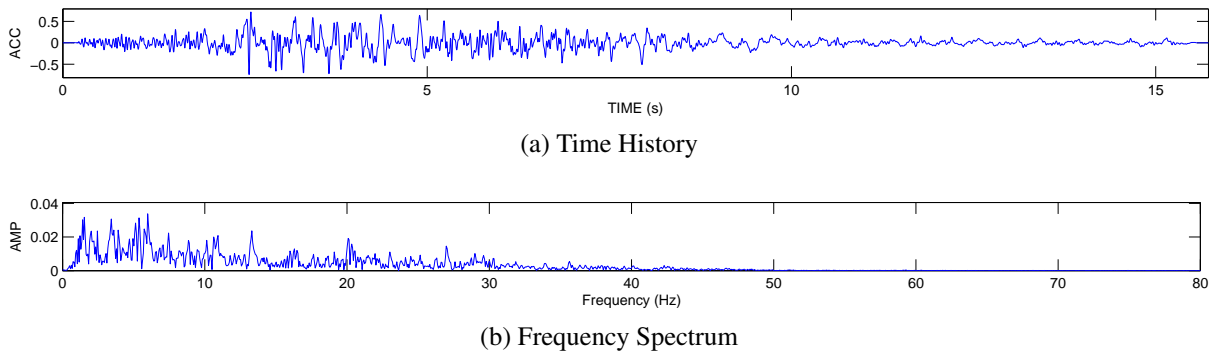


Figure 4.4: Shanghai artificial wave plots for (a) The scaled acceleration time history for the Shanghai artificial wave (b) The frequency spectrum for the scaled Shanghai artificial wave.

The next source was the Kobe earthquake record is from the Great Hanshin earthquake that happen on January 17th, 1995, in Japan with an epicenter around 20 km from the city of Kobe. This earthquake was recorded by the Kobe ocean observatory 0.4km from the epicenter. It measured a magnitude of 6.8 (Person, 1997). The north-south component was used as the x-direction input in to the test. Again for this test the time and peak acceleration had to be adjusted by the Buckingham Pi theorem. The scaled time history of acceleration and its respected FFT for the Kobe earthquake record can be seen in figure 4.5 (a) and (b) respectively.

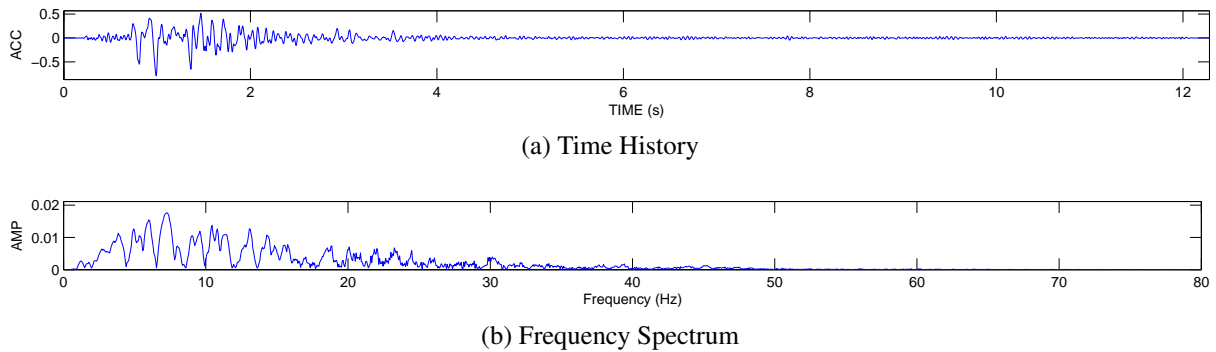


Figure 4.5: Kobe earthquake record plots for (a) The scaled acceleration time history for the Kobe earthquake record (b) The frequency spectrum for the scaled Kobe earthquake record.

The final source was the El Centro earthquake record was recorded by the El Centro Station on May 18th, 1940 during the El Centro earthquake that occurred in the Imperial Valley, near the California, USA and Mexican border (Stover and Coffman, 1993). For the test the north-south acceleration data from the El Centro earthquake was used (a classic record used in many structural test) The main excitation lasted about 26 seconds long and the magnitude was 7.1. For the test though the time and peak acceleration had to be adjusted by the Buckingham Pi theorem. The scaled x-direction (N-S component) time history of acceleration for the El Centro earthquake record and its respected FFT can be seen in figure 4.6 (a) and (b) respectively. The El Centro 1940 earthquake record is commonly used in design applications (Chopra, 2006), this is a large reason for choosing to use this excitation.

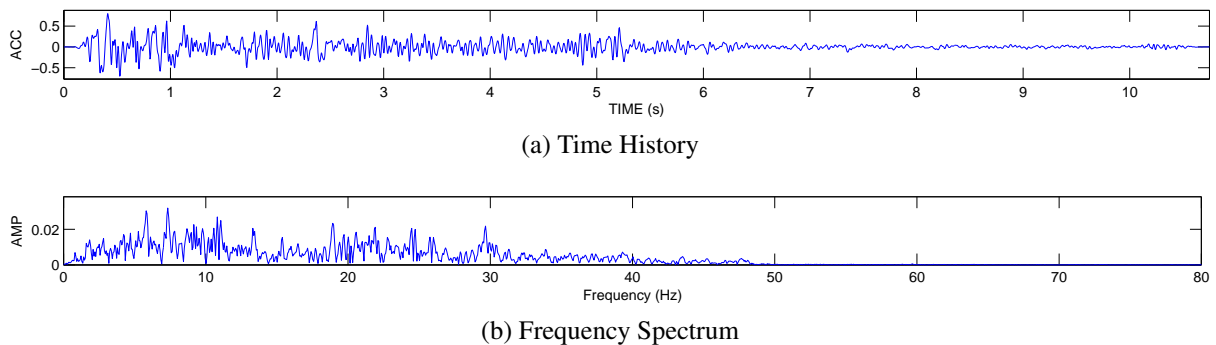


Figure 4.6: El Centro plots for (a) The scaled acceleration time history for the El Centro earthquake record (b) The frequency spectrum for the scaled El Centro earthquake record.

Table 4.2: Excitation level and its correspond peak acceleration

<i>Excitation level</i>	<i>Peak acceleration units of (G)</i>
1	0.093
2	0.266
3	0.399
4	0.532
5	0.665
6	0.798

4.1.6 Experimental Protocol

Although the shaker table was capable of multiple degrees of freedom, dynamic tests were only conducted for unidirectional and bidirectional. For the unidirectional test they were conducted in the horizontal X-direction. The three excitation records used were the El Centro earthquake record (EL), the Kobe earthquake record (KB) and the Shanghai artificial wave record (SH). The acceleration data were categorized into seven levels indicated in the range 1 to 7. Level 1 corresponds to a peak acceleration of 0.093 G, while level 6 corresponds to a peak acceleration of 0.798 G, this can be seen in table 4.2. The tests were carried out in the year 2000, where the first phase of testing took place in January and the second phase was from September to December.

The accelerometers mention in 4.1.4 were used to capture the data. The sampling frequency of the accelerometers was 250 Hz. The setup again is, one accelerometer was installed on the shaker table and was designated A0. Additional accelerometers were installed at every other floor; starting with accelerometer A1 installed at the base of the superstructure to A7 installed at the top of the superstructure. Figure 4.3 shows the building models with sensor locations and a photograph of the shaking table model.

4.1.7 Damage Observation After Shake Table Tests

During the experiments the Chen (2001) noticed the development of cracks in the fixed foundation model. No cracks develop until the 2nd level of excitation for all the wave records. During the 2nd level of excitations slight vertical cracks of approximately 0.05mm in width appeared on the end of the beams that are parallel to the direction of the excitation. These cracks appeared along 1st to 4th floors, the columns did not crack. After the 3rd levels of excitations more cracks develop these cracks were approximately 0.1mm in width and again were located on the beams parallel to the direction of the excitation, these cracks were located on the 1st through 5th floors. After the 4th level of excitations cracks of about 0.5mm in width developed along the beams on the 3rd and 4th floor. The columns on the 1st floor started to develop cracks and the columns on the 3rd floor started to develop localized crushed concrete. After the 4th level of excitation the cracks continued to develop. Finally, after the 6th level of excitation was applied, horizontal cracks in sizes from 0.2mm to 0.5mm appeared on the outside of the columns from the 1st to 3rd floor, crushed concrete was visible on the outside of the columns from 2nd to 3rd story columns, on the beams some of the cracks have almost run through the beams that are parallel to the direction of excitation this is for all beams from the 1st to the 8th floor the cracks vary in width from 0.1mm to 1mm, the largest cracks are found in between the 2nd and 5th floor. This last test left the fixed foundation test unstable.

For the pile and box foundation similar cracks developed on the superstructure but these cracks would develop at higher excitations than the cracks in the fixed foundation. It should also be noted that these cracks were generally smaller and less numerous but had the same general fracture pattern. For the pile foundation superstructure, cracks do not develop until the 5th level excitation at this time fine cracks developed on the bottom of the two columns (look into more detail currently just says northwest and northeast columns find out how they relate to direction of excitation), beams running parallel to the direction of excitation develop cracks

smaller than 0.02mm on floors 1 through 2. After all levels of excitation are run fine vertical cracks appear on floors 1 through 6, these cracks are much smaller than those that appeared on the fixed foundation. On the actual pile foundation it was noticed that cracking occurred on the piles themselves. After testing was complete for the box foundation fine cracks had developed on the column at the ground floor, these cracks were about 0.05mm in width, vertical cracks on the beams parallel to the direction of excitation had also developed on floors 1 through 5, these were smaller than 0.08mm in width.

After testing the pile foundation was dug up, cracking developed on all the piles as seen in Figure 4.7. Even between the piles and pile cap there was cracks, these were the widest cracks seen on the pile foundation. The cracking also varied with the depth, cracking on the piles was more severe near the pile cap and were small or nonexistent near the tip. The piles on the outside of the 3x3 foundation had more severe cracking than the center pile.

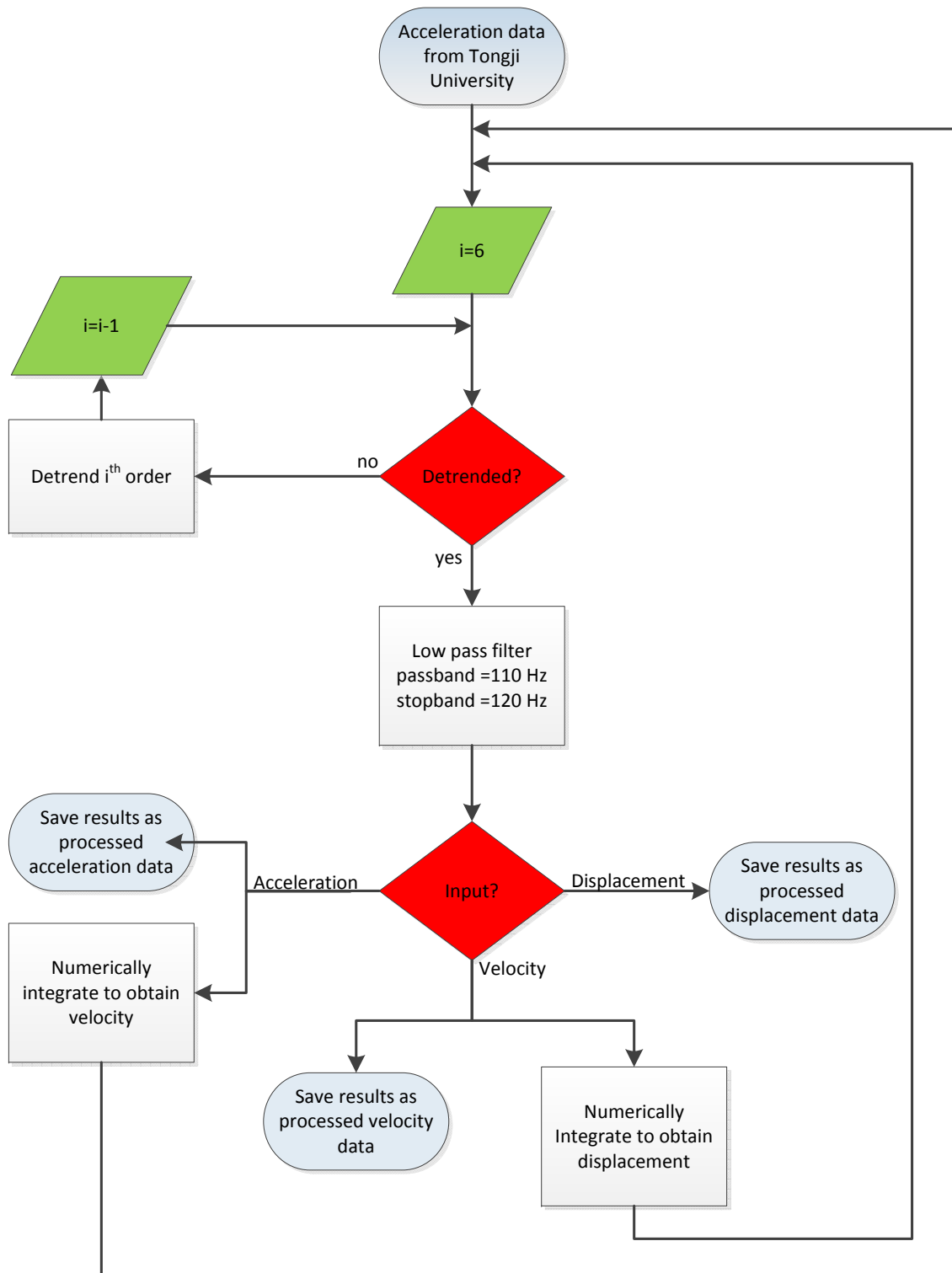


(a) Cracking on the pile foundation

Figure 4.7: Cracking of the pile foundation after testing. Source: (Chen, 2001).

4.2 Preprocessing Of Sensor Measurements

It was important that all data sets be processed the same way to ensure uniformity. A flowchart showing how the data was processed can be seen in Figure 4.8. To explain it, the recorded acceleration data was first detrended from the 6th order and filtered with a low-pass filter. The following properties for the filter were applied; the filter passband was set to 110 Hz and the stopband was set to 120 Hz, passband ripple was set to 1 dB and the stopband attenuation was 60 dB. After filtering, the acceleration data was then numerically integrated with respect to time using the MATLAB command “cumtrapz” to produce the velocity; velocity was then filtered with the same low pass filter and settings. Velocity was then numerically integrated in the same manner acceleration was to obtain the displacement data, which was then filter in the same way acceleration and velocity were. A sample of the acceleration and the calculated velocity, and displacement time history can be see in Figure 4.9 which is the acceleration, velocity and displacement of the shaker table due to the Shanghai excitation level 6 on the fixed foundation type.



(a) Acceleration Time History (G)

Figure 4.8: Flowchart representing how preprocessing was performed.

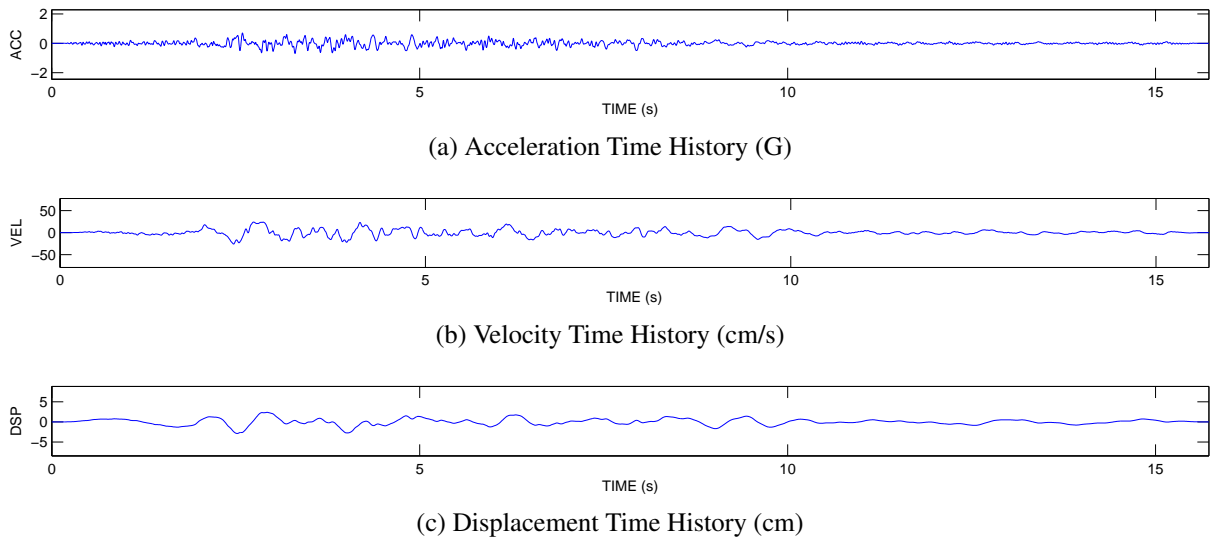


Figure 4.9: Response from channel A0, the shaker table, of the fixed foundation model due to Shanghai excitation level 6 (a) the absolute acceleration (\ddot{x}) time history (b) the absolute velocity (\dot{x}) time history (c) The absolute displacement (x) time history.

4.2.1 Restoring Force Estimation

After the measurements have been taken from the system, it is necessary to calculate the restoring force to use in the MDOF RFM. Since the information about the mass isn't readily available, instead the mass normalized restoring force must be calculated. Some assumptions had to be made about the structure. It was determined that based on the symmetry of the models, as can be seen in figure 4.3, that the masses associated with sensors A7 to A2 could be considered equal. Equation 2.29 will be used to calculate the restoring force. The system will be simplified as a chain like system with nonlinear elements interposed between 2 successive floors. Therefore, the following convention will be used; element G_7 will represent the system characteristics of floors 11 and 12; element G_6 will represent the system characteristics of floors 9 and 10; this pattern will follow for all the floors down to element G_2 representing the system characteristics of floors 1 and 2;

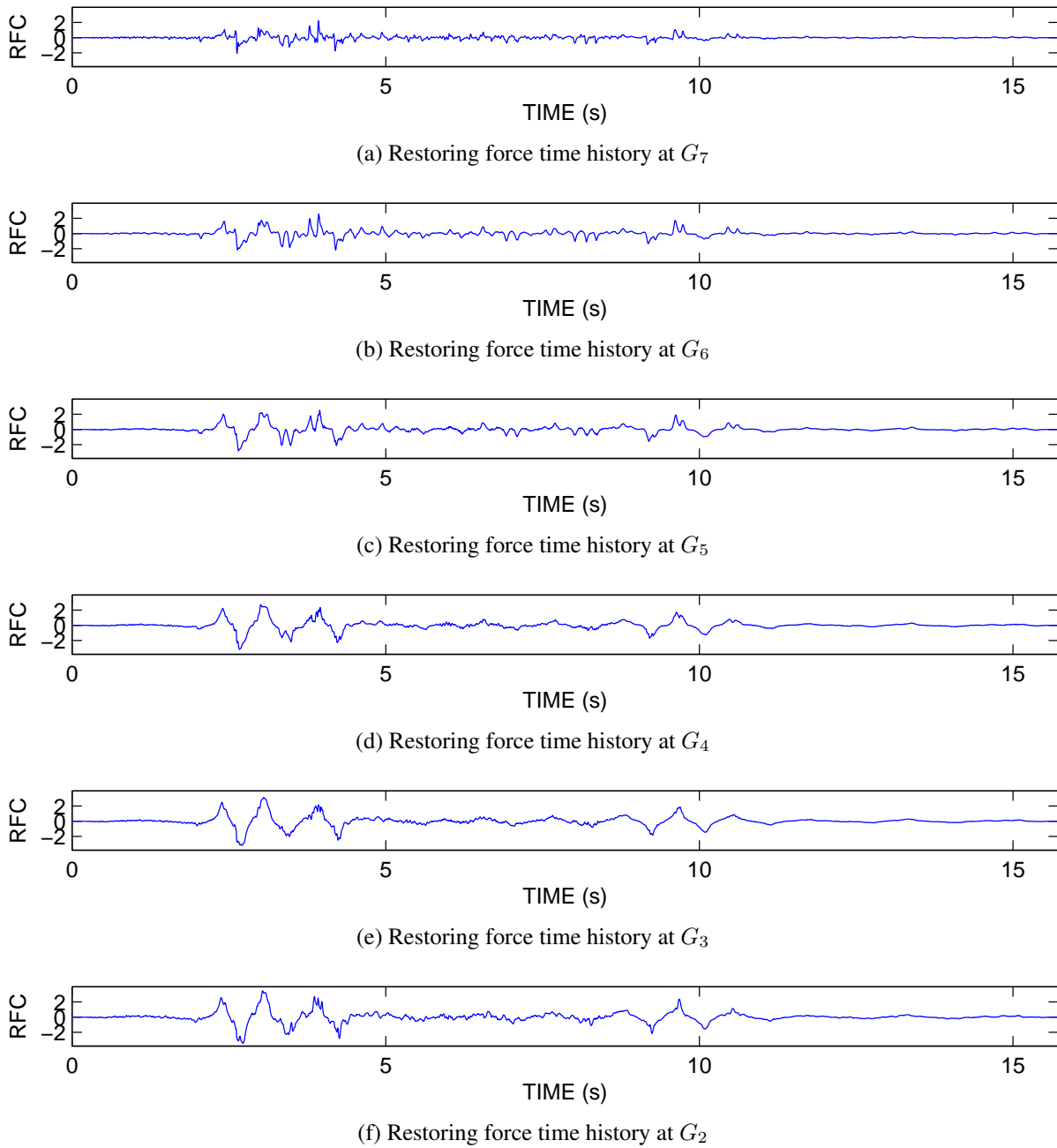


Figure 4.10: Time history of the measured restoring force for Shanghai excitation level 6 for the fixed foundation model at (a) G_7 , floors 11 and 12 (b) G_6 , floors 9 and 10 (c) G_5 , floors 7 and 8 (d) G_4 , floors 5 and 6 (e) G_3 , floors 3 and 4 (f) G_2 , floors 1 and 2.

Figure 4.10 demonstrates the change in amplitude of the restoring force for the different elements. At the lower elements, closer to the excitation, the restoring force is higher, because

it is more directly influenced by the shaking excitation. At the highest element G_7 the restoring force is lower because it is sufficiently far from the excitation. The restoring force helps to understand where damage will occur. If the dimensions and material properties are all identical for all elements, damage is more likely to occur where restoring force is larger. Therefore, damage is more likely to occur in elements G_2 , G_3 and G_4 compared to the elements located higher on the structure.

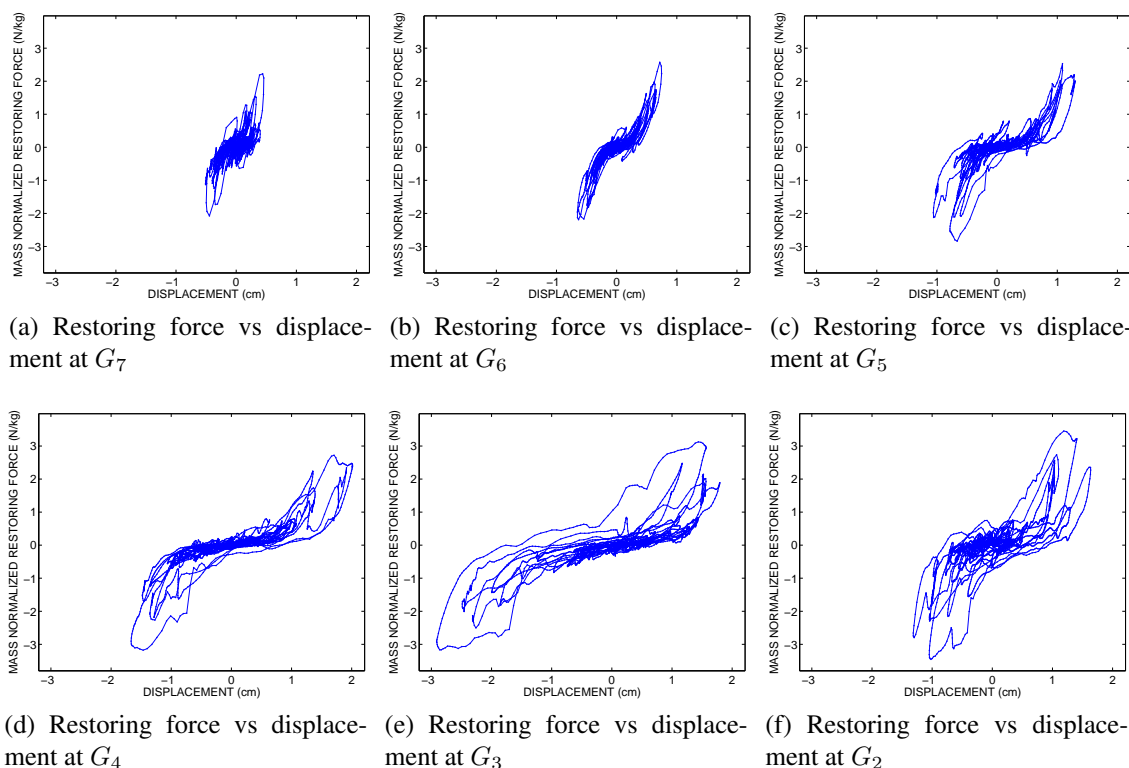


Figure 4.11: Phase Diagrams of restoring force vs displacement for Shanghai excitation level 6 for the fixed foundation model at (a) G_7 , floors 11 and 12 (b) G_6 , floors 9 and 10 (c) G_5 , floors 7 and 8 (d) G_4 , floors 5 and 6 (e) G_3 , floors 3 and 4 (f) G_2 , floors 1 and 2..

Figure 4.11 depicts the phase diagram for restoring force vs displacement. The displacement phase diagram provides insight into the system characteristics. This phase diagram for restoring force vs displacement most directly relates to the stiffness of the structure (Piersol and Paez, 2009). To start with, Figure 4.11 (a) is predominantly non-linear, exhibiting a very strong,

sharp, curved nonlinear function. This is because the excitation wasn't high enough at this level to create a wide nonlinear shape. Figure 4.11 (f) the restoring force exhibits a strong nonlinear property which also has a very wide shape and has smoother curves than those seen in 4.11 (a). Figure 4.11 (e) and Figure 4.11 (d) both display some of the widest nonlinear curves. Each of these phase diagrams for Figure 4.11 depicts a characteristic called hardening. A good description of hardening is provided by Piersol and Paez (2009), who describe it as a system characteristic in which small increases in displacement corresponds to rapid increases in the restoring force.

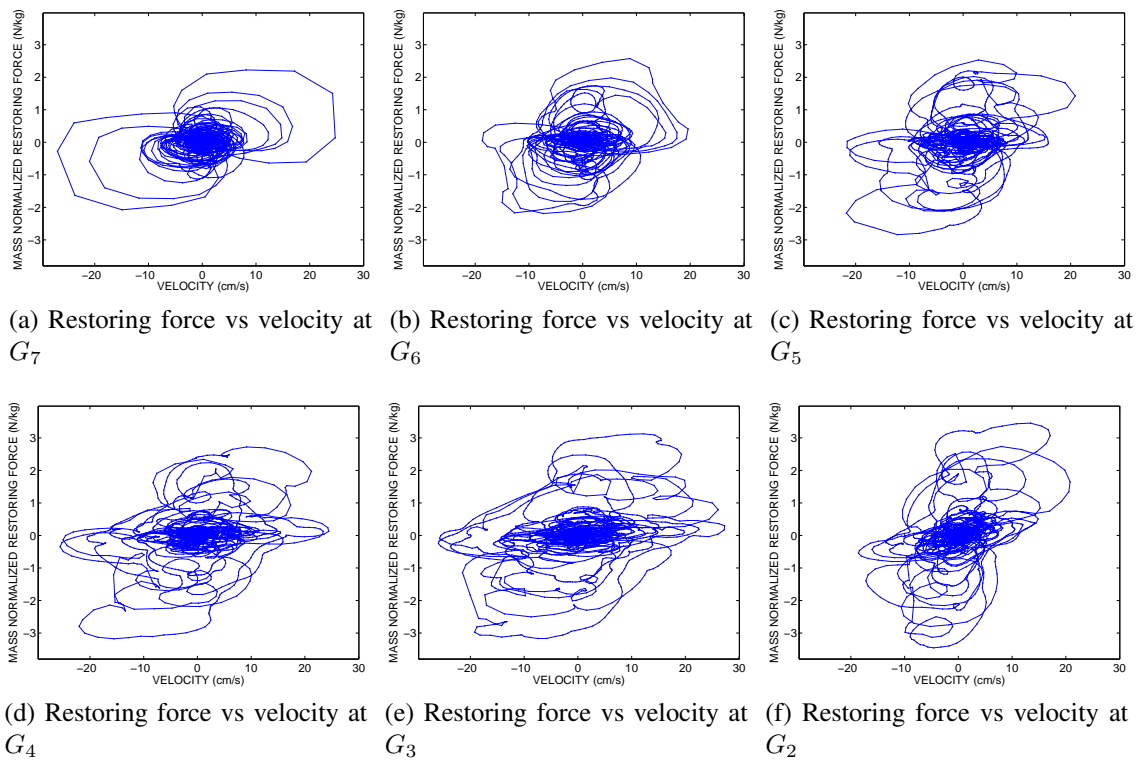


Figure 4.12: Phase Diagrams of restoring force vs velocity for Shanghai excitation level 6 for the fixed foundation model at (a) G_7 , floors 11 and 12 (b) G_6 , floors 9 and 10 (c) G_5 , floors 7 and 8 (d) G_4 , floors 5 and 6 (e) G_3 , floors 3 and 4 (f) G_2 , floors 1 and 2..

Similarly, to investigate the relationship between restoring force and damping coefficient, the phase diagram for restoring force vs velocity can be plotted (Piersol and Paez, 2009). This is

done in Figure 4.12. All of these restoring force velocity phase diagrams show some variation of a circular plot. This characteristics tends to indicate that the correlation between restoring force and velocity is weak, which would indicate that the contribution from the damping coefficients are small.

4.3 Multidegree Of Freedom Restoring Force Method Results

With the mass normalized restoring force calculated and the velocity and displacement for each degree of freedom calculated almost all of the data is ready to be input into the MRFM. As mentioned earlier in Subsection 2.2, the input data must be in the form of interstory relative displacements, and interstory relative velocities. Through the use of Equations 2.16 and 2.17 the interstory relative displacement and interstory relative velocity was calculated. Now with the interstory relative velocities, interstory relative displacement and mass normalized restoring force the restoring force method can be used. Please note that the since the mass normalized restoring force is being used that, the results will be in the form of the mass normalized coefficients.

With all the data ready to be used in the MRFM only one last thing remains which is to choose the model order in the RFM, it is important for the RFM to choose the right model order. If the model order is too low, under-fitting occurs but using a high model order creates a risk of over-fitting. Figure 4.13 helped to decided what model order to use. From this figure, it was determined to use a 4th order model.

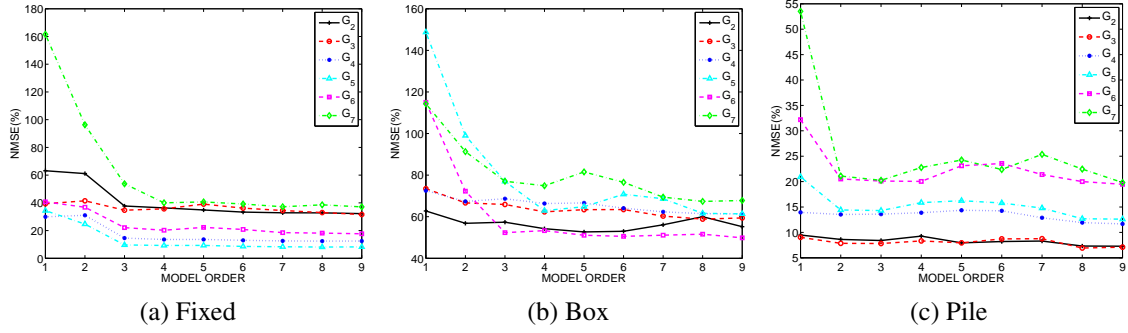


Figure 4.13: Model order vs the NMSE for the (a) fixed foundation (b) box foundation (c) pile foundation.

4.3.1 Error In Estimation

To ensure the validity of the results, this section will describe the measured error from the difference between the calculated measured restoring force and the approximated restoring force. A common measure of error between the measured mass normalized restoring force, $G^m(z, \dot{z})$, and the approximated mass normalized restoring force, $\hat{G}_n^m(\bar{z}, \dot{\bar{z}})$, is the Normalized Mean Square Error (NMSE), which is a measurement between the difference of the measured and approximated values, in this case measured and approximated restoring force. NMSE can be calculated by Equation 4.1 (Worden, 1990)

$$NMSE(\hat{x})(\%) = \frac{100}{N\sigma_x^2} \sum_{i=1}^N (x_i - \hat{x}_i)^2 \quad (4.1)$$

where x_i is the measured data, in this case it will be the measured restoring force, \hat{x}_i is the estimated data in this case the approximated mass normalized restoring force, N is the number of data points which must be the same for both approximated and measured, restoring forces, and σ_x^2 is the variance of the measured data. The normalized mean square can be used to evaluate the accuracy of identification results (Yun et al., 2008). While the identification results are actually the Chebyshev coefficients not the approximated restoring force, the Chebyshev coefficients are

used in the creation of the approximated restoring force, in this sense the NMSE indicates how well the coefficients can accurately approximate the restoring force. A large NMSE indicates that there is a large difference between the measured and approximated restoring forces, which will indicate the identified Chebyshev coefficients are poor indicators of the measured restoring force. While a small NMSE indicates that there is a small difference between the measured and approximated restoring force, this indicates that the identified Chebyshev coefficients can accurately be used to recreate the measured restoring force. So the lower NMSE the better the identification results are. The NMSE can be used to calculate the error between the two values. These NMSE values are found in Tables 4.3, 4.4, and 4.5.

Table 4.3: NMSE of the reconstructed restoring force for all levels of the Shanghai excitation for the box, pile and fixed foundation models

<i>Fixed Foundation</i>							
<i>Mass Normalized Restoring Force</i>	Shanghai Excitation Level						<i>Mean For Node</i>
	1	2	3	4	5	6	
\hat{G}_2^m	85.69	32.07	36.38	27.05	15.54	34.62	38.56
\hat{G}_3^m	59.18	11.95	35.67	29.3	19.41	20.21	29.29
\hat{G}_4^m	54.54	14.16	13.55	25.93	9.54	11.08	21.47
\hat{G}_5^m	70.12	35.67	9.29	16.76	7.38	32.26	28.58
\hat{G}_6^m	68.66	41.72	20.24	34.97	10.17	11.8	31.26
\hat{G}_7^m	91.09	66.93	40.01	30.55	34.66	51.39	52.44
<i>Mean for Level</i>	71.55	33.75	25.86	27.43	16.12	26.89	33.60
<i>Box Foundation</i>							
<i>Mass Normalized Restoring Force</i>	Shanghai Excitation Level						<i>Mean For Node</i>
	1	2	3	4	5	6	
\hat{G}_2^m	19.81	32.33	54.26	60.44	74.40	72.03	52.21
\hat{G}_3^m	17.99	42.50	62.35	81.28	72.01	81.26	59.57
\hat{G}_4^m	22.83	35.79	66.34	65.71	75.39	84.29	58.39
\hat{G}_5^m	9.79	42.88	62.94	74.55	98.77	83.80	62.12
\hat{G}_6^m	13.73	30.69	53.29	93.44	107.67	104.99	67.30
\hat{G}_7^m	25.26	64.40	74.89	81.75	82.00	95.08	70.56
<i>Mean for Level</i>	18.24	41.43	62.35	76.2	85.04	86.91	61.69
<i>Pile Foundation</i>							
<i>Mass Normalized Restoring Force</i>	Shanghai Excitation Level						<i>Mean For Node</i>
	1	2	3	4	5	6	
\hat{G}_2^m	35.22	8.99	9.26	4.52	5.89	12.34	12.70
\hat{G}_3^m	42.62	9.13	8.31	5.48	11.29	16.49	15.55
\hat{G}_4^m	41.57	29.74	13.87	5.20	9.10	12.78	18.71
\hat{G}_5^m	25.55	20.19	15.86	10.5	19.02	30.99	20.35
\hat{G}_6^m	46.54	24.89	20.04	12.14	34.88	32.8	28.55
\hat{G}_7^m	58.71	105.54	22.77	21.94	41.94	62.94	52.31
<i>Mean for Level</i>	41.7	33.08	15.02	9.96	20.35	28.06	24.7

Table 4.4: NMSE of the reconstructed restoring force for all levels of the Kobe excitation for the box, pile and fixed foundation models

<i>Fixed Foundation</i>							
<i>Mass Normalized Restoring Force</i>	Kobe Excitation Level						<i>Mean For Node</i>
	1	2	3	4	5	6	
\hat{G}_2^m	135.71	158.01	105.65	36.56	46.53	51.32	88.96
\hat{G}_3^m	91.34	8.8	33.04	21.32	41.32	70.81	44.44
\hat{G}_4^m	189.65	15.67	25.26	26.93	39.67	50.41	57.93
\hat{G}_5^m	220.27	40.32	48.69	15.23	22.48	22.7	61.62
\hat{G}_6^m	144.86	35.41	49.5	60.32	37.13	9.43	56.11
\hat{G}_7^m	120.54	196.59	84.63	174.7	66.6	61.91	117.5
<i>Mean for Level</i>	150.4	75.8	57.8	55.84	42.29	44.43	71.09
<i>Box Foundation</i>							
<i>Mass Normalized Restoring Force</i>	Kobe Excitation Level						<i>Mean For Node</i>
	1	2	3	4	5	6	
\hat{G}_2^m	59.69	62.19	91.78	102.62	93.31	77.64	81.21
\hat{G}_3^m	67.38	59.32	78.01	79.59	116.86	71.29	78.74
\hat{G}_4^m	60.25	87.42	96.48	88.10	63.33	97.29	82.15
\hat{G}_5^m	94.00	80.81	74.59	83.23	68.73	83.20	80.76
\hat{G}_6^m	71.10	72.91	73.64	100.71	99.88	71.34	81.60
\hat{G}_7^m	97.93	86.59	90.20	74.72	80.37	112.82	90.44
<i>Mean for Level</i>	75.06	74.87	84.12	88.16	87.08	85.6	82.48
<i>Pile Foundation</i>							
<i>Mass Normalized Restoring Force</i>	Kobe Excitation Level						<i>Mean For Node</i>
	1	2	3	4	5	6	
\hat{G}_2^m	162.03	58.95	64.51	47.72	15.31	32.79	63.55
\hat{G}_3^m	159.35	27.26	6.26	12.33	12.01	14.13	38.56
\hat{G}_4^m	48.13	12.57	40.95	33.93	7.96	8.97	25.42
\hat{G}_5^m	145.78	73.29	63.46	41.85	29.85	18.12	62.06
\hat{G}_6^m	92.83	119.54	111.18	32.7	31.1	36.52	70.65
\hat{G}_7^m	109.93	162.84	72.45	44.41	45.32	64.29	83.21
<i>Mean for Level</i>	119.68	75.74	59.8	35.49	23.59	29.14	57.24

Table 4.5: NMSE of the reconstructed restoring force for all levels of the El Centro excitation for the box, pile and fixed foundation models

<i>Fixed Foundation</i>							
<i>Mass Normalized Restoring Force</i>	El Centro Excitation Level						<i>Mean For Node</i>
	1	2	3	4	5	6	
\hat{G}_2^m	90.11	46.45	13.4	5.19	19.58	22.88	32.94
\hat{G}_3^m	93.69	16.35	1.75	3.99	13.77	18.73	24.71
\hat{G}_4^m	55.08	27.28	3.43	5.78	40.26	50.84	30.45
\hat{G}_5^m	64.6	54.71	18.29	12.93	26.89	43.7	36.85
\hat{G}_6^m	68.73	71.52	16.79	26.62	18.74	19.99	37.07
\hat{G}_7^m	85.55	58.33	35.42	41.8	59.01	51.15	55.21
<i>Mean for Level</i>	76.29	45.77	14.85	16.05	29.71	34.55	36.21
<i>Box Foundation</i>							
<i>Mass Normalized Restoring Force</i>	El Centro Excitation Level						<i>Mean For Node</i>
	1	2	3	4	5	6	
\hat{G}_2^m	19.85	49.47	40.33	29.31	45.79	42.29	37.84
\hat{G}_3^m	16.13	29.03	49.85	38.52	39.99	60.95	39.08
\hat{G}_4^m	15.96	51.66	53.63	40.2	44.41	59.13	44.17
\hat{G}_5^m	53.32	46.87	64.75	58.78	40.49	58.98	53.87
\hat{G}_6^m	19	26.14	60.77	37.22	40.98	54.97	39.85
\hat{G}_7^m	98.99	52.95	57.11	56.3	59.95	73.55	66.48
<i>Mean for Level</i>	37.21	42.69	54.41	43.39	45.27	58.31	46.88
<i>Pile Foundation</i>							
<i>Mass Normalized Restoring Force</i>	El Centro Excitation Level						<i>Mean For Node</i>
	1	2	3	4	5	6	
\hat{G}_2^m	65.00	40.50	8.14	9.23	28.67	32.43	30.66
\hat{G}_3^m	19.30	37.20	4.86	6.00	23.93	31.81	20.52
\hat{G}_4^m	64.61	32.69	15.8	13.63	23.54	30.54	30.14
\hat{G}_5^m	56.94	54.44	24.61	22.27	42.86	82.64	47.29
\hat{G}_6^m	68.58	76.75	33.11	23.73	38.35	68.62	51.52
\hat{G}_7^m	57.44	115.36	49.11	37.10	33.71	51.03	57.29
<i>Mean for Level</i>	57.44	115.36	49.11	37.10	33.71	51.03	57.29

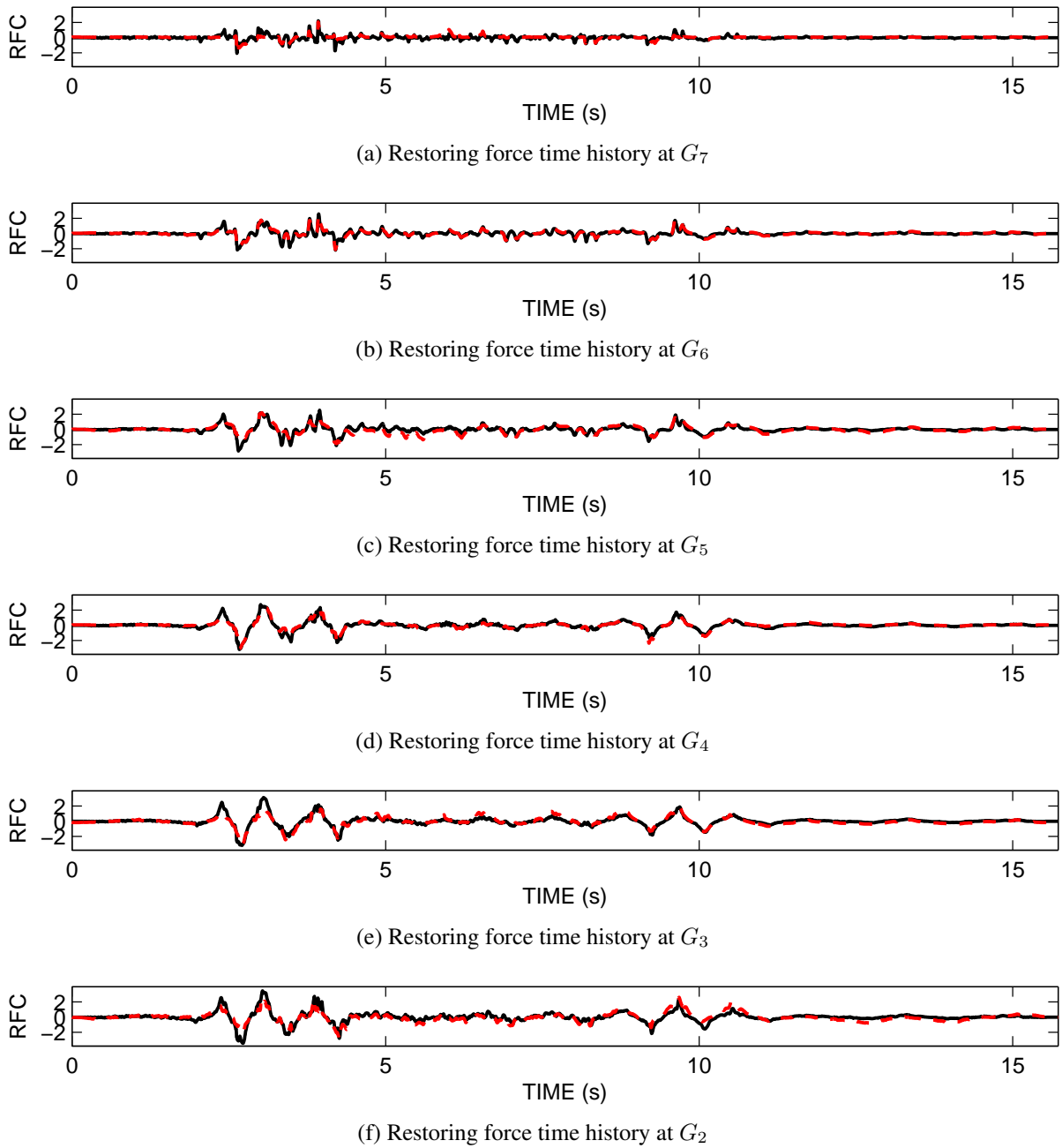


Figure 4.14: Time history of the measured restoring force, in blue, with the approximated restoring force, in red, overlapped for Shanghai excitation level 6 for the fixed foundation model at (a) G_7 , floors 11 and 12 (b) G_6 , floors 9 and 10 (c) G_5 , floors 7 and 8 (d) G_4 , floors 5 and 6 (e) G_3 , floors 3 and 4 (f) G_2 , floors 1 and 2.

It is important to make sure that the estimated mass normalized restoring force, $\hat{G}_n^m(\bar{z}, \dot{\bar{z}})$,

is close to the measured mass normalized restoring force, $G_n^m(z, \dot{z})$, through means of visual comparison, to ensure similar characteristics are capture in the estimated restoring force. This is done so in Figure 4.14. Overall, the two restoring forces match relatively closely. Most of the major peaks overlay; however at some of the smaller peaks a difference is visible between the two restoring forces. Because the way the NMSE works the smaller peaks have a higher weight then the larger peaks so even if the larger peaks are closer the smaller peaks will give a higher NMSE.

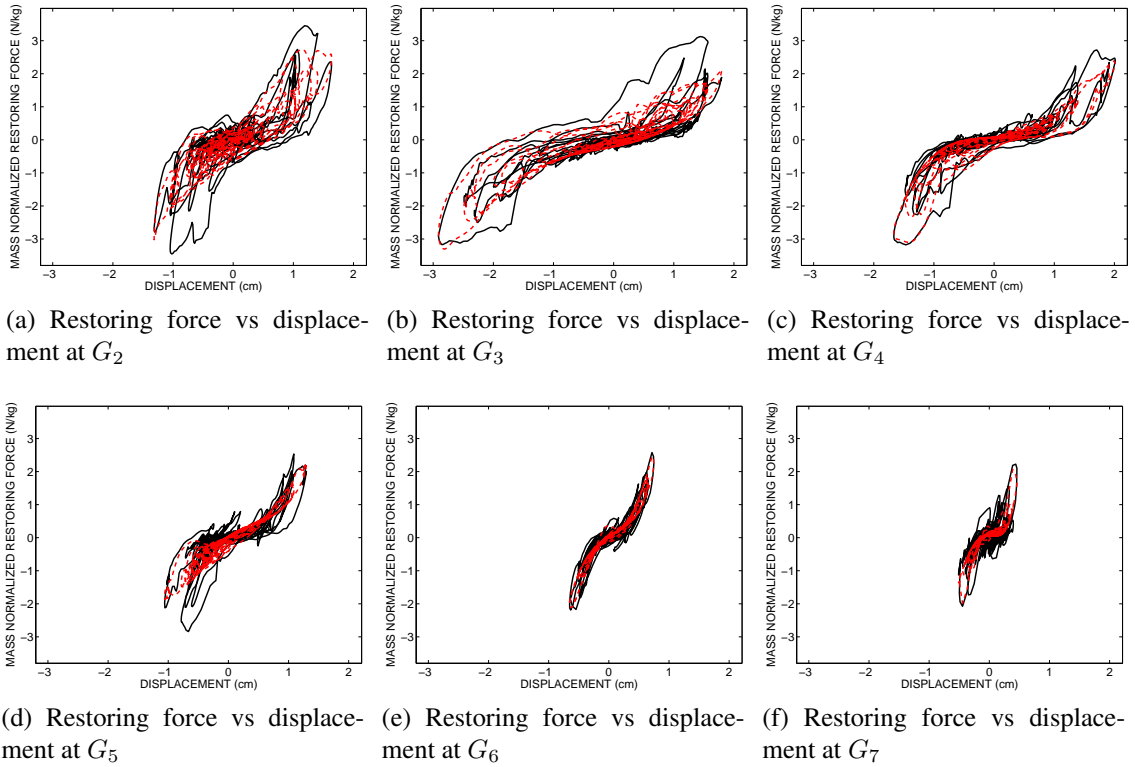


Figure 4.15: Phase Diagrams of restoring force vs displacement for Shanghai excitation level 6 for the fixed foundation model at (a) G_7 , floors 11 and 12 (b) G_6 , floors 9 and 10 (c) G_5 , floors 7 and 8 (d) G_4 , floors 5 and 6 (e) G_3 , floors 3 and 4 (f) G_2 , floors 1 and 2..

It is also important to make sure that the estimated restoring force, $\hat{G}_n^m(\bar{z}, \bar{\dot{z}})$, creates a phase diagram similar to the measured restoring force, $G_n^m(\bar{z}, \bar{\dot{z}})$. This will ensure that the identified results carry over the similar stiffness system characteristics as the measured restoring force.

By Figure 4.14 it is visible that for the phase diagram, for displacement vs. restoring force, a similar third order hardening is achieved in both measured and approximated restoring force. The overlap shows that most of the characteristics are able to be accurately replicated.

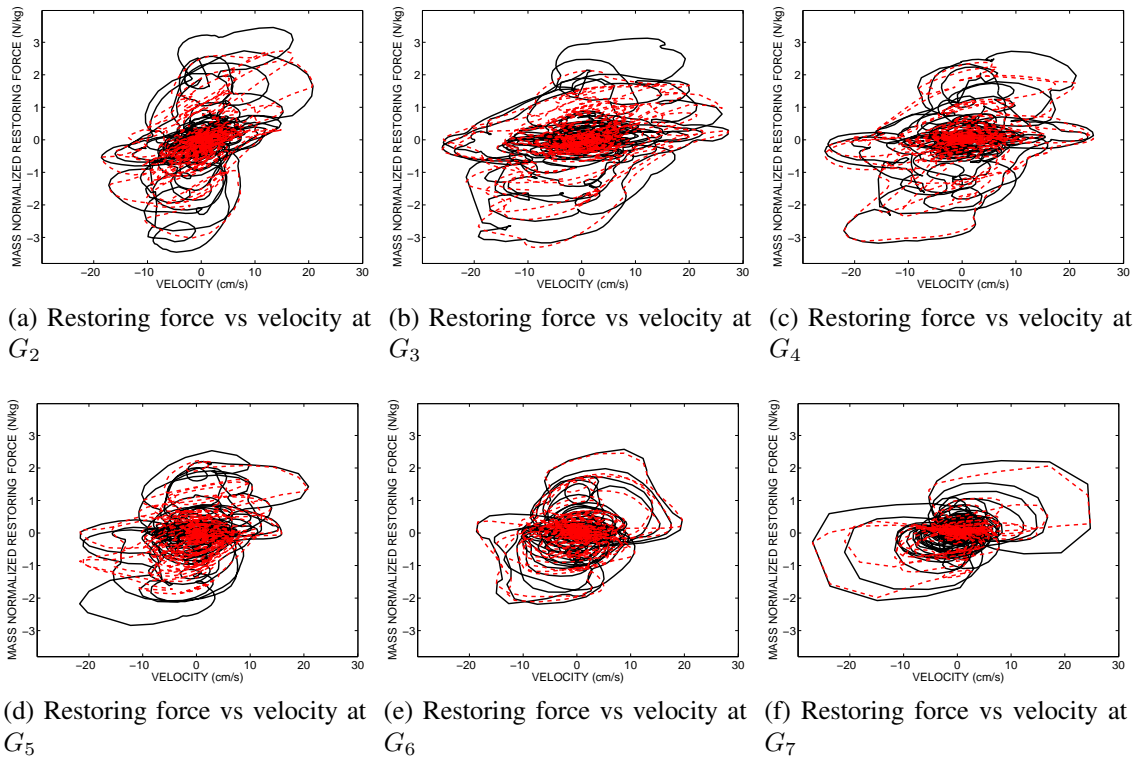


Figure 4.16: Phase Diagrams of restoring force vs velocity for Shanghai excitation level 6 for the fixed foundation model at (a) G_7 , floors 11 and 12 (b) G_6 , floors 9 and 10 (c) G_5 , floors 7 and 8 (d) G_4 , floors 5 and 6 (e) G_3 , floors 3 and 4 (f) G_2 , floors 1 and 2..

Similarly, this visual comparison also applies to the velocity and restoring force, phase diagram to ensure that the identified results carry over the same properties as the measured restoring force. By Figure 4.16 it is visible that for the phase diagram, for velocity vs. restoring force, a similar circular pattern showing, that restoring force and velocity are not in phase, is achieved in both measured and approximated restoring force. The overlap shows that most of the characteristics are able to be accurately replicated.

4.3.2 *MRFM For Fixed Foundation*

Several data sets were analyzed with the MRFM. These data sets corresponded to the unidirectional excitations applied to all three foundation types, with the El Centro earthquake record (EL), the Kobe earthquake record (KB) and the Shanghai artificial wave record (SH) for excitation intensity levels one through six. In total 54 data sets were processed, and each data set was analyzed for the range from sensor A7 to A2. Each data set analyzed produced 6 tables of Chebyshev coefficients. In total there are 324 tables of Chebyshev coefficients. One table for each excitation type, excitation level, foundation type and elements G_2 through G_7 .

Since the results are so numerous, only select results from the MRFM will be show. These results will primarily be from the Shanghai excitation level 6 and will be for each foundation type. These results are chosen because of the high level excitation and since the Shanghai artificial wave is a broadband excitation, able to excite many frequencies.

First, analysis will be run on the fixed foundation. The fixed foundation is chosen since it is the simplest case to analysis since, there was no foundation, there was no SFSI. The results from the fixed foundation will establish the analytical approach for the remaining foundations.

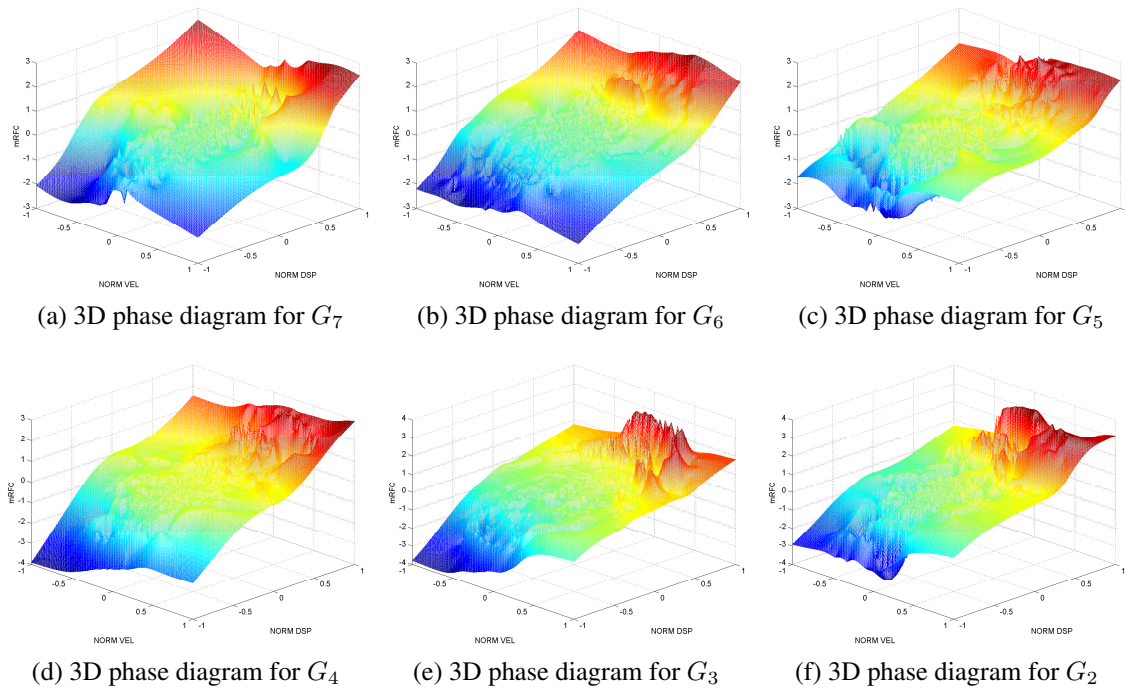


Figure 4.17: 3D phase Diagrams of the measured restoring force vs displacement vs velocity for Shanghai excitation level 6 for the fixed foundation model at (a) G_7 , floors 11 and 12 (b) G_6 , floors 9 and 10 (c) G_5 , floors 7 and 8 (d) G_4 , floors 5 and 6 (e) G_3 , floors 3 and 4 (f) G_2 , floors 1 and 2..

Since the MRFM is a phase domain system identification technique it is important to see the phase surface. Figure 4.17 shows the phase surface that is to be fitted by the restoring force method. This is the surface created by the RBFs interpolation, that the RFM will fit. The slopes of the figure give insight into the damping and stiffness characteristics of the surface. It should be noted that the RBFs also capture any noise in the data and fit that to the surface too. This can explain the numerous small peaks and dips. Figure 4.17 (c) is a good example of this. The strong slope on the displacement axis indicates the stiffness characteristics of the structure while the relatively small slope of the velocity axis shows that damping will be a weak characteristic. These 3d plots generally reinforce what has already been seen in Figure 4.12 and 4.11.

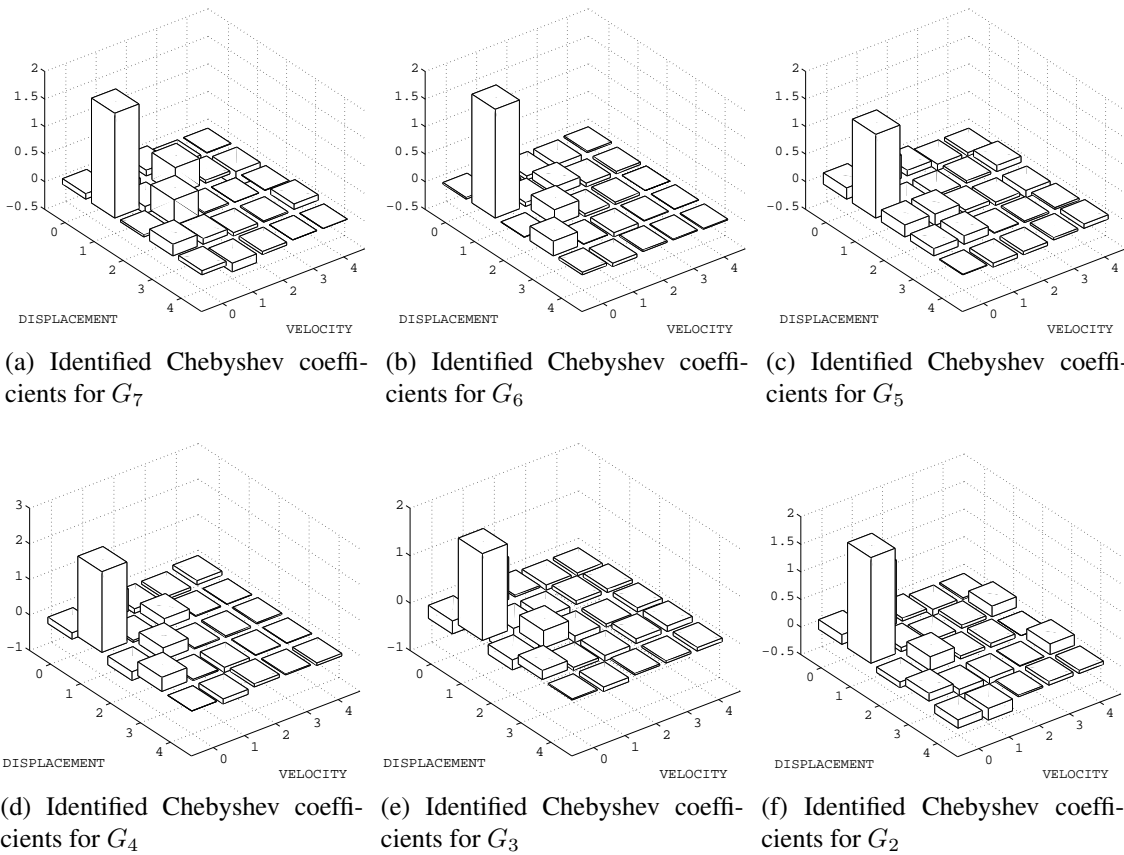


Figure 4.18: Identified Chebyshev coefficients for the Shanghai excitation level 6 for the fixed foundation model at (a) G_7 , floors 11 and 12 (b) G_6 , floors 9 and 10 (c) G_5 , floors 7 and 8 (d) G_4 , floors 5 and 6 (e) G_3 , floors 3 and 4 (f) G_2 , floors 1 and 2.

By performing the MRFM identification on the Shanghai excitation level 6 for the fixed foundation model results in the Chebyshev coefficients seen in Figure 4.18. As mentioned before, since this is a nonparametric method the Chebyshev coefficients don't reveal much about the system. However it can indicate contribution by stiffness-like coefficients and damping-like coefficients. The columns in Figure 4.18 represent restoring force dependencies on velocity, displacement or a couple effect of velocity and displacement. The numerical values along the left hand side of the 3d bar chart are for displacement terms and the numerical values on the right hand side are for velocity terms, the horizontal numerical numbers are for the actual value

of the Chebyshev coefficient. So to understand the stiffness-like contribution, look at any of the values C_{i0} , where $i > 0$. Any value here would represent a contribution by only a stiffness-like term. Similarly C_{0j} , where $j > 0$, would represent a value by only damping-like term. As shown before in Figure 4.11 and Figure 4.12, it was primarily expected that the results would largely be displacement dependent indicating stiffness-like coefficients contribute the most. This is confirmed in the results obtained in Figure 4.18. There are some contributions by coupled terms, seen in Figure 4.18 (a)-(f), most notably in 4.18 (a), but these are much smaller than the displacement dependent terms. It should be noted that the Chebyshev coefficients do not give a very good indication of the nonlinearity of the system, for this it is best to look at the power series coefficients.

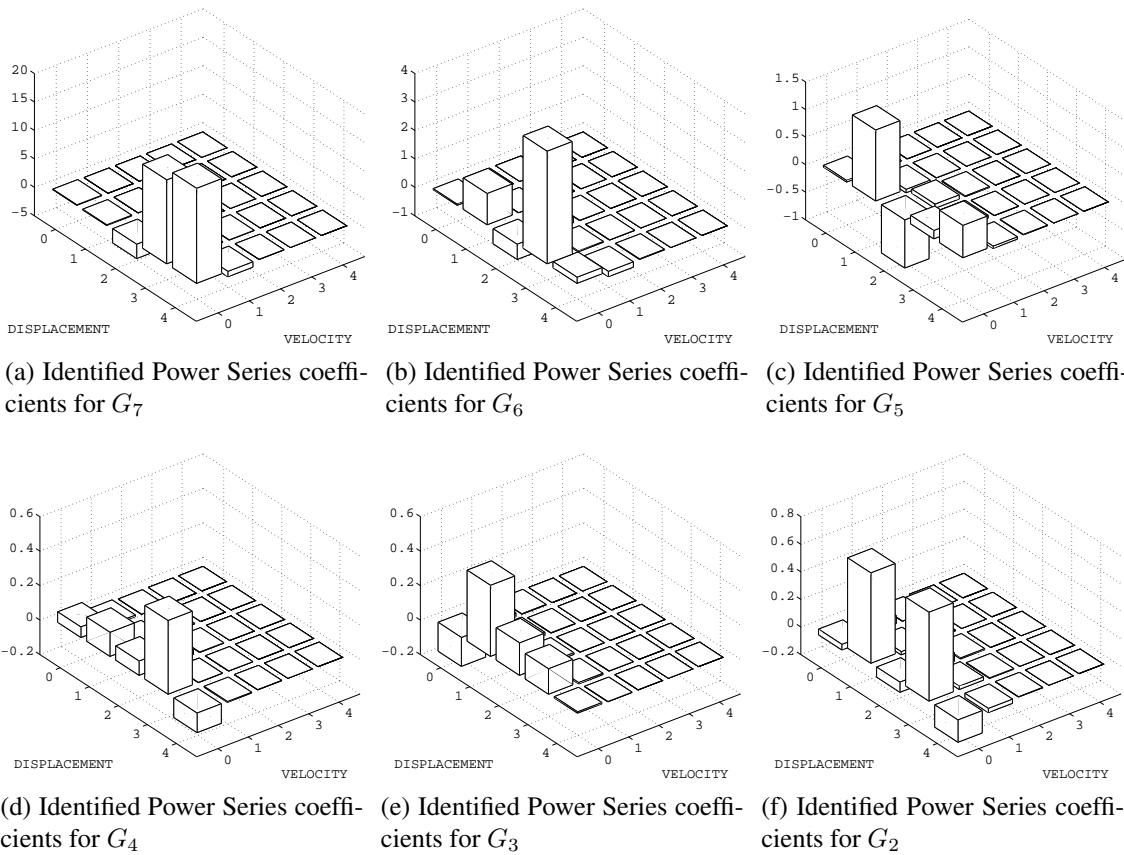


Figure 4.19: Identified power series coefficients for the Shanghai excitation level 6 for the fixed foundation model at (a) G_7 , floors 11 and 12 (b) G_6 , floors 9 and 10 (c) G_5 , floors 7 and 8 (d) G_4 , floors 5 and 6 (e) G_3 , floors 3 and 4 (f) G_2 , floors 1 and 2.

The identified Chebyshev coefficients in Figure 4.18 can be converted to the power series coefficients seen in Figure 4.19. The columns in Figure 4.19 represent restoring force damping-like coefficients, stiffness-like coefficients or a couple effect of both. The numerical values along the left hand side of the 3d bar chart are for stiffness-like terms and the numerical values on the right hand side are for damping-like terms. The horizontal numerical numbers are for the values of the power series coefficient. To summarize this the stiffness-like terms can be found by looking at any of the values A_{i0} , where $i > 0$. Similarly A_{0j} , where $j > 0$, would represent a damping-like term. These power series coefficients will give parametric information

about the system. By taking a look at Figure 4.19, it can be seen that for most of the restoring force elements G , the stiffness-like coefficients are nonlinear dominant, mostly 3rd order, and with some linear stiffness-like coefficients. Figure 4.19 (f) and (e) show the largest contribution of linear elements. This was expected from the results seen in Figure 4.11. On observation of Figure 4.19 (d) which represents G_5 , it is observed that this case does not follow the same pattern as the other restoring force elements. Here the system is controlled by a dominant linear element. There should be very little reason for this element alone to break the pattern. This result from G_5 will be discussed further.

4.3.3 Term Wise Identification

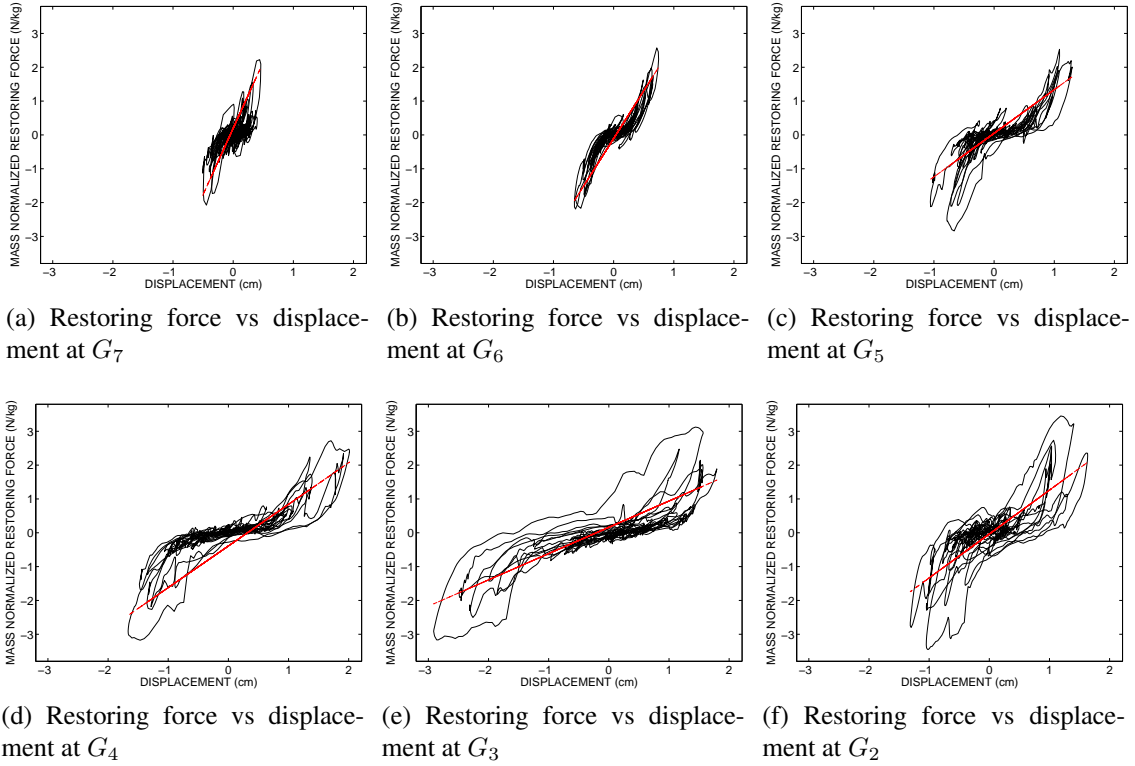


Figure 4.20: Term wise phase Diagrams of restoring force vs displacement with the first order displacement dependent Chebyshev coefficient C_{10}^m only used to reconstruct the restoring force plotted for Shanghai excitation level 6 for the fixed foundation model at (a) G_2 (b) G_3 (c) G_4 (d) G_5 (e) G_6 (f) G_7 .

From Figure 4.18 it was seen that the most dominant term was C_{10}^m . This can further be investigated by plotting the term wise coefficients. These help to indicate the contribution from individual terms (Yun et al., 2008). Figure 4.21 shows strong contributions from the C_{10}^m . This can be seen by looking at the slope of each individual figure, a steeper slope indicates a high contribution.

Figure 4.21 plots the C_{30}^m and shows the nonlinear characteristic of the various degrees of freedom. It can be seen that Figure 4.21 (c)-(f) depicts strong nonlinear contributions compared to Figure 4.21 (a)-(b).

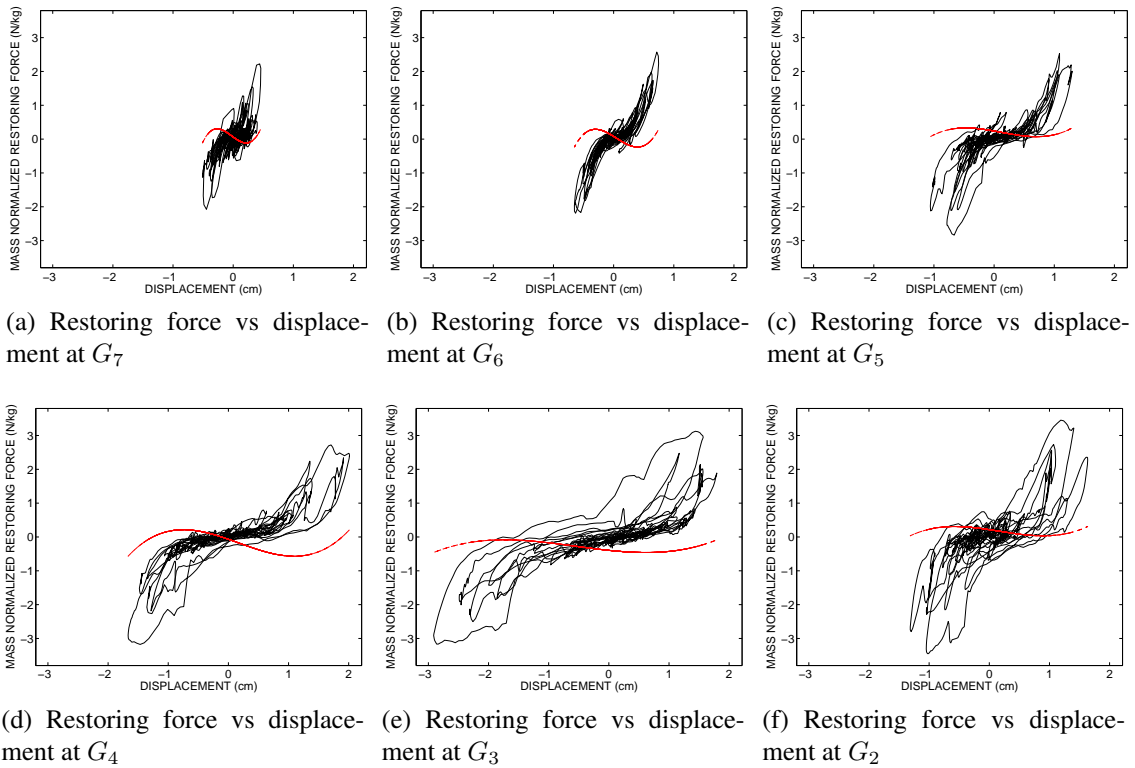


Figure 4.21: Term wise phase Diagrams of restoring force vs displacement with the third order displacement dependent Chebyshev coefficient C_{30}^m only used to reconstruct the restoring force plotted for Shanghai excitation level 6 for the fixed foundation model at (a) G_2 (b) G_3 (c) G_4 (d) G_5 (e) G_6 (f) G_7 .

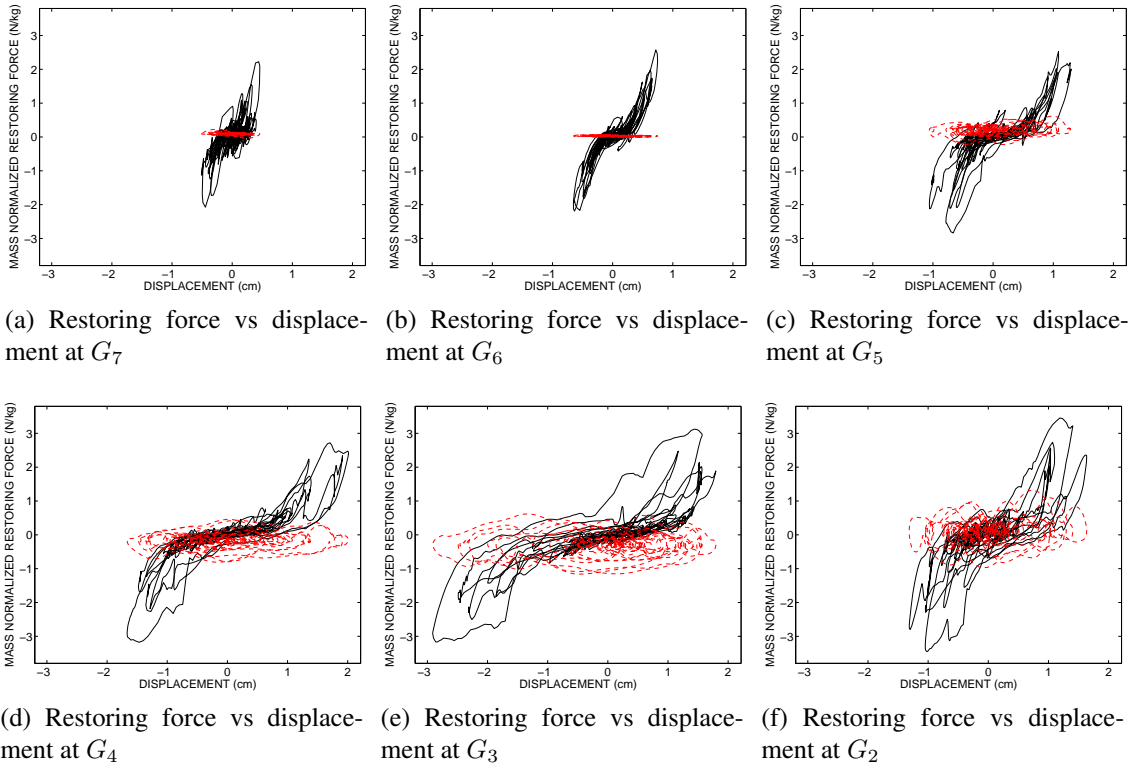


Figure 4.22: Term wise phase Diagrams of restoring force vs displacement with the first order velocity-dependent Chebyshev coefficient C_{01}^m only used to reconstruct the restoring force plotted for Shanghai excitation level 6 for the fixed foundation model at (a) G_2 (b) G_3 (c) G_4 (d) G_5 (e) G_6 (f) G_7 .

Figure 4.22 shows the hysteresis in the displacement phase diagrams are contributed largely by the C_{01}^m term and are important for properly modeling the nonlinear elements. The hysteresis can be seen decreasing from 4.22 (a) to 4.22 (e).

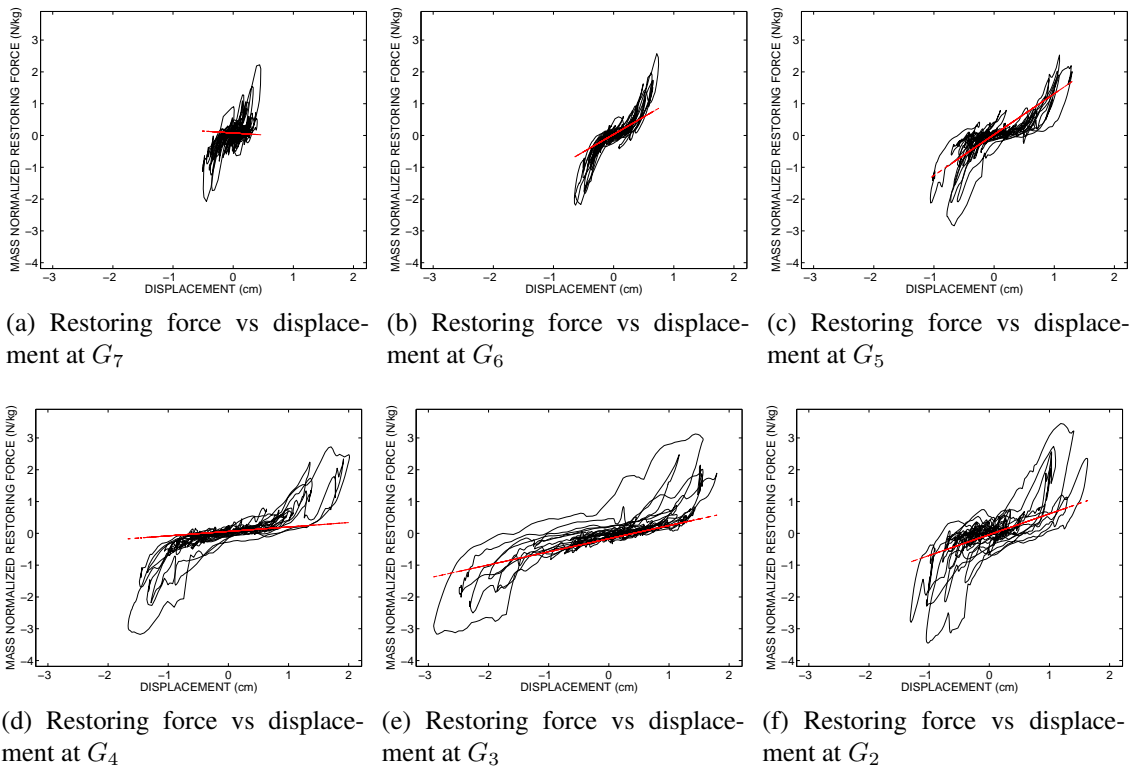


Figure 4.23: Term wise phase Diagrams of restoring force vs displacement with the first order stiffness-like coefficient a_{10}^m only used to reconstruct the restoring force plotted for Shanghai excitation level 6 for the fixed foundation model at (a) G_2 (b) G_3 (c) G_4 (d) G_5 (e) G_6 (f) G_7 .

Plotting the power series termwise coefficients helps to show contribution of the terms. Figure 4.23 shows the contribution of the linear a_{10}^m term. It is clearly visible in Figure 4.23 (f) that there is very little contribution and in Figure 4.23 (d) the linear term is very high and this is peculiar. It is higher than any other term; more than likely this is error.

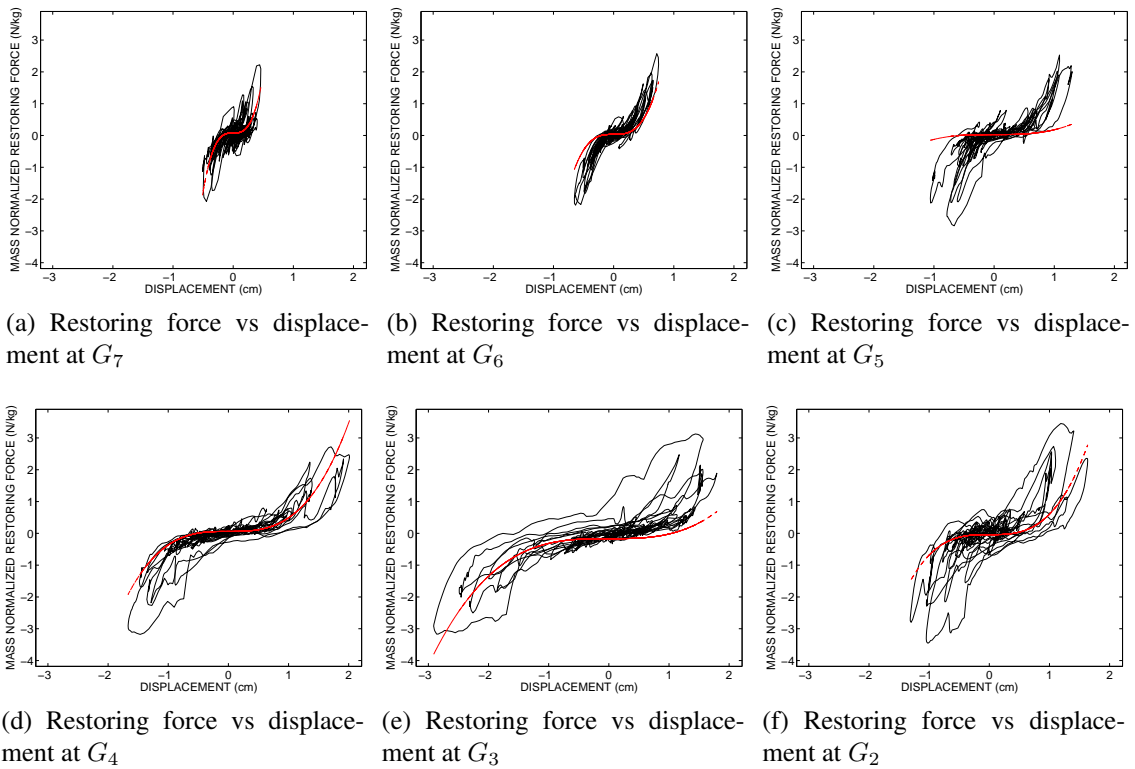


Figure 4.24: Term wise phase Diagrams of restoring force vs displacement with the third order stiffness-like coefficient a_{30}^m only used to reconstruct the restoring force plotted for Shanghai excitation level 6 for the fixed foundation model at (a) G_2 (b) G_3 (c) G_4 (d) G_5 (e) G_6 (f) G_7 .

Figure 4.24 shows the contribution of the nonlinear a_{30}^m term. It is clearly visible in Figure 4.23 (d) that there is very little contribution even though the phase diagram shows a very cubic function again this is some type of error. The rest of the plots in Figure 4.23 show very strong cubic contributions.

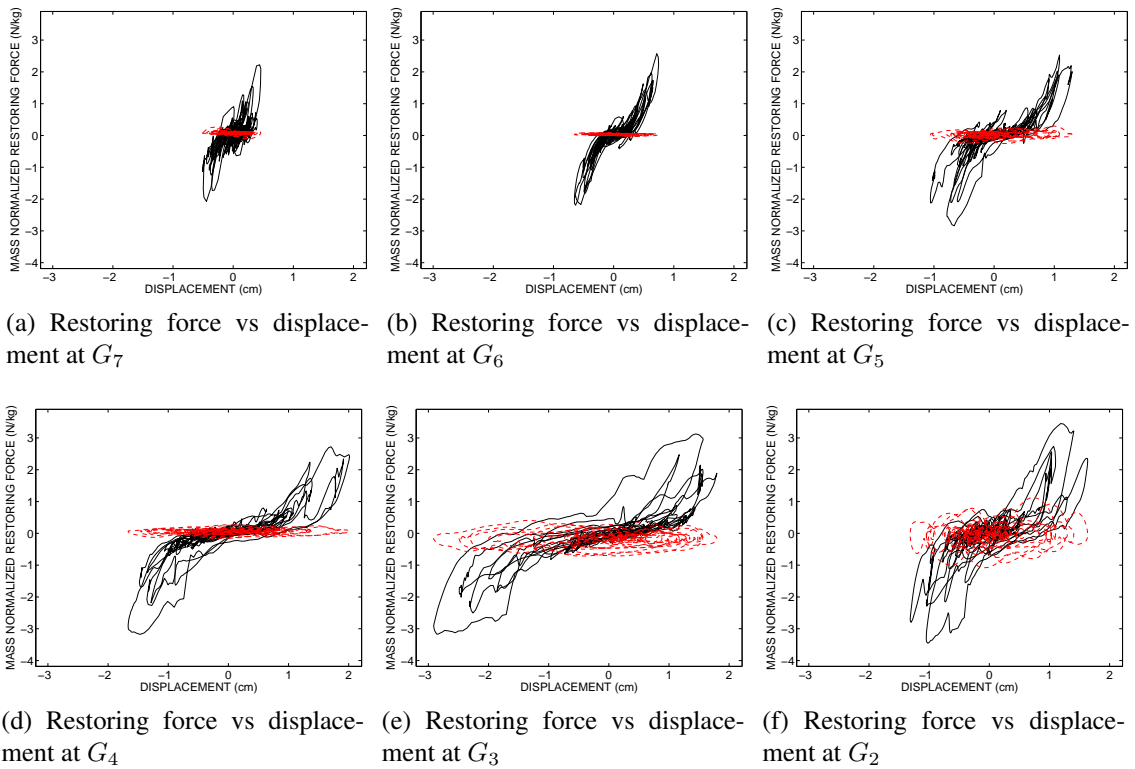


Figure 4.25: Term wise phase Diagrams of restoring force vs displacement with the first order damping-like coefficient a_{01}^m only used to reconstruct the restoring force plotted for Shanghai excitation level 6 for the fixed foundation model at (a) G_2 (b) G_3 (c) G_4 (d) G_5 (e) G_6 (f) G_7 .

Figure 4.25 shows the hysteresis in the displacement phase diagrams are contributed largely by the a_{01}^m term. The hysteresis can be seen decreasing from 4.25 (a) to 4.25 (e). The expected damping energy should decrease as these hysteresis decrease.

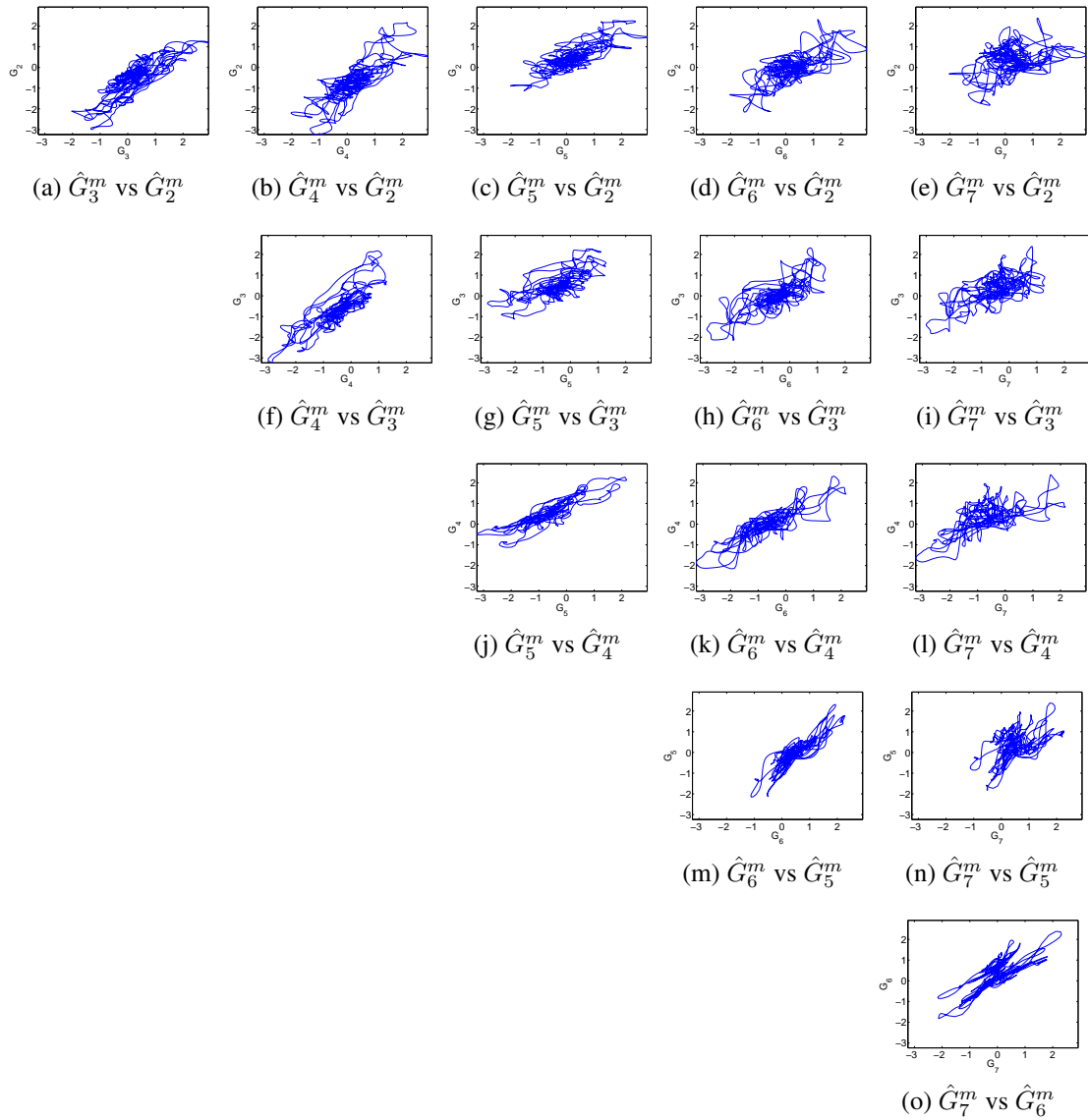


Figure 4.26: Reconstructed mass normalized restoring forces plotted against other reconstructed mass normalized restoring forces for Shanghai excitation level 6 for the fixed foundation model (a) \hat{G}_3^m vs \hat{G}_2^m (b) \hat{G}_4^m vs \hat{G}_2^m (c) \hat{G}_5^m vs \hat{G}_2^m (d) \hat{G}_6^m vs \hat{G}_2^m (e) \hat{G}_7^m vs \hat{G}_2^m (f) \hat{G}_4^m vs \hat{G}_3^m (g) \hat{G}_5^m vs \hat{G}_3^m (h) \hat{G}_6^m vs \hat{G}_3^m (i) \hat{G}_7^m vs \hat{G}_3^m (j) \hat{G}_5^m vs \hat{G}_4^m (k) \hat{G}_6^m vs \hat{G}_4^m (l) \hat{G}_7^m vs \hat{G}_4^m (m) \hat{G}_6^m vs \hat{G}_5^m (n) \hat{G}_7^m vs \hat{G}_5^m (o) \hat{G}_7^m vs \hat{G}_6^m .

Figure 4.26 shows several important characteristics of the system. The shape of the image can reveal several key relationships: decrease in amplitude during propagation, phase delay, possible damage to the structure. The decrease in amplitude can be imagined as a somewhat

linear relationship on the Figures. The slope is roughly the ratio of energy transferred from one non-linear element to the next element. Figure 4.26 (a) - (e) will be an important comparison for understanding the way the energy decreased in amplitude during propagation. Figure 4.26 (a) and (b) show very similar slopes to each other. This indicates that the force prorogated from $\hat{G}_2^m(\bar{z}, \bar{z})$ to $\hat{G}_3^m(\bar{z}, \bar{z})$ and $\hat{G}_4^m(\bar{z}, \bar{z})$ is nearly equal. Next, is Figure 4.26 (c) and (d) these two both contain smaller slopes than the previous figures indicating that a decrease in the energy has occurred. The rest of the figures can be interpreted similarly.

Energy Dissipation

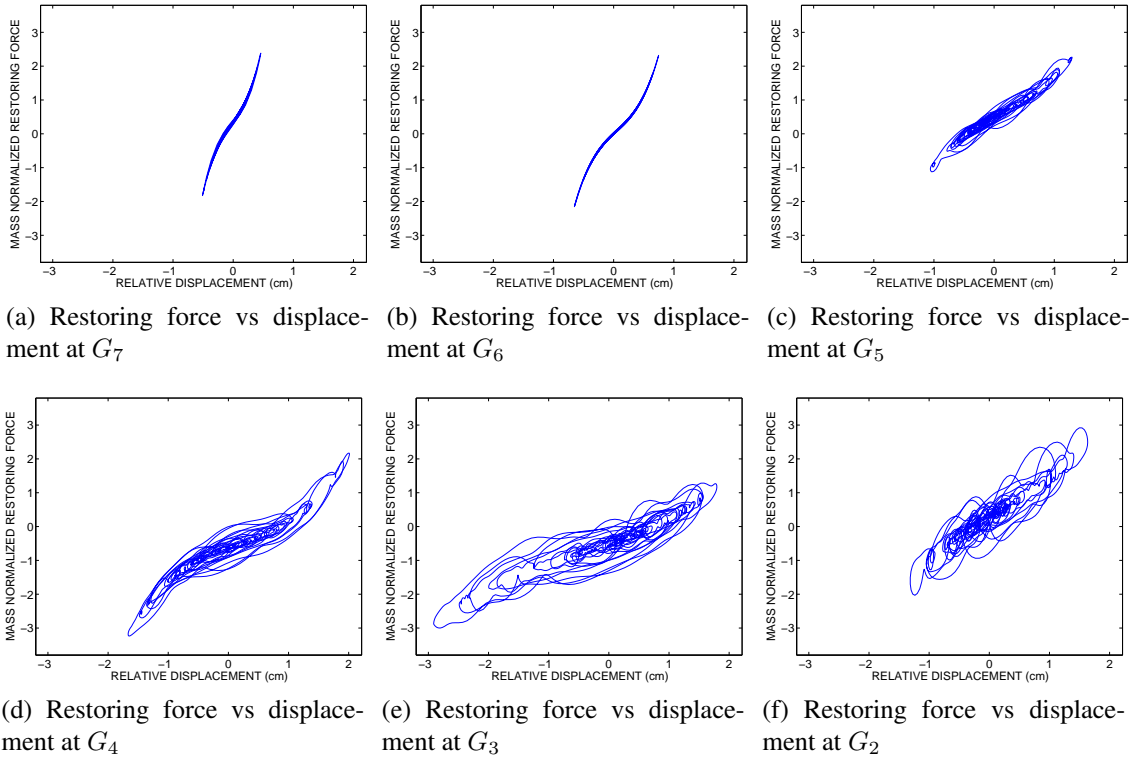


Figure 4.27: Term wise phase diagrams of restoring force vs displacement with the first order velocity dependent, first order displacement dependent, third order displacement dependent, Chebyshev coefficient used to reconstruct the restoring force plotted for Shanghai excitation level 6 for the fixed foundation model at (a) G_7 (b) G_6 (c) G_5 (d) G_4 (e) G_3 (f) G_2 .

Combining the three dominant term wise Chebyshev coefficients together and plotting them against the displacement helps to reveal the energy dissipated by the system, Figure 4.27 shows this plotted. The dissipated energy can be calculated by finding the area inscribed by the figure. The calculated values from Figure 4.27 are shown fully in Figure 4.28 as a plot of the calculated dissipated energy for each element vs the peak acceleration. It can be seen that the lower elements dissipate more energy than the higher elements and that the amount dissipated decreases at each successive element seems to decrease for Figure 4.27 (b) and (c), which is the box and pile foundation. However, in the fixed foundation seen in Figure 4.27 (a) the element

G_3 , representing the 3rd and 4th floors, dissipate more energy than the element below it. This is interesting and will be explained by damage later on in Subsection 4.3.5.

One feature that clearly creates a difference between the 3 excitations is the amount of energy dissipated by same foundations in each excitation type. This is why the Shanghai artificial wave record was selected as a representative case for the dissipated energy plots. While not as clear as the results from the Shanghai artificial wave the results from Kobe and El Centro wave records for the dissipated energy plotted in Figures 4.29 and 4.30 show some similar trends as Figure 4.27. As before for the fixed foundation in Figures 4.29 (a) is seen dissipating increasing amounts of energy at every level of excitation while the fixed foundation in Figure 4.30 (a) is seen dissipating increasing amount of energy only for the element G_2 . For the box foundation in Figure 4.29 (b) a steady rise in the dissipated energy can be seen only at the lowest elements G_2 and G_3 the rest of the elements remain nearly constant. Figure 4.30 (b) is particularly interesting because it shows a sharp rise in the dissipated energy only to return to the pre-peak levels, this may be to some shifting in the soil container causing greater interaction with the foundation where another shift may cause the interaction to return to normal. The pile foundation shows interesting trends also in Figure 4.29 (c) shows a sharp drop in dissipated energy after which the dissipated energy steadily climbs, Figure 4.30 (c) also shows a drop in dissipated energy for several elements but an increase in the lower elements until the lowest elements suffers a similar drop in dissipated energy.

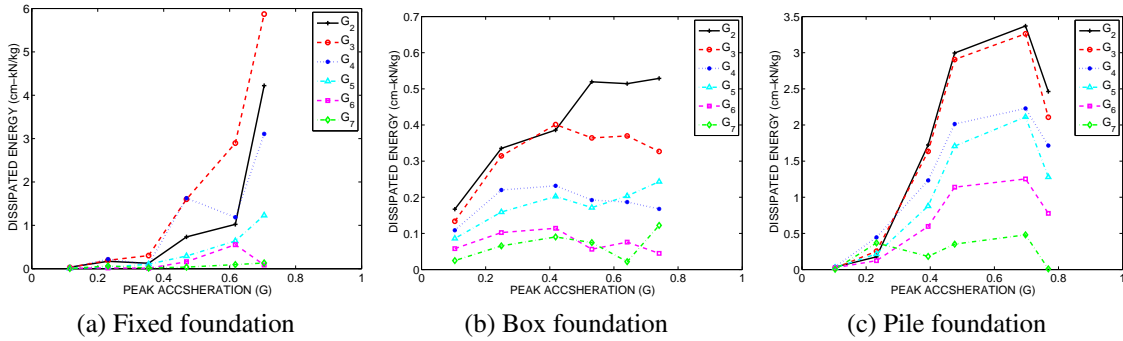


Figure 4.28: Plot of dissipated energy vs peak acceleration for the Shanghai artificial wave record (a) Fixed foundation (b) Box foundation (c) Pile foundation.

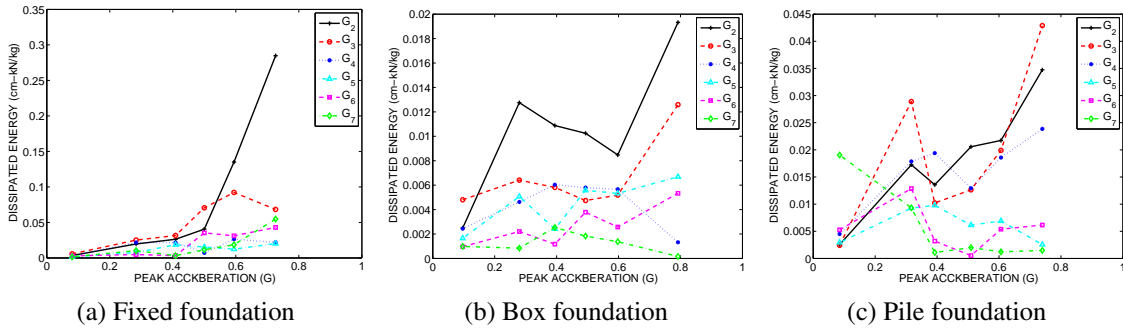


Figure 4.29: Plot of dissipated energy vs peak acceleration for the Kobe wave record (a) Fixed foundation (b) Box foundation (c) Pile foundation.

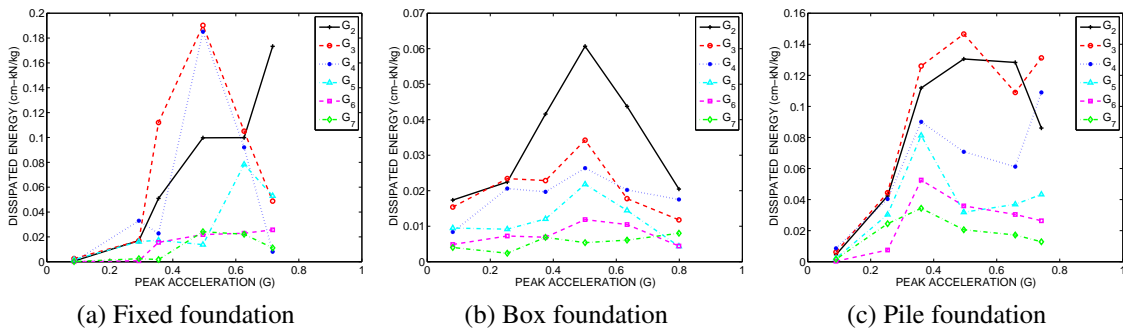


Figure 4.30: Plot of dissipated energy vs peak acceleration for the El Centro wave record (a) Fixed foundation (b) Box foundation (c) Pile foundation.

4.3.4 Effects Of Foundation

Since the original study was to help understand the different foundations and their effects, this subsection will pay homage to that study and focus on those effects and do some analysis. The most obvious effect of the foundation and soil system is the reduction in energy being sent into the superstructure. These effects can be seen for the Shanghai excitation levels in Figure 4.28. Although the Shanghai excitation will be used predominantly, because of its broadband nature, it is still advised to look at Figures 4.29 and 4.30. The fixed foundation would represent a system in which no energy is lost to the soil system, so most of the comparison will be made between the box foundation and the pile foundation since the soil system is similar in both. It is fairly obvious the effects of the different foundations and the energy. From Figure 4.28 (a), (b) and (c), representing the fixed foundation, box foundation and pile foundation, respectively. It can be discerned that the superstructure for the box foundation dissipates less energy than superstructure for the pile foundation suggesting, that pile foundation transfers more energy into its superstructure compared to the box foundation.

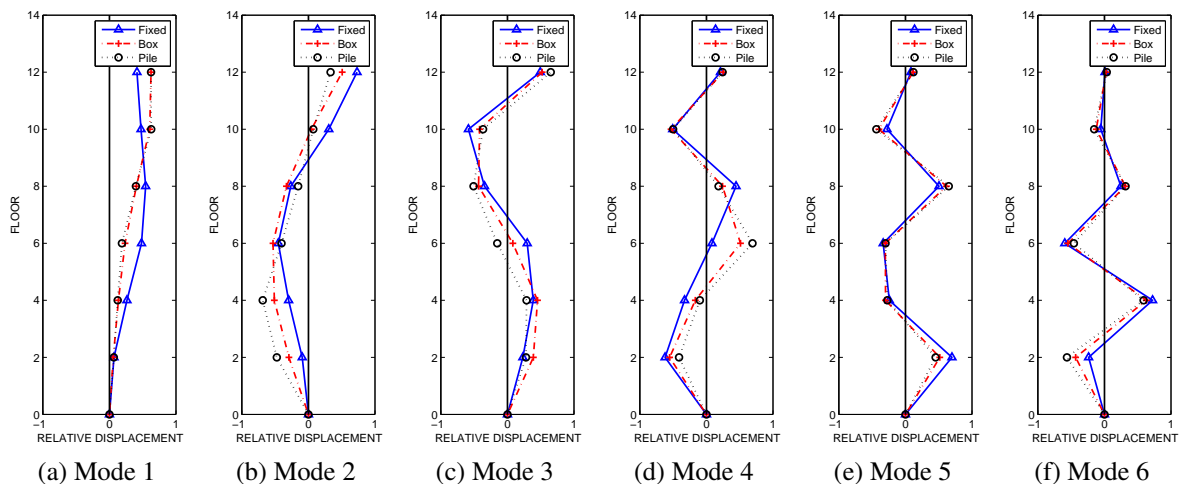


Figure 4.31: Mode shapes for Shanghai excitation level 1 for the fixed foundation model (a) 1st (b) 2nd (c) 3rd (d) 4th (e) 5th (f) 6th.

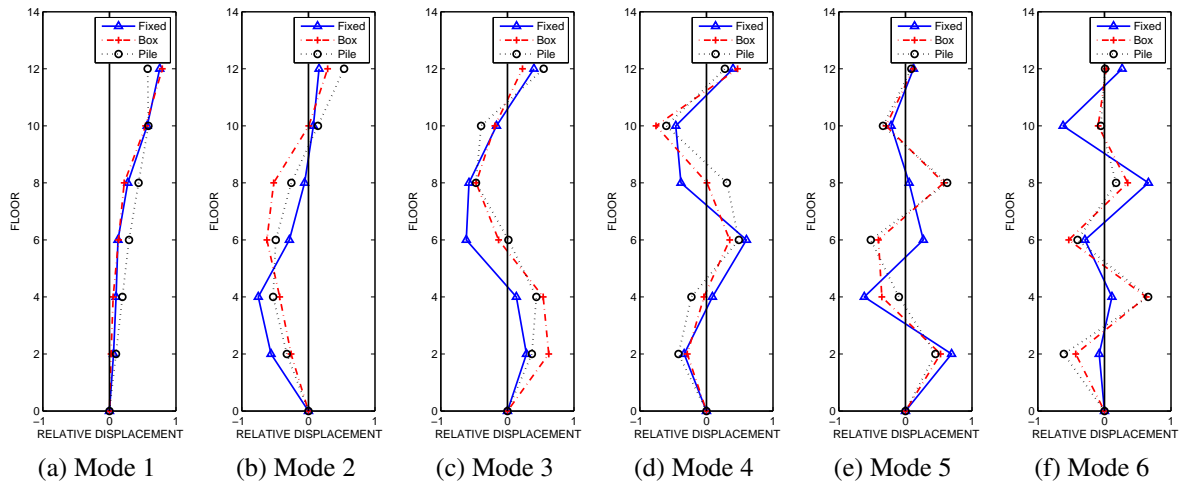


Figure 4.32: Mode shapes for Shanghai excitation level 3 for the box foundation model (a) 1st (b) 2nd (c) 3rd (d) 4th (e) 5th (f) 6th.

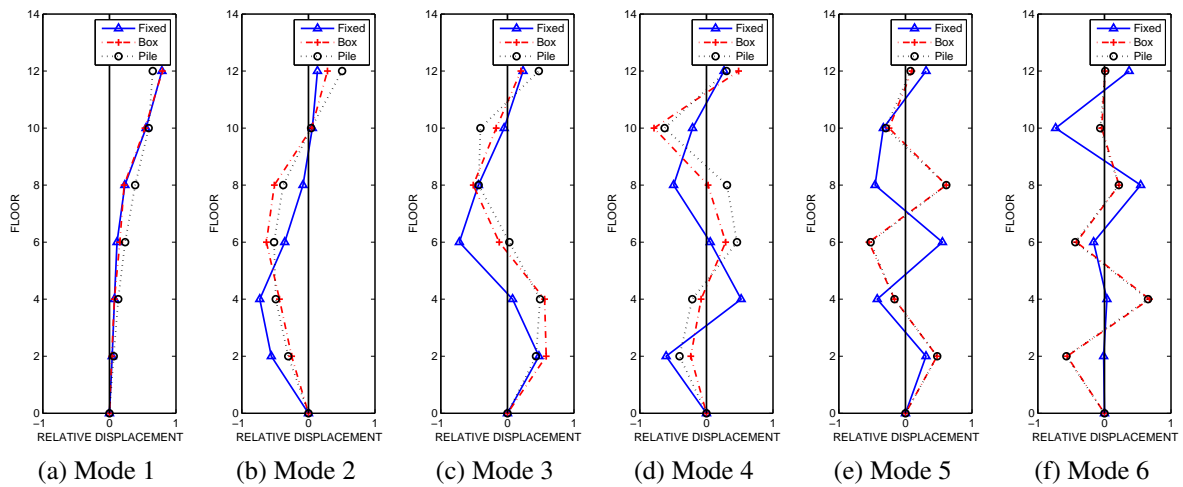


Figure 4.33: Mode shapes for Shanghai excitation level 6 for the pile foundation model (a) 1st (b) 2nd (c) 3rd (d) 4th (e) 5th (f) 6th.

Effects Of Foundation On Mode Shape

Another effect of the foundation can be seen by looking into the mode shapes. For the visual comparison of the mode shapes consult Figures 4.31, 4.32 and 4.33. Keep in mind the relative displacement along the x-axis is for the relative displacement for each mode shape. This provides a convenient measure to compare the mode shapes with. While visually very similar modes are achieved for the pile and box foundation, the fixed foundation is visually much different than the other foundation types. Often times, the pile and box foundations have very large sloping curves while the fixed foundation has much sharp bends in the structure.

4.3.5 Effects Of Damage

The effects of damage to the structure can be seen in a few different ways. To start with on the foundation itself. By examining Figure 4.28 (b), which shows dissipated energy at peak acceleration for the pile foundation. The pile foundation shows higher amounts of dissipated energy and finally a sharp decrease at all elements for the highest level of excitation corresponding to a peak acceleration of 0.798 G. This sharp decrease may be explained by a lower transfer of energy into the system because of a broken pile system. Which, the experimental observation noted that there was sever cracking along the pile foundation after the test. With less energy in the system there needs to be less damping. The fixed foundation was not damaged because the foundation itself was part of the shaker table. For the box foundation no damage was reported to the foundation. This explains both of these foundations in continual dissipation in energy.

The effects of damage on the superstructure can be seen through a plot of the power series vs the peak acceleration. This will be crossexamined with the mode shapes in Figures 4.31, 4.32 and 4.33. The mode shapes can show where damage is likely to occur and the decrease in the power series coefficient at that particular location will help to confirm this. Ultimately, the results are to be compared against the report experimental observation on the cracking and see if it confirms some of the results from the mode shape and power series coefficients.

While plotting the power series coefficients it was decided to remove the first two levels of excitation because it was believed that the structure wasn't fully excited then and these would yield in accurate results. First, the mass normalized power series coefficients a_{10}^m , a_{30}^m , and a_{01}^m , which were chosen because of their dominant nature in the recreation of the estimated mass normalized restoring force, these are plotted against the peak acceleration. Damage can be detected by a decrease in the stiffness at higher levels of excitation. For this purpose the plots of a_{10}^m and a_{30}^m are important, for the Shanghai excitation level these plots appear in Figure 4.34 (a),

(b) for the fixed foundation, Figure 4.34 (d), (e) for the box foundation, Figure 4.34 (g), (h) for the pile foundation.

Starting with the fixed foundation, by looking at the fixed foundation a_{10}^m in Figure 4.34 (a), a steady decline at higher increments of peak acceleration can be seen, this indicates damage has occurred on the structure and changed the stiffness. The cracking mentioned in Section 4.1.7 confirms cracking along the superstructure. Another expected results is that there should be an increase in damping on the structure, this can be seen if compared with Figure 4.34 (c), although there is some instances of an increase in damping it is difficult to make a significant case for most of the elements, since the damping coefficients are small and any changes are themselves small, Instead focusing on elements, G_2 representing floors 1 and 2, and G_3 representing floors 3 and 4 respectively. Observing these coefficients is an increase in the damping this could be explained by increase in cracks on the columns in that area. The cracks would increase friction which in turns results in higher damping values. This is mentioned before in the Section 4.1.7 that cracking has occurred along columns running from floors 1 to 4. For the box foundation there was not noticeable damage to the structure the plots in Figures 4.34 (d) and (e) do not show much in way of change to the stiffness of the structure and Figures 4.34 (f) shows a decrease in the damping coefficients. Finally the pile structure, as can be seen in Figure 4.34 (g) a decrease in the first order linear stiffness is visible however there is an increase in the nonlinear third order stiffness in 4.34 (h), but upon closer observation it can be seen that this is because the third order had very week contributions to begin with so there truly isn't much of a change just more contribution probably from the higher excitation. The damping coefficients associated with the pile foundation do not change much in Figure 4.34 (i), the cracking in the pile foundation was less sever than that of the Fixed foundation so it is of no surprise that these coefficients have not changed much.

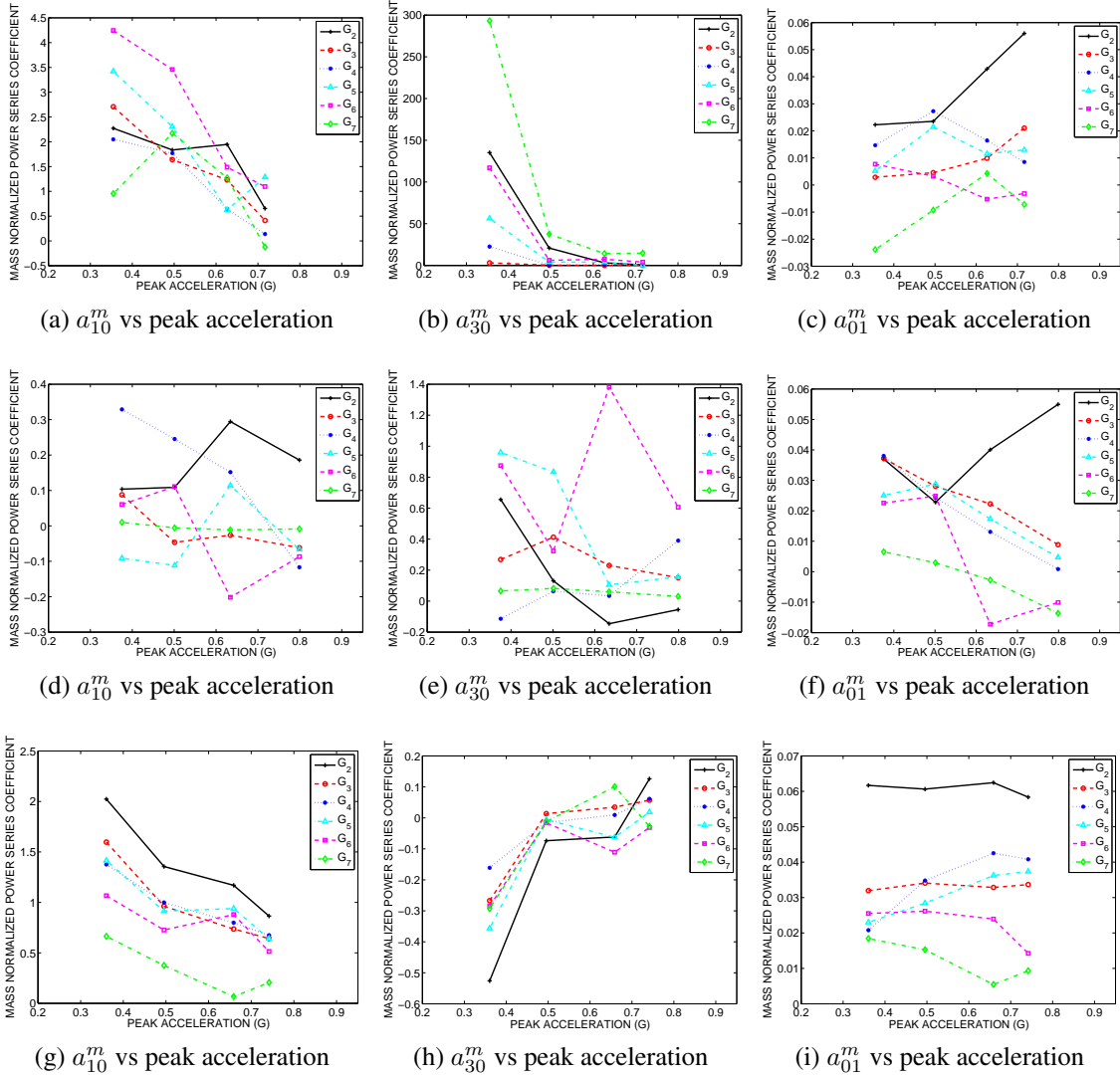


Figure 4.34: Plot of mass normalized power series coefficients vs. peak acceleration for the Shanghai artificial wave record with the following foundation type and coefficient (a) Fixed foundation a_{10}^m (b) Fixed foundation a_{30}^m (c) Fixed foundation a_{01}^m (d) Box foundation a_{10}^m (e) Box foundation a_{30}^m (f) Box foundation a_{01}^m (g) Pile foundation a_{10}^m (h) Pile foundation a_{30}^m (i) Pile foundation a_{01}^m .

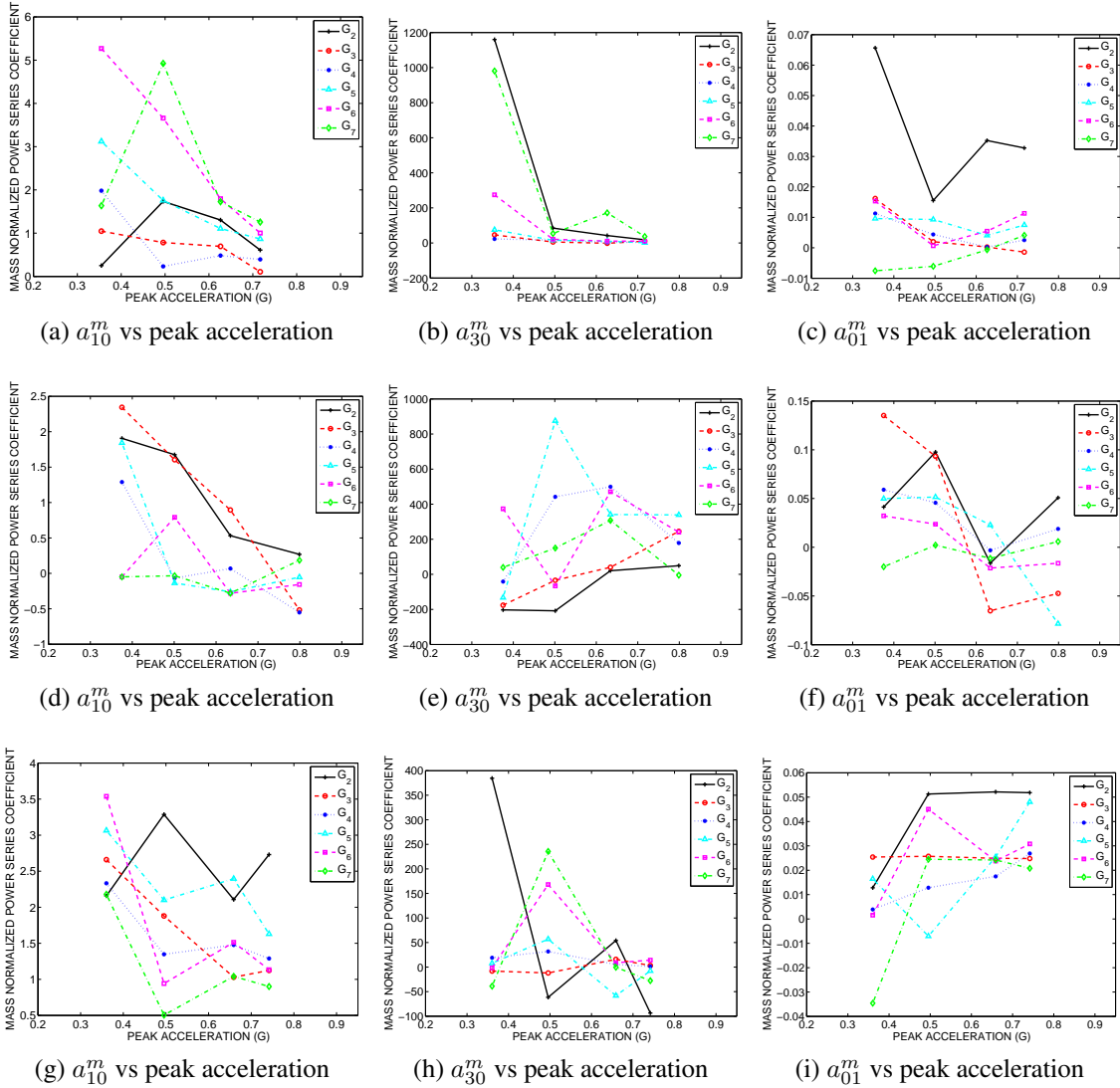


Figure 4.35: Plot of mass normalized power series coefficients vs. peak acceleration for the Kobe wave record with the following foundation type and coefficient (a) Fixed foundation a_{10}^m (b) Fixed foundation a_{30}^m (c) Fixed foundation a_{01}^m (d) Box foundation a_{10}^m (e) Box foundation a_{30}^m (f) Box foundation a_{01}^m (g) Pile foundation a_{10}^m (h) Pile foundation a_{30}^m (i) Pile foundation a_{01}^m .

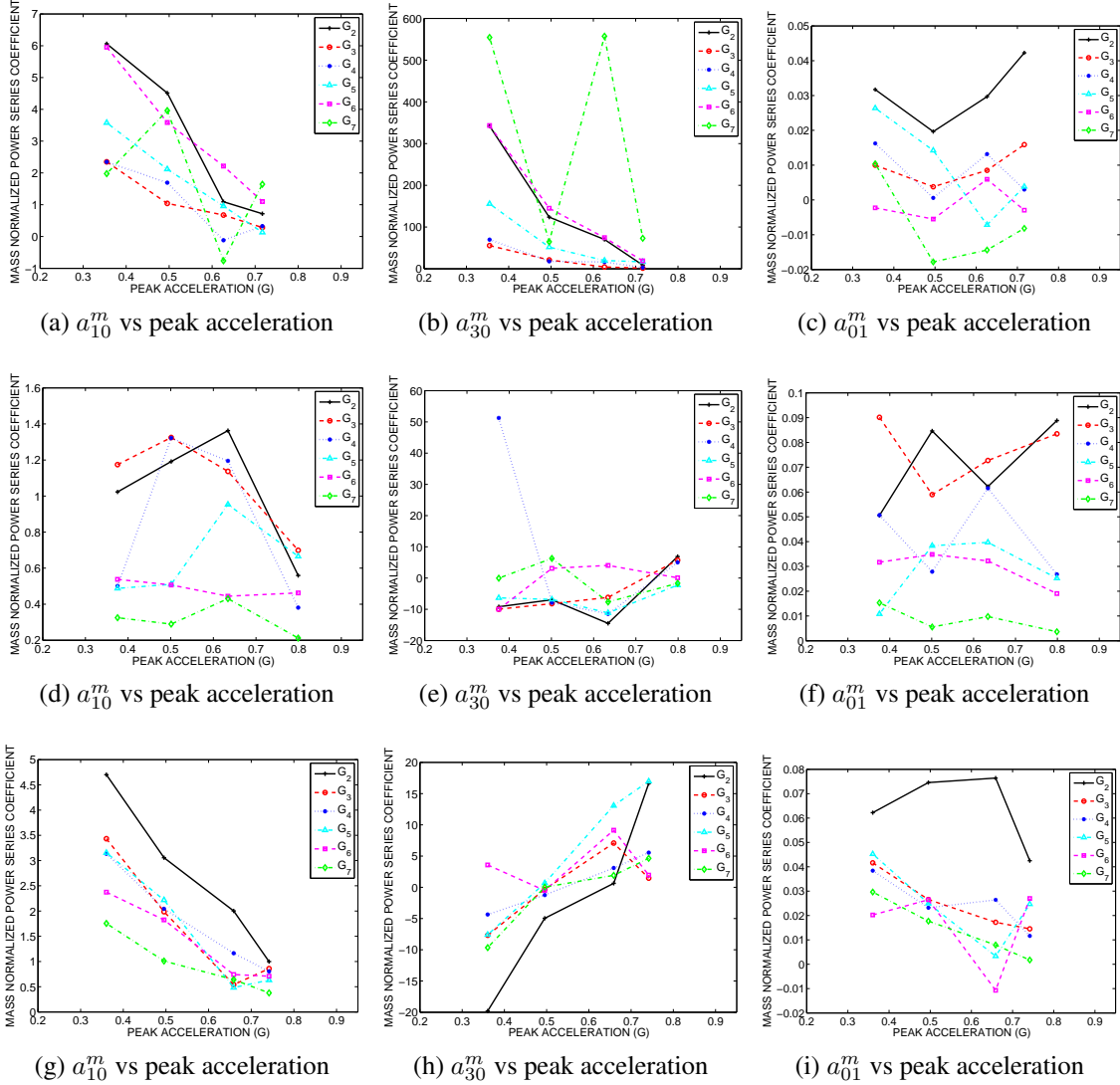


Figure 4.36: Plot of mass normalized power series coefficients vs. peak acceleration for the El Centro wave record with the following foundation type and coefficient (a) Fixed foundation a_{10}^m (b) Fixed foundation a_{30}^m (c) Fixed foundation a_{01}^m (d) Box foundation a_{10}^m (e) Box foundation a_{30}^m (f) Box foundation a_{01}^m (g) Pile foundation a_{10}^m (h) Pile foundation a_{30}^m (i) Pile foundation a_{01}^m .

5 EXPERIMENTAL NONLINEAR IDENTIFICATION FOR SMALL SCALE WIND TURBINE BLADE

With concerns for global warming alternative energy sources are becoming extremely popular. One of the popular alternative energy sources is wind turbines. As demand for wind energy grows so does the size of the wind turbines, and the remoteness of the locations. Both of these changes in the wind industry has encouraged research into materials better suited for higher strength, to deal with the increased size and materials that will have lower maintenance, for those blades in remote locations. Additionally, the size and remoteness of wind turbines has increased the importance for monitoring system in wind turbines (Yang et al., 2010). This study will focus on two things, the proposal of using the MDOF RFM for structural monitoring of the blades and ways that the results can be used for comparing material properties of the basalt fiber blade to other blades.

5.1 Background

On the material side, basalt fiber is becoming increasingly more common in many different civil engineering applications (Quagliarini et al., 2012). This is because basalt fiber is thought to be an alternative to both carbon fiber and glass fiber, because it offers competitive strength compared to glass fiber (Deak and Czigany, 2009) and considerable cost savings over carbon fiber (Rosa et al., 2011). In addition with the goal of wind turbines being a "green" energy basalt fiber offers an environmentally friendly material (Deak and Czigany, 2009). A series of experiments were conducted to investigate the behavior of basalt fiber wind turbine blades. Although most wind turbine blades are composed of glass fiber or carbon fiber, basalt fiber was proposed in this study as an alternative that would be cost-effective and comparative in strength to glass fiber. Future studies were planned to include a comparison between wind turbine blades composed of basalt fiber, glass fiber, and carbon fiber.

5.2 Literature Review: Wind Turbines

5.2.1 Introduction

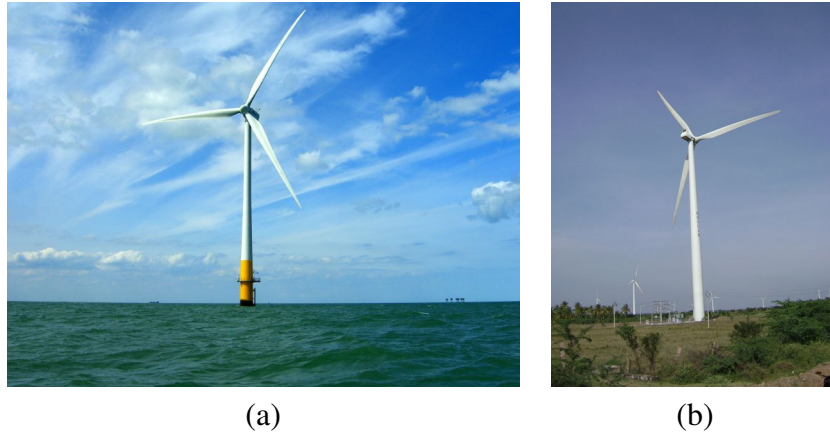


Figure 5.1: (a)An offshore wind turbine Source: (Hollman, 2006) (b) a land-based wind turbine Source: (Sherman, 2008)

Wind turbines can be either offshore or land-based. The location of the turbine can affect cost, noise, aesthetics, and the wind potential. Land-based wind turbines can be located in a variety of different terrains, e.g., mountains and plains. There are three subtypes of offshore turbines, i.e., shallow water (30m or less), transitional water (30m to 60m), and deep water (greater than 60m). This section will analyze the advantages and disadvantages of each.

Land-based wind turbines have a distinct advantage of being lower cost. The higher cost associated with offshore wind turbines is attributed to the higher cost for foundations, installations, operation, and maintenance (Musial et al., 2006). Offshore turbines do however have greater future size capacity since larger turbines are easier to transport on the water. Additionally cost curves are lower for offshore turbines compared to onshore turbines (Morgan and Jamieson, 2001).

Floating turbines are a very attractive option. The turbines can be located in deep water far from shore. Compared to land-based and shallow water wind turbines they have the potential

to access much higher wind speeds, lower environmental impacts on wildlife, and have little to no visual impact (Clarke et al., 2009).

Table 5.1: Comparison of Advantages and Disadvantages of Offshore and Land-based Wind Turbines.

<i>Turbine Type</i>	<i>Advantage</i>	<i>Disadvantage</i>
Land-based Wind Turbines	<ul style="list-style-type: none"> - Lower Cost - Easier operation - Easier maintenance 	<ul style="list-style-type: none"> - Noise emissions more likely to disturb populace - Lower wind potential
Offshore Wind Turbine	<ul style="list-style-type: none"> - Noise emissions unlikely to disturb populace - Higher wind potential 	<ul style="list-style-type: none"> - Higher Cost - Maintenance is more difficult - Operation is more expensive

5.2.2 Floating Wind Turbine Structural Design

Floating wind turbines require a floating structure that can support the weight of the turbine and restrain pitch, roll, and heave motions within acceptable limits. For a wind turbine, large wind-driven overturning moments dominate the design (Musial et al., 2006). Wave-loading also affects the design considerations.

Weight reduction is critical in the structural design of floating wind turbines. The lower the weight the less buoyancy structure is required. The heaviest component of the structure is the tower. Lightweight materials may help to reduce tower weight. Lightweight aggregates in concrete could help reduce concrete options 40% below standard mixtures. There is also a trend towards direct drive generators, which are smaller and more reliable than modular gear driven generators (Butterfield et al., 2005).

5.2.3 Floating Wind Turbine Subtypes

Within floating turbines there are several subtypes. Three of the main proposed subtypes can be seen in Figure 5.2. From left to right those are ballast stabilized (spur-buoy), Mooring Line stabilized, and buoyancy stabilized (barge).

The ballast stabilized uses a catenary mooring systems to keep it in place. This is advantageous because of the low cost for the anchors. To prevent overturning, significant ballast must be added below the center of buoyancy. Because of their nature, catenary mooring systems subject the wind turbine to larger base motion in all directions because they lack vertical tension. This could increase additional cost for the turbine (Musial et al., 2003).

Mooring line stabilized platforms use a submerged structure through the use of vertical moored anchors. This system provides the highest stability level and may be the lowest near term risk. A tension leg platform uses multiple legs spread out on either side of the base. The largest portion of the structure is kept submerged and well below the water line to reduce wave loading. Additionally, reserve buoyancy is kept in the base to prevent the tendons from losing tension even in extreme conditions. This system requires tendons and anchors which can withstand greater force than what is seen in the ballast stabilized design. Therefore there is a greater cost associated with the anchors for Mooring line stabilized platforms (Musial et al., 2003).

The buoyancy stabilized system uses distributed buoyancy. It takes advantage of the weighted water plane area for a righting moment. Additionally it also uses a catenary mooring system to keep it in place (Butterfield et al., 2005).

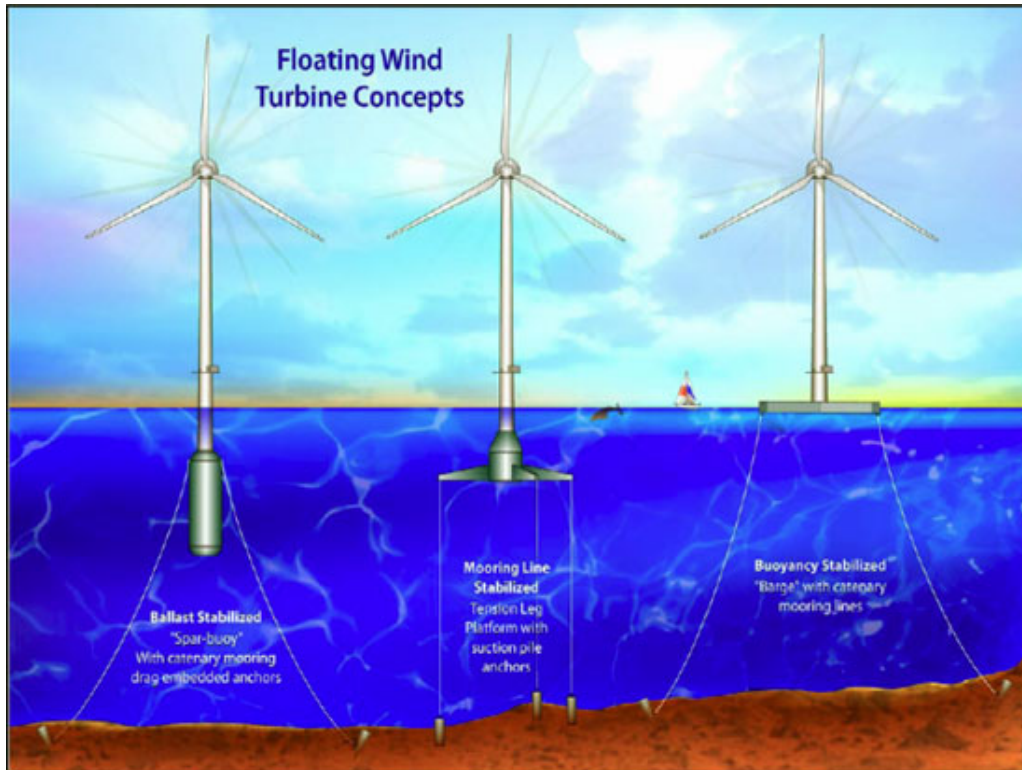


Figure 5.2: Three of the subtypes of floating wind turbines Source: (U.S. National Renewable Energy Laboratory, 2011)

5.2.4 Wind Potential

Wind speed increases as the distance out to sea increases. This increase in wind speed can be seen in Figure 5.3. Not only does the wind speed increase, but the variation of direction decreases. A floating wind turbine far out to sea ensures that it receives constant strong winds.

Stronger winds and more constant supplies will increase production and will help to offset the higher cost of floating wind turbines.

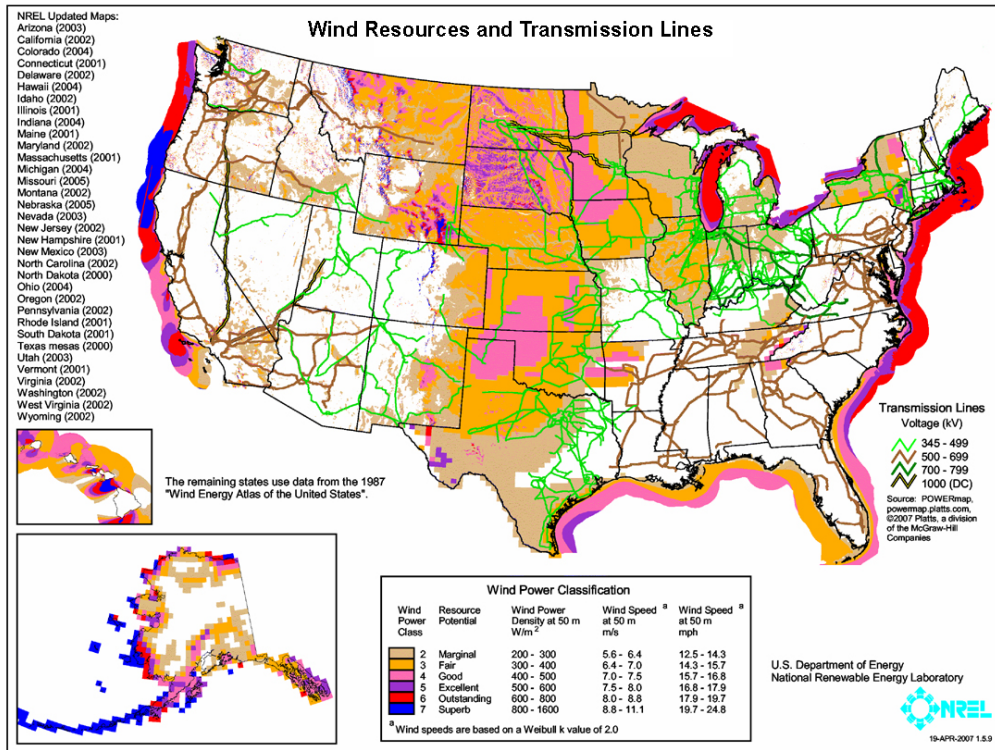


Figure 5.3: Map of Potential Wind Energy In The United States Source: U.S. National Renewable Energy Laboratory (2007)

5.2.5 Hywind

The world's first full scale floating wind turbine was launched in 2009. This turbine was the Hywind pilot, a concept developed by Statoil a Norwegian oil and gas company. The project cost over USD\$71 million. This project was not designed to create a revenue but instead will help acquire knowledge that will benefit future generations of floating wind turbines. The Hywind pilot is a 2.3MW turbine with a 100 meter draft hull, 82.4 meter rotor diameter and a 65m turbine height (Sprey, 2009).

While a floating wind turbine has many advantages over both shallow water and land-based turbines, it is, however, generally unused because of the high cost. The floating wind turbines can capture energy from higher value wind sites, and there are fewer concerns about acoustic

emissions, environmental impacts, and aesthetic values. Hopefully, with the data gathered from Hywind, floating wind turbines will eventually become competitive.

5.3 Experimental Study

The experimental study was a preliminary study designed to collect several data sets and use different system identification techniques to see how they perform on the wind turbine blade.

5.3.1 Sample Preparation

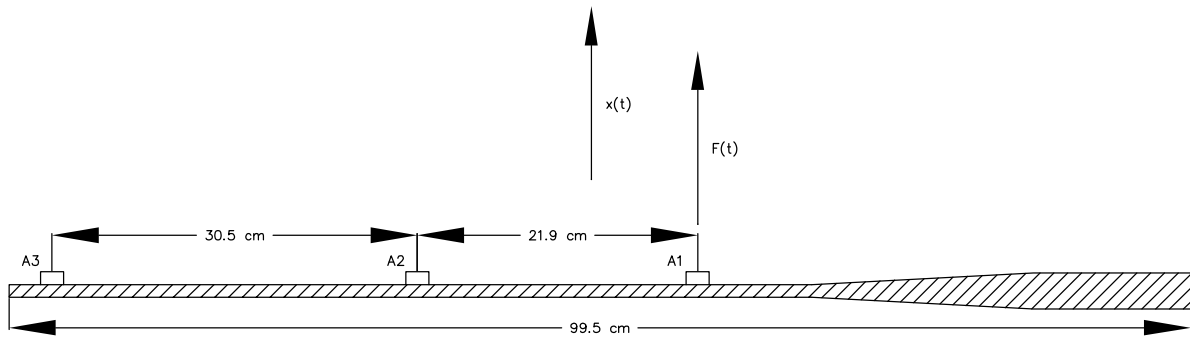
This study was a cooperative, interdisciplinary study with members of the UCF MMAE department: Dr. Gou and his student Fei Liang. They were responsible for the design and construction of the wind turbine blade and created it through a pre-impregnated process. The blade tested in this experiment was composed of basalt fiber with a PVC foam core and a polyester matrix. The density of the blade was found to be $.56 \text{ g/cm}^3$. This was determined through the measurement of the mass and the volume.



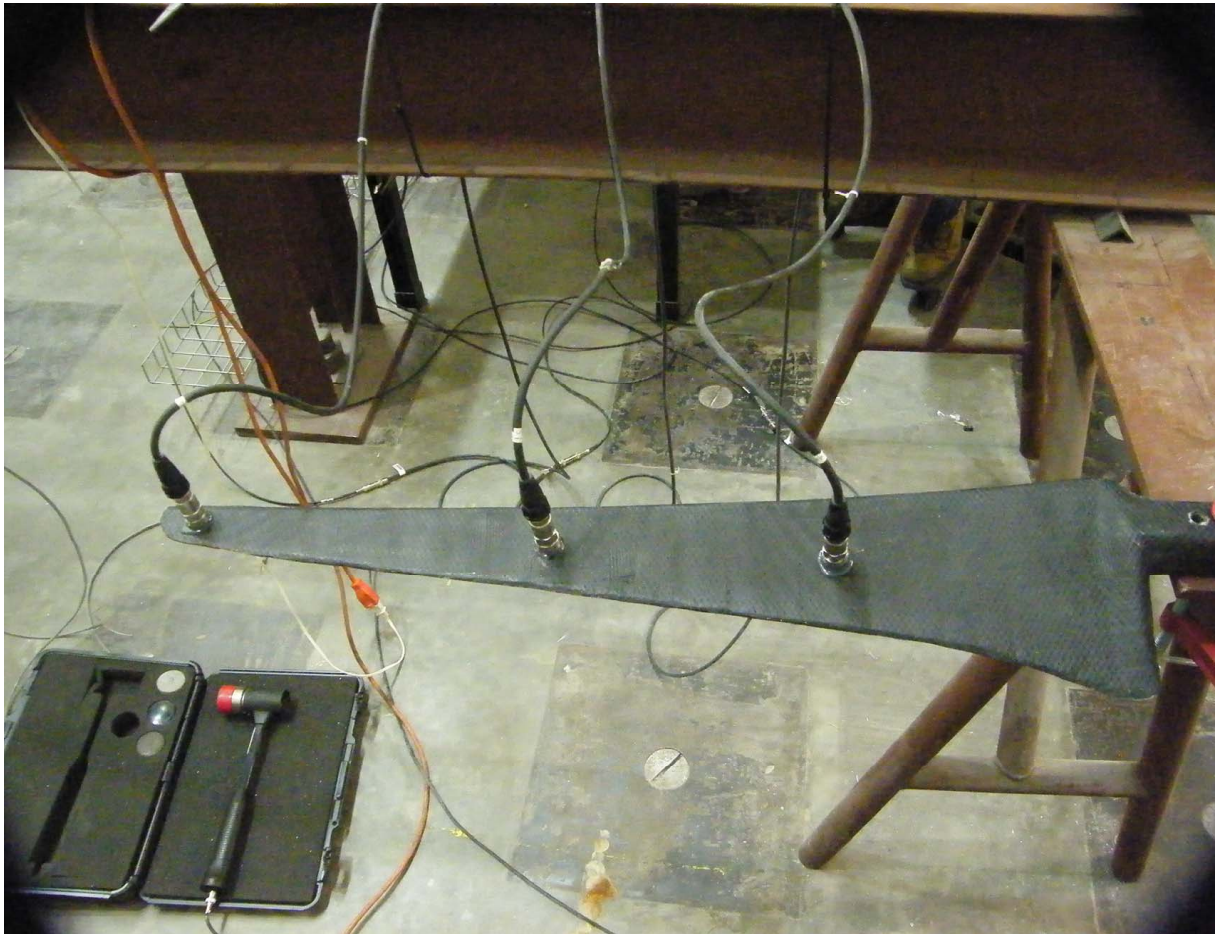
Figure 5.4: Photograph of the wind turbine basalt fiber blade.

5.3.2 *Instrumentation*

The blade was mounted with three accelerometers to acquire dynamic information about movement of the blade. The locations of each accelerometer was selected based on the thickness, and width of the blade at the location the sensor was placed. Another factor used in the selection of sensor location was distance from adjacent sensors. For this study data was collected from sensors A1 to A3 as indicated in Figure 5.5 (a). A3 is the tip of the blade while A1 is closest to the base of the blade. During the study, recordings were taken in the X-direction. In Figure 5.5 (b) is a photo to show how the blade was instrumented.



(a) Pile Foundation



(b) Box Foundation

Figure 5.5: Distribution of the accelerometers on the wind turbine blade with (a) An autocad drawing showing the direction of motion and the direction the force is applied in (b) A photograph with the blade fixed and instrumented.

5.3.3 Test Protocol

Test were only conducted in the X-direction indicated by Figure 5.5 (a). The X-direction was of interest because the blade would naturally be excited in this direction by wind during normal operation. The testing took place during June 2010.

The blade was fixed at its base through use of 2 large C clamps to a large metal table. The fixing of the blade was to imitate natural conditions where the blade would be fixed to the rotor. The blade was then excited through the use of a force measuring impact hammer. The hammer struck the blade directly below sensor A1. The excitation provided was a very quick impulse force, the results can be seen in Figure 5.6. The resulting recorded acceleration can be seen in Figure 5.7, please note this is not the raw data but rather the processed data.

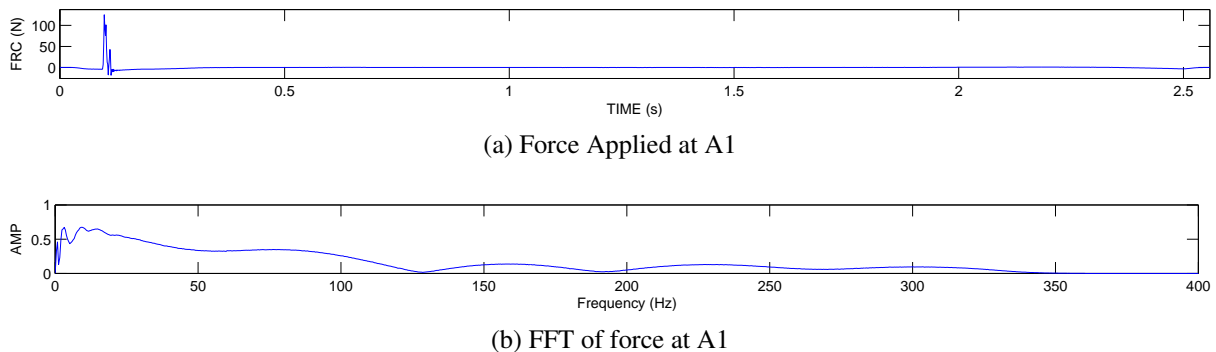
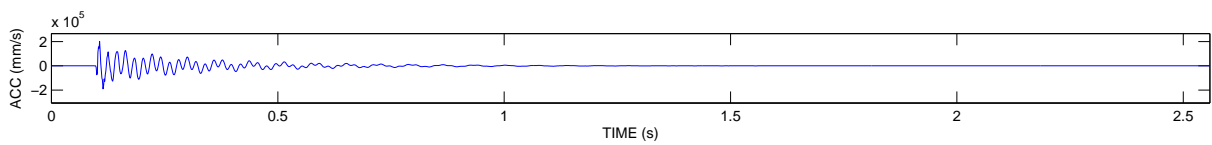


Figure 5.6: Plots of (a) The time history of the force applied to the turbine blade at A1 (b) The frequency spectrum of the applied force.

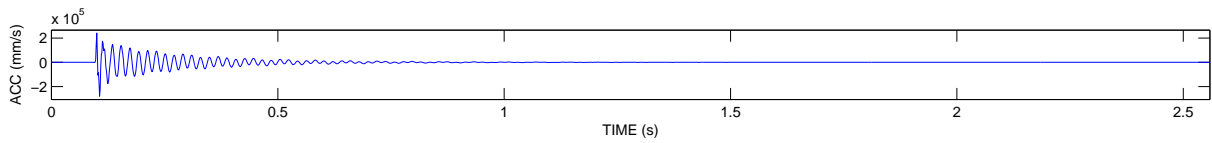
5.4 Preprocessing

Much like in Section 4.2 the data collected from this experimental study needed to be processed. The same method was used with a few exceptions. The recorded acceleration data was first detrended from the 15th order and filtered with a band-pass filter. The following properties for the filter were applied; the high filter passband was set to 1 Hz and the stopband was set to 0 Hz, passband ripple was set to 1 dB and the stopband attenuation was 60 dB; the high

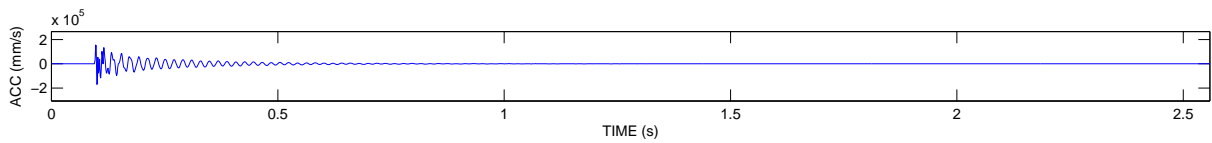
filter passband was set to 350 Hz and the stopband was set to 360 Hz, passband ripple was set to 1 dB and the stopband attenuation was 60 dB. After filtering, the acceleration data was then numerically integrated with respect to time using the MATLAB command “cumtrapz” to produce the velocity; velocity was then filtered with the same low pass filter and settings. Velocity was then numerically integrated in the same manner acceleration was to obtain the displacement data, which was then filter in the same way acceleration and velocity were. A sample of the acceleration and the calculated velocity, and displacement time history can be see in Figure 5.7, 5.8, and 5.9, which is the acceleration, velocity and displacement of the blade at all three points due to the excitation seen in Figure 5.6 (a) acting at A1.



(a) Acceleration at A_3



(b) Acceleration at A_2



(c) Acceleration at A_1

Figure 5.7: Time histories of the acceleration of the turbine blade at (a) A_3 (b) A_2 (c) A_1 .

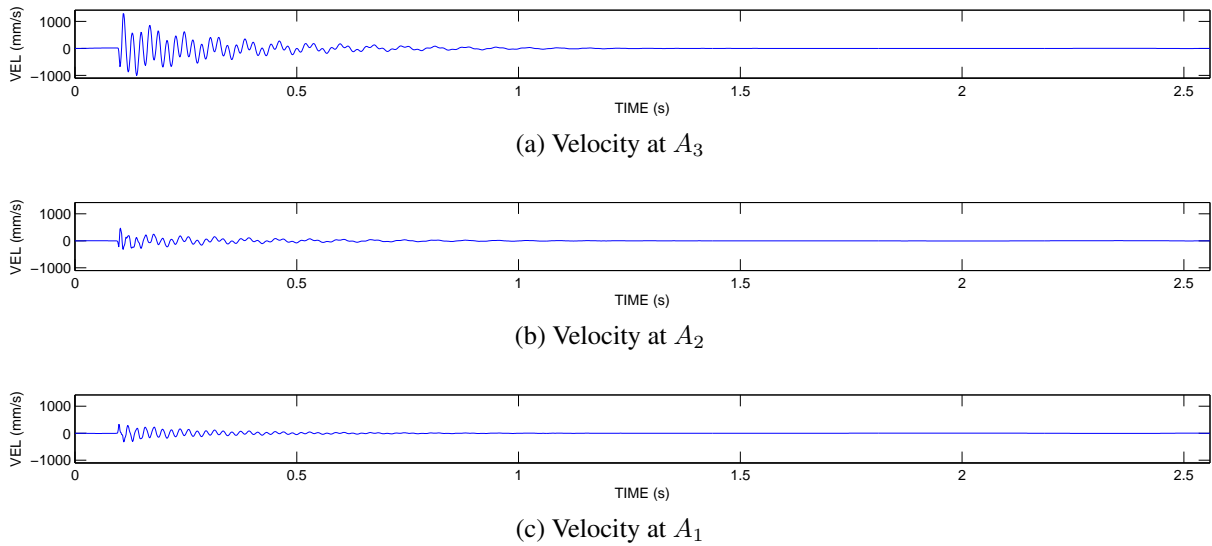


Figure 5.8: Time histories of the relative velocity of the turbine blade at (a) A_1 (b) A_2 (c) A_3 .

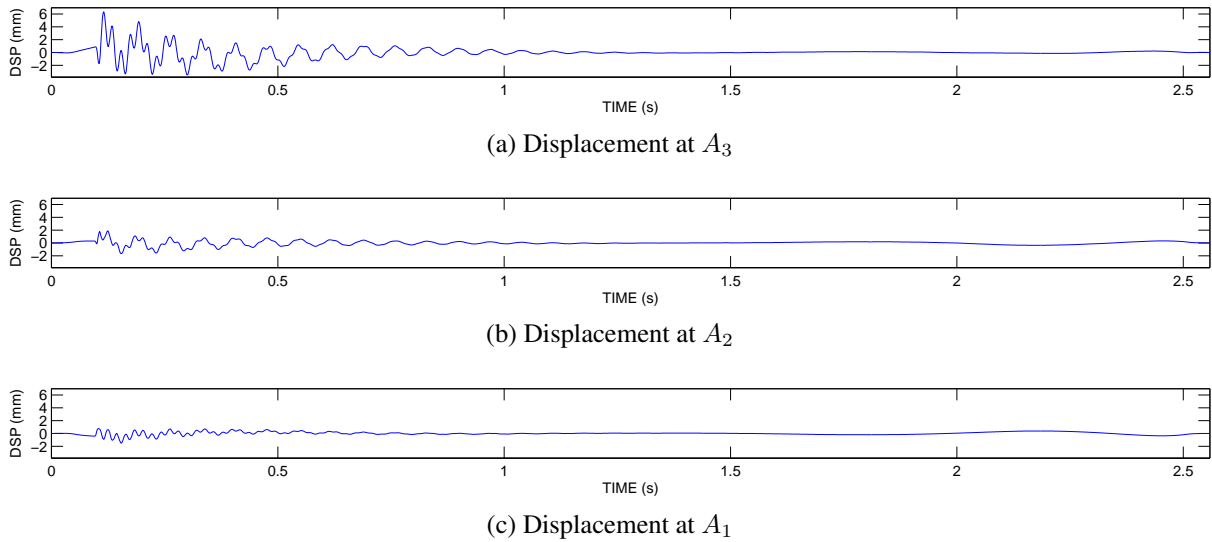


Figure 5.9: Time histories of the relative displacement of the turbine blade at (a) A_1 (b) A_2 (c) A_3 .

5.4.1 Restoring Force Estimation

After the measurements have been taken from the system, the restoring force was ready to be calculated. The restoring force will be calculated, unlike in Chapter 4 where the mass

normalized restoring force was calculated. This is because, the mass for each piece was easily calculated using the density and the volume and it could not be assumed that each mass was approximately equal.

To calculate the mass, the blade was treated as a lumped mass system. The system will be represented as a chain-like system with nonlinear elements interposed between sensors A3-A2, A2-A1 and A1 the base, these will be represented by G_3 , G_2 and G_1 , respectively. The midpoint between two adjacent sensors was considered the breaking point between the masses. The mass for sensor 3 was the volume, from tip to the midpoint between sensor 3 and 2, multiplied by the density, while the mass for sensor 2 was considered the volume from midpoint between sensor 3 and 2 to the midpoint between sensor 2 and 1. The volume of the blades was measured by using a water overflow displacement test. The blade was submerged until the first midpoint was reached. The water that was expelled during the overflow was weighed. The overflow vessel was then refilled; the blade was then submerged again until the second midpoint was reached. This process was repeated until volume was found over the entire blade. Since this method would find volume from tip to every midpoint it was necessary to find from midpoint to midpoint this can be done by the, subtraction of the previous volumes. With the volumes known one must simply multiply by the density to find the mass.

Now with mass and acceleration measured the restoring force can be calculated following Equation 2.21. This yields the results seen in Figure 5.10.

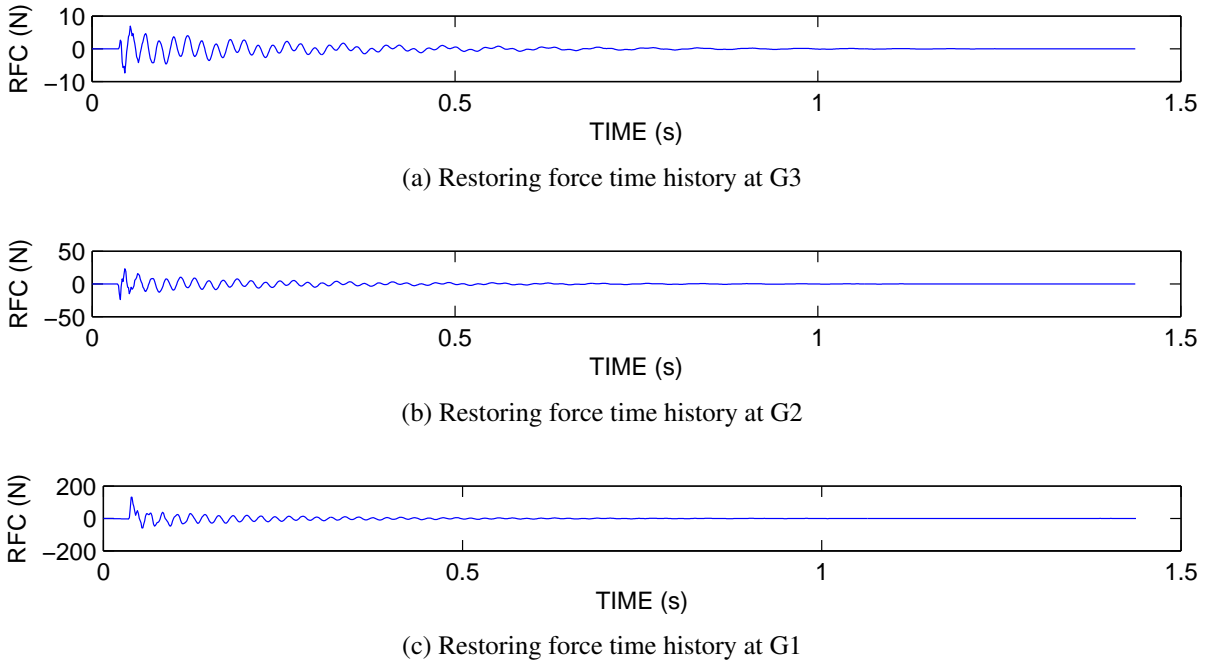


Figure 5.10: Time history of the measured restoring force for the wind turbine blade at (a) G_1 (b) G_2 (c) G_3 .

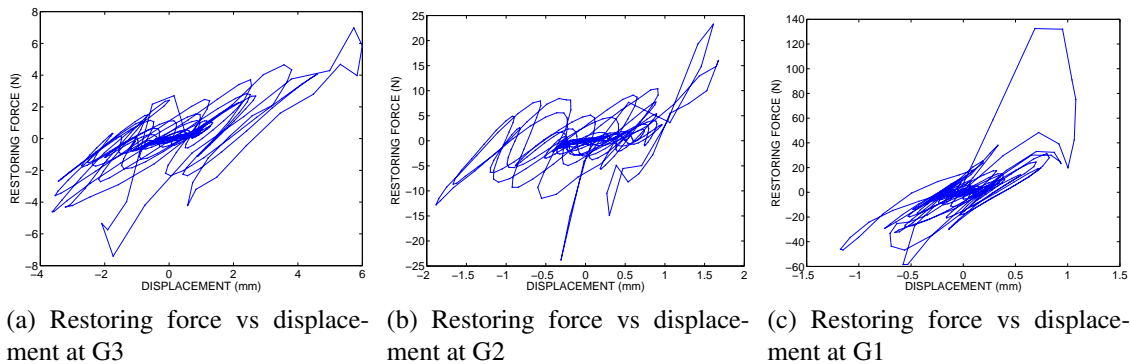


Figure 5.11: Phase Diagrams of restoring force vs displacement for wind turbine blade at (a) G_1 (b) G_2 (c) G_3 .

As mentioned before the phase diagram displays characteristics about the system. In Figure 5.11 is the phase diagram for restoring force vs displacement by looking at it can be interpreted that there is a strong contribution from stiffness and that this is nonlinear. These Figures show hardening in there phase diagram.

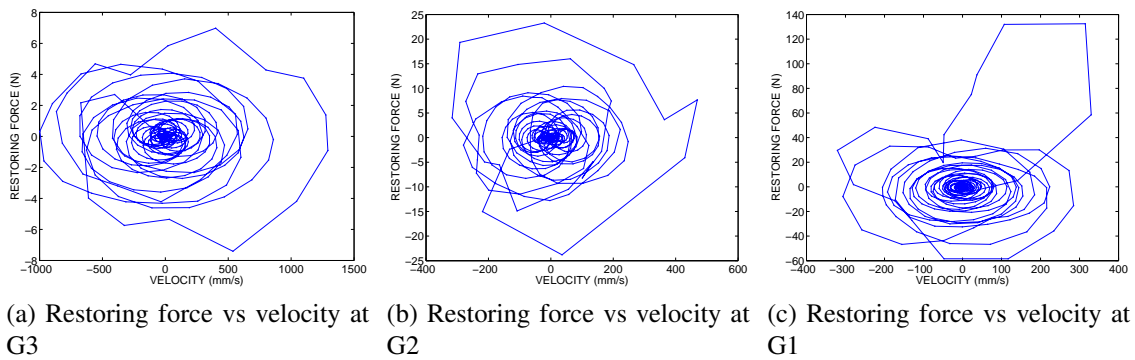


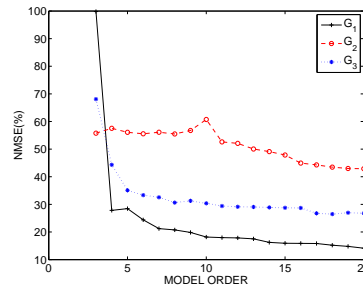
Figure 5.12: Phase Diagrams of restoring force vs velocity for wind turbine blade at (a) G_1 (b) G_2 (c) G_3 .

Similarly to investigate the relationship between restoring force and damping coefficient the phase diagram for restoring force vs velocity is plotted in Figure 5.12. It can mostly be seen that all of these restoring force velocity phase diagrams show a circular plot, this tends to show that the correlation between restoring force and velocity is weak and that the contribution from the damping coefficients is small.

5.5 Multidegree Of Freedom Restoring Force Method Results

With the restoring force calculated and the velocity and displacement for each degree of freedom calculated almost all of the data is ready to be input into the MDOF RFM. As mentioned earlier in Subsection 2.2, the input data must be in the form of interstory relative displacements, and interstory relative velocities. Through the use of Equations 2.16 and 2.17 the interstory relative displacement and interstory relative velocity was calculated. Now with the interstory relative velocities, interstory relative displacement and restoring force, the restoring force method can be used after selecting an appropriate model order.

To help select the model order Figure 5.13. Based on this figure a 6th order model was used.



(a) Fixed

Figure 5.13: Model order vs the NMSE for the wind turbine blade.

5.5.1 Error In Estimation

NMSE as described before in Section 4.3.1, was again used to calculate the goodness of fit of the results of which can be seen in Table 5.2. Overall the results show that some parts of the wind turbine are fitted much better than the rest and that noticeably G_3 , which is the element at the tip, shows the best fit. As explained before this is to be expected based on the way the MDFO RFM works.

Table 5.2: NMSE for the wind turbine blade for the three elements of the wind turbine blade.

<i>Wind Turbine Blade NMSE</i>			
<i>Element</i>	1	2	3
<i>NMSE</i>	19.82	56.75	31.26

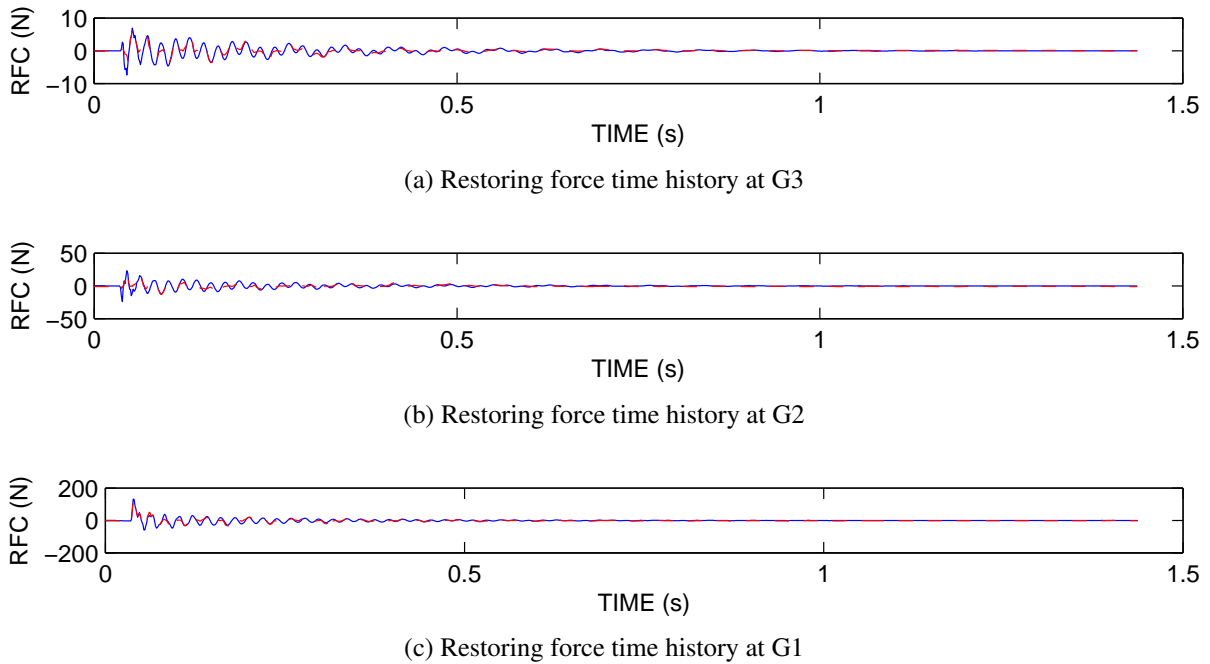


Figure 5.14: Time history of the measured restoring force, in blue, with the approximated restoring force, in red, overlapped for the wind turbine blade at (a) G_1 (b) G_2 (c) G_3 .

Again a visual fitting is important for the understanding of the error in the analysis. Figure 5.14 is plotted to ensure that the estimated restoring force, $\hat{G}_n(\bar{z}, \bar{\dot{z}})$, is close to the measured restoring force, $G_n(z, \dot{z})$, through means of visual comparison. Overall, the two restoring forces match relatively closely. Most of the major peaks overlay; however, some of the peaks are over estimated in Figure 5.14 (c).

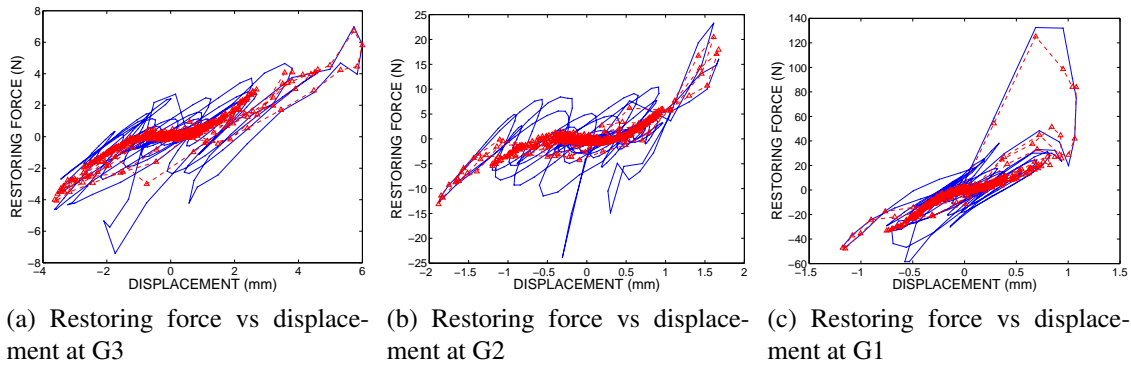


Figure 5.15: Phase Diagrams of restoring force vs displacement for wind turbine blade at (a) G_1 (b) G_2 (c) G_3 .

It is also important to make sure that the estimated restoring force, $\hat{G}_n^m(\bar{z}, \bar{\dot{z}})$, creates a displacement phase diagram similar to the measured restoring force, $G_n^m(\bar{z}, \bar{\dot{z}})$. This will ensure that the identified results carry over the similar stiffness system characteristics as the measured restoring force. By Figure 5.15 it is visible that for the phase diagram, for displacement vs. restoring force, a similar third order hardening is achieved in both measured and approximated restoring force. The overlap shows that most of the characteristics related to the stiffness are able to be accurately replicated except for the hysteresis.

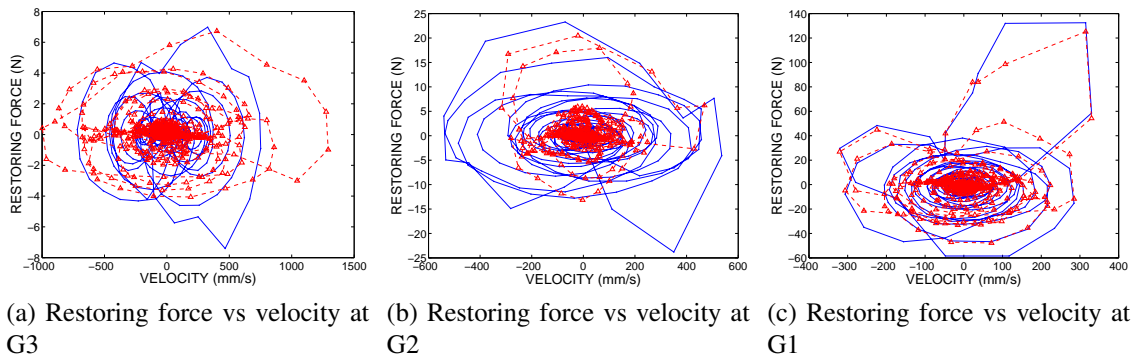


Figure 5.16: Phase Diagrams of the measured restoring force and approximated restoring force vs displacement for wind turbine blade at (a) G_1 (b) G_2 (c) G_3 .

Similarly, this visual comparison also applies to the velocity and restoring force, phase

diagram to ensure that the identified results carry over the same properties related to as the measured restoring force. By Figure 5.16 it is visible that for the phase diagram, for velocity vs. restoring force, a similar circular pattern. However, it is not an exact fit and in some case the approximated restoring force appears to be smaller than the measured restoring force as such in Figure 5.16 (b) this can probably help to explain that missing hysteresis.

5.6 MRFM For Wind Turbine Blade

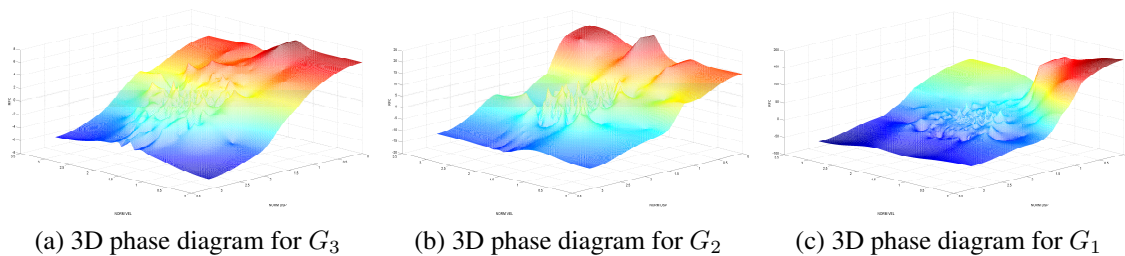


Figure 5.17: 3D phase Diagrams of restoring force vs normalized displacement vs normalized velocity for wind turbine blade at (a) G_3 (b) G_2 (c) G_1 .

Now the the phase surface is plotted in Figure 5.17 shows the phase surface that is to be fitted by the restoring force method. Again it is important to plot the phase surface because the MDOF RFM is a phase domain technique. The surface will vary by what interpolation and extrapolation technique is used. This is the surface created by the RBFs interpolation and extrapolation, that the RFM will fit. The slopes of the figure give insight into the damping and stiffness characteristics of the surface. It should be noted that the RBFs also capture any noise in the data and fit that to the surface too. This can explain the numerous small peaks and dips. While Figure 5.17 (a) and (b) both demonstrate a very well developed slope although highly noisy, Figure 5.17 (c) shows a poorly developed slope this is probably due to poor excitation to the system.

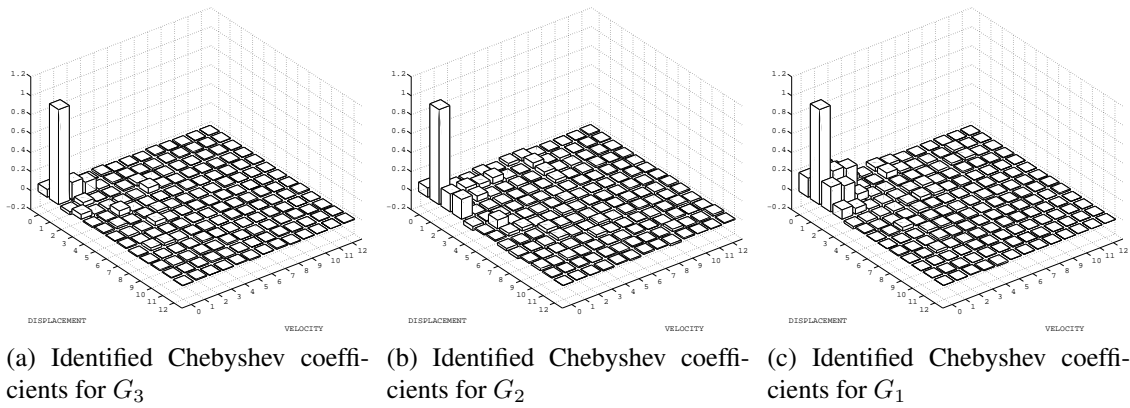


Figure 5.18: Identified Chebyshev coefficients for the wind turbine blade at (a) G_3 , floors 11 and 12 (b) G_2 , floors 9 and 10 (c) G_1 , floors 7 and 8

The first result from the MDOF RFM is the Chebyshev coefficients, these are seen in Figure 5.18. As explain in the previous Chapters 2 and 4, these coefficients are nonparametric but can be used to indicate contribution by stiffness-like coefficients and damping-like coefficients. The columns in Figure 5.18 represent restoring force dependencies on velocity, displacement or a couple effect of velocity and displacement. The numerical values along the left hand side of the 3d bar chart are for displacement terms and the numerical values on the right hand side are for velocity terms, the horizontal numerical numbers are for the actual value of the Chebyshev coefficient. So to understand the stiffness-like contribution, look at any of the values C_{i0} , where $i > 0$. Any value here would represent a contribution by only a stiffness-like term. Similarly C_{0j} , where $j > 0$, would represent a value by only damping-like term. From the phase diagrams, displacement and velocity in Figures 5.11 and 5.12, it was expected for a largely displacement dependent stiffness-like coefficients and very small velocity dependent damping-like coefficients. Interesting though is that while there was dominant stiffness-like terms in all these Figures 5.18 (a), (b) and (c), there were also relatively strong contributions from coupled terms meaning both a stiffness-like and damping-like term contribution. These terms are more dominant in 5.18 (c). It should be noted that the Chebyshev coefficients do not give a very

good indication of the nonlinearity of the system, for this it is best to look at the power series coefficients.

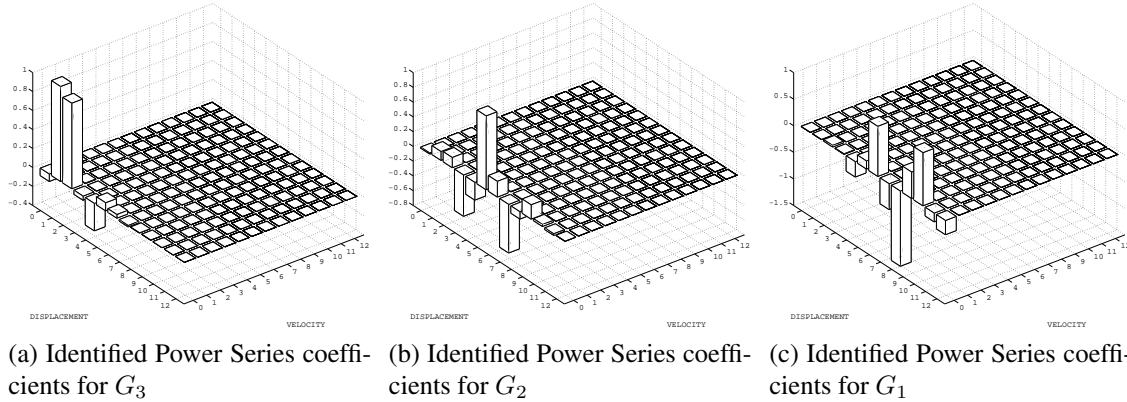


Figure 5.19: Identified power series coefficients for the wind turbine blade at (a) G_3 , floors 11 and 12 (b) G_2 , floors 9 and 10 (c) G_1 , floors 7 and 8.

5.7 Discussion

The MRFM was able to accurately describe the system characteristics of the wind turbine blade even with a high degree of nonlinearity in the system. Although there are some uncertainties relating to calculation of each lumped mass it is assured that because the way the MRFM as seen in Chapter 2, that at least element G_3 will have similar characteristics no matter what mass is used. However, error from the calculation of masses will pass on to both G_2 and G_1 . Most of the error from the mass calculation deviates from the assumption of a single uniform density throughout the blade. In fact the blade has the highest density when the basalt fiber is most numerous as the basalt fiber can weigh in at $2.8g/cm^3$ (Quagliarini et al., 2012) while the PVC foam core often used in wind turbine blades has a density of $0.063g/cm^3$ (Yang et al., 2013). In an actual application for wind turbine blades this would not be as much of a problem to calculate the mass since there would be numerous shop drawings with details relating to the thickness.

6 SUMMARY AND CONCLUSIONS

6.1 Summary And Conclusions

The results showed in each section are different and will be summarized by there parts. An overall summary suggest that the restoring force method was applied successfully to each respective section and valuable information was gained. First, the analytical section in Chapter 3, showed how the MRFM can be applied to a variety of linear and nonlinear systems. It also confirmed how using both a known mass and a known mass system can result in the same identification results, this is only true though when the assumptions about the mass normalized restoring force from Chapter 2 are held true. Second, the results from Chapter 4 showed the successful application of the MRFM to several foundation types with several levels of excitation. Information was able to be obtained about the differences between the several foundations and damage to the structure. It was also seen how calculating dissipated energy in the structure was able to help indicate damage in the superstructure but also in the foundation system itself. Finally, the MRFM was seen to be a valuable tool to use on wind turbine blades in Chapter 5. Although, not much information was gain from the test as it was mostly a preliminary test it gave information into what should be done in future studies.

Ultimately it was seen that the MRFM is a viable option for SHM of nonlinear multidegree of freedom dynamic systems. It is able to quantify damage, locate damage and is applicable to a wide variety of structural systems.

6.2 Challenges Presented In The Application Of The Restoring Force

While the MRFM is a very attractive option for SHM capable of identifying damage and location of damage it still has some challenges to overcome. The following is just a list of

challenges that were observed during this study.

1. Measurements are needed for force.

- Results from the MRFM are dependent on the force applied to the structure. While sometimes the force applied to the structure is negligible this is not always true. For the MRFM to be applied to wind turbine blades in real world applications a way to measure the force acting over the structure is necessary.

2. Measurement of velocity and displacement.

- The MRFM uses a phase diagram of velocity, displacement and restoring force to calculate the coefficients. Error in either of these could result in significant error in the calculated system coefficients. While in this study displacement and velocity were calculated from numerical integration of acceleration. It would be beneficial to at least measure the displacement with this information numerical differentiation to find velocity this would ensure checks on how well velocity was estimated by both use of acceleration and displacement data.

3. Calculation of structures mass.

- Calculation of the restoring force is dependent on the use of mass. While mass normalized restoring force can be used it should be noted this requires the assumption that mass at all elements of interest are equal. Error in this assumption especially at the top elements of this structure will generate error all the way down the structure.

6.3 Suggestions For Future Studies

The suggestions for future studies will be broken into respective sections for; the MDOF RFM, the shaker table data set and the applications of the MDOF RFM to the wind turbine blade.

To begin, the RFM at its heart is a computationally efficient method, while the calculation of the Chebyshev coefficients is minimum, the RFM can require a decent amount of computational time depending on the use of interpolation function. Selection of the proper interpolation function is often important and while the current RBFs is very powerful and useful it is very slow. There have been many developments in the research of RBFs, there are newer versions that have faster computational times, less memory requirements and also smoothing functions. An addition of one of these newer RBFs would be a great replacement to the current RBFs.

Next, for the shaker table data set, while the information from the MDOF RFM has been extracted and compared with each other it would be wise to compare it with other methods. Comparison of mode shapes, coefficients and energy dissipation would all be places to start.

Lastly, the wind turbine blade. Some information was gained about this project but to continue on longer data sets should be collected, a longer data set would give a better opportunity to acquire more accurate information about the system. Also the MDOF RFM shows that it would be a useful tool in require information from blades made of different materials, system parameters such as stiffness and damping could easily be compared between multiple blades. Utilizing several data sets though to get an average would be the best approach to do so though. In addition to stiffness and damping coefficients information about dissipated energy from each type of blade material would be an interesting comparison.

LIST OF REFERENCES

- ASCE (2009). “2009 Report Card for America’s Infrastructure.
- Bornn, L., Farrar, C. R., and Park, G. (2010). “Damage detection in initially nonlinear systems.” *International Journal of Engineering Science*, 48(10), 909–920.
- Butterfield, S., Musial, W., Jonkman, J., and Sclavounos, P. (2005). “Engineering Challenges for Floating Offshore Wind Turbines.” *Copenhagen Offshore Wind Conference*, Copenhagen, National Renewable Energy Laboratory, <<http://www.nrel.gov/wind/pdfs/38776.pdf>>.
- Carr, J. C., Fright, W. R., and Beatson, R. K. (1997). “Surface interpolation with radial basis functions for medical imaging.” *IEEE transactions on medical imaging*, 16(1), 96–107.
- Chen, Y. (2001). “Shaking Table Testing on Dynamic Soil-Structure Interaction System.” Ph.D. thesis, Tongji University, Shanghai.
- Chopra, A. (2006). *Dynamics of Structures*. Prentice Hall, Englewood Cliffs, NJ, 3rd edition.
- Clarke, S., Courtney, F., Dykes, K., Jodziewicz, L., and Watson, G. (2009). “U.S. Offshore Wind Energy: A Path Forward, <<http://www.usowc.org/pdfs/PathForwardfinal.pdf>>.
- Deak, T. and Czigany, T. (2009). “Chemical Composition and Mechanical Properties of Basalt and Glass Fibers: A Comparison.” *Textile Research Journal*, 79(7), 645–651.
- Doebling, S. W., Farrar, C. R., Prime, M. B., and Shevitz, D. W. (1996). “Damage Identification and Health Monitoring of Structural and Mechanical Systems from Changes in Their Vibration Characteristics: A Literature Review.” *Report no.*, Los Alamos National Laboratory, Los Alamos, New Mexico, <http://institute.lanl.gov/ei/shm/pubs/lit_review.pdf>.

- Fasshauer, G. E. (2007). *Meshfree Approximation Methods with Matlab (with Cd-rom)*. World Scientific, <<http://books.google.com/books?id=gtqBdMEqryEC&pgis=1>>.
- Finnemore, E. and Franzini, J. (2001). *Fluid Mechanics With Engineering Applications*. McGraw-Hill Science/Engineering/Math, <<http://www.amazon.com/Fluid-Mechanics-With-Engineering-Applications/dp/0072432020>>.
- Hernandez-Garcia, M. R., Masri, S. F., Ghanem, R., Figueiredo, E., and Farrar, C. R. (2010). “An experimental investigation of change detection in uncertain chain-like systems.” *Journal of Sound and Vibration*, 329(12), 2395–2409.
- Hollman, P. (2006). “Off-shore Wind Farm Turbine,” <http://commons.wikimedia.org/wiki/File:Off-shore_Wind_Farm_Turbine.jpg>.
- Masri, S. F., Bekey, G. A., Sassi, H., and Caughey, T. K. (1982). “Non-parametric identification of a class of nonlinear multidegree dynamic systems.” *Earthquake Engineering & Structural Dynamics*, 10(1), 1–30.
- Masri, S. F. and Caughey, T. K. (1979). “A Nonparametric Identification Technique for Non-linear Dynamic Problems.” *Journal of Applied Mechanics*, 46(2), 433–447.
- Morgan, C. and Jamieson, P. (2001). “Offshore Wind Energy Ready To Power a Sustainable Europe.” *Report no.*, Delft University Wind Energy Research Institute, Delft, <<http://www.emu-consult.dk/includes/totalfinalreport.pdf>>.
- Musial, W., Butterfield, S., and Boone, A. (2003). “Feasibility of Floating Platform Systems for Wind Turbines.” *ASME Wind Energy Symposium*, Reno, National Renewable Energy Laboratory.
- Musial, W., Butterfield, S., and Ram, B. (2006). “Energy from Offshore Wind.” *Off-*

- shore Technology Conference*, Houston, National Renewable Energy Laboratory, 14, <<http://www.nrel.gov/docs/fy06osti/39450.pdf>>.
- Nayeri, R. D., Masri, S. F., Ghanem, R. G., and Nigbor, R. L. (2008). “A novel approach for the structural identification and monitoring of a full-scale 17-story building based on ambient vibration measurements.” *Smart Materials and Structures*, 17(2), 025006.
- Person, W. J. (1997). “Significant Earthquakes of the World 1990-1995, <<http://pubs.usgs.gov/of/1997/0494/report.pdf>>.
- Piersol, A. and Paez, T. (2009). *Harris’ Shock and Vibration Handbook (McGraw-Hill Handbooks)*. McGraw-Hill Professional, <<http://www.amazon.com/Harris-Vibration-Handbook-McGraw-Hill-Handbooks/dp/0071508198>>.
- Quagliarini, E., Monni, F., Lenci, S., and Bondioli, F. (2012). “Tensile characterization of basalt fiber rods and ropes: A first contribution.” *Construction and Building Materials*, 34(null), 372–380.
- Rosa, I. M., Marra, F., Pulci, G., Santulli, C., Sarasini, F., Tirillò, J., and Valente, M. (2011). “Post-Impact Mechanical Characterisation of Glass and Basalt Woven Fabric Laminates.” *Applied Composite Materials*, 19(3-4), 475–490.
- Sherman, M. (2008). “Wind Turbine-Udumalpet, <http://commons.wikimedia.org/wiki/File:Wind_Turbine-Udumalpet.jpg>.
- Sohn, H., Farrar, C. R., Hemez, F. M., Shunk, D. D., Stinemates, D. W., Nadler, B. R., and Czarnecki, J. J. (2004). “A Reivew of Structural Healht Monitoring Literature: 1996-2001.” *Report no.*, Los Alamos National Labratory, Los Alamos, New Mexico, <http://institute.lanl.gov/ei/shm/pubs/LA_13976_MSa.pdf>.

- Sprey, K. (2009). “HyWind - World’s First Floating Wind Turbine Reaches Its Final Destination, <<http://www.gizmag.com/hywind-floating-wind-turbine/11961/>>.
- Stover, C. W. and Coffman, J. L. (1993). *Seismicity of the United States, 1568-1989 (U.S. Geological Survey Professional Paper, 1527)*. United States Geological, <<http://www.amazon.com/Seismicity-United-1568-1989-Geological-Professional/dp/9992738006>>.
- U.S. National Renewable Energy Laboratory (2007). “United States Wind Resources and Transmission Lines Map, <<http://www.nrel.gov/gis/pdfs/windsmodel4pub1-1-9base200904enh.pdf>>.
- U.S. National Renewable Energy Laboratory (2011). “New Modeling Tool Analyzes Floating Platform Concepts for Offshore Wind Turbines.
- Wolfe, R. W., Masri, S. F., and Caffrey, J. (2002). “Some structural health monitoring approaches for nonlinear hydraulic dampers.” *Journal of Structural Control*, 9(1), 5–18.
- Worden, K. (1990). “Data processing and experiment design for the restoring force surface method, part I: integration and differentiation of measured time data.” *Mechanical Systems and Signal Processing*, 4(4), 295–319.
- Yang, J., Peng, C., Xiao, J., Zeng, J., Xing, S., Jin, J., and Deng, H. (2013). “Structural investigation of composite wind turbine blade considering structural collapse in full-scale static tests.” *Composite Structures*, 97(null), 15–29.
- Yang, W., Tavner, P., Crabtree, C., and Wilkinson, M. (2010). “Cost-Effective Condition Monitoring for Wind Turbines.” *IEEE Transactions on Industrial Electronics*, 57(1), 263–271.
- Yun, H.-B. and Masri, S. F. (2008). “Stochastic change detection in uncertain nonlinear systems

using reduced-order models: system identification.” *Smart Materials and Structures*, 17(1), 015040.

Yun, H.-B. and Masri, S. F. (2009). “Stochastic change detection in uncertain nonlinear systems using reduced-order models: classification.” *Smart Materials and Structures*, 18(1), 015004.

Yun, H.-B., Tasbighoo, F., Masri, S., Caffrey, J., Wolfe, R., Makris, N., and Black, C. (2008). “Comparison of Modeling Approaches for Full-scale Nonlinear Viscous Dampers.” *Journal of Vibration and Control*, 14(1-2), 51–76.

Zill, D. G. and Cullen, M. R. (2006). *Advanced Engineering Mathematics*. Jones & Bartlett Publishers, <<http://www.amazon.com/Advanced-Engineering-Mathematics-Dennis-Zill/dp/076374591X>>.